

Dynamics of Micro-Particles in Complex Environment

Fengchang Yang

Dissertation submitted to the faculty of the Virginia Polytechnic Institute and State University in partial fulfillment of the requirements for the degree of

Doctor of Philosophy
In
Mechanical Engineering

Rui Qiao, Chair

Michael von Spakovsky

Chang Lu

Mark Paul

Yang Liu

June 8, 2017
Blacksburg, VA

Keywords: particle dynamics, bubble behavior, surface walker

Copyright © 2017, Fengchang Yang

Dynamics of Micro-Particles in Complex Environment

Fengchang Yang

ABSTRACT

Micro-particles are ubiquitous in microsystems. The effective manipulation of micro-particles is often crucial for achieving the desired functionality of microsystems and requires a fundamental understanding of the particle dynamics. In this dissertation, the dynamics of two types of micro-particles, Janus catalytic micromotors (JCMs) and magnetic clusters, in complex environment are studied using numerical simulations.

The self-diffusiophoresis of JCMs in a confined environment is studied first. Overall, the translocation of a JCM through a short pore is slowed down by pore walls, although the slowdown is far weaker than the transport of particles through similar pores driven by other mechanisms. A JCM entering a pore with its axis not aligned with the pore axis can execute a self-alignment process and similar phenomenon is found for JCMs already inside the pore. Both hydrodynamic effect and “chemical effect”, i.e., the modification of the concentration of chemical species around JCMs by walls and other JCMs, play a key role in the observed dynamics of JCMs in confined and crowded environment.

The dynamics of bubbles and JCMs in liquid films covering solid substrates are studied next. A simple criterion for the formation of bubbles on isolated JCMs is developed and validated. The anomalous bubble growth law ($r \sim t^{0.7}$) is rationalized by considering the relative motion of growing bubbles and their surrounding JCMs. The experimentally observed ultra-fast collapse of bubbles is attributed to the coalescence of the bubble with the liquid film-air interface. It is shown that the collective motion of JCMs toward a bubble growing on a solid substrate is caused by the evaporation-induced Marangoni flow near the bubble.

The actuation of magnetic clusters using non-uniform alternating magnetic fields is studied next. It is discovered that the clusters' clockwise, out-of-plane rotation is a synergistic effect of the magnetophoresis force, the externally imposed magnetic torque and the hydrodynamic interactions between the cluster and the substrate. Such a rotation enables the cluster to move as a surface walker and leads to unique dynamics, e.g., the cluster moves away from the magnetic source and its trajectory exhibits a periodic fluctuation with a frequency twice of the field frequency.

Dynamics of Micro-Particles in Complex Environment

Fengchang Yang

GENERAL AUDIENCE ABSTRACT

Miniaturization of mechanical systems has attracted great interests in the past several decades. Micro-particles are ubiquitous in microsystems. Achieving the target performance of these systems often hinges on the effective manipulation of micro-particles, which in turn requires a fundamental understanding of the dynamics of micro-particles in complex environments. In this dissertation, the dynamics of two types of micro-particles, Janus catalytic micromotors (JCMs) and magnetic clusters, in complex environment are studied using numerical simulations and scale analysis.

Simulations revealed that the transport of JCMs through short pores with diameter comparable to their diameter is slowed down by the pore walls. In addition to purely hydrodynamic effects, the modification of the species concentration near JCMs by confining pore walls and neighboring JCMs also greatly affects the dynamics of JCMs in confined and crowded environments. Bubbles can greatly affect the dynamics of JCMs and anomalous bubble formation, growth, and collapse behavior have been reported. It is shown that the peculiar bubble behavior reported experimentally originates from the fast mass transport and interactions between bubbles with confining interfaces. The evaporation-induced Marangoni flow near a growing bubble is shown to lead to the collective movement of JCMs toward the bubble base. Simulations also help explain why non-uniform AC magnetic fields can drive magnetic clusters toward position with weaker magnetic fields.

Dedication

To my parents,
Xiong Yang and Juan Ma,
And all of my friends,
Without whom none of my success would be possible

Acknowledgements

Pursuing a Ph.D. degree is like a wild voyage in the sea of endless knowledge. You sometimes feel lost and may not be able to find the right path by yourself. Fortunately, I could find the destination of this voyage following the guidance from others and I feel really grateful for the support and help I received during this fantastic journey. The experience through my Ph.D. study changes my life and will be remembered forever.

First of all, I want to thank my advisor Dr. Rui Qiao for his endless support and guidance through my Ph.D. study. When I first arrived in the US, I did not have an advisor and feel anxiety. I still remember the day that Dr. Rui Qiao talked with me and welcomed me to the TPL group. Without his help, I would not be able to tackle so many difficult problems and finish my Ph.D. study. He not only serves as an excellent academic advisor with his abundant knowledge but also shares his life philosophy and experiences, which greatly benefit me and help me become more mature. It is my great honor to study under his guidance and words alone simply cannot express my gratitude.

I also want to thank my academic committee members, Dr. Michael von Spakovsky, Dr. Mark Paul, Dr. Chang Lu, and Dr. Yang Liu for their valuable suggestions and feedbacks on my research and dissertation.

I would like to thank all the collaborators through my Ph.D. study, especially Dr. Yiping Zhao from the University of Georgia, Dr. Shizhi Qian from Old Dominion University, Dr. Jingsong Huang and Dr. Bobby G. Sumpter from Oak Ridge National Lab. It is their wise suggestion and inspiration that make my research projects more successful. I want to thank other collaborators who helped me during my Ph.D. studies as well.

Furthermore, I want to thank all the TPL group members for their help and good times I had in the group. I have learned a lot from them and gain great help from them as well. I am grateful that I could meet so many great peoples and become good friends with them. I want to thank Dr. Xikai Jiang and Dr. Ying Liu for their wise advice in both research and life, Dr. Guang Feng and Dr. Peng Wu for their valuable suggestions especially in career planning, Yadong He, and Fei Zhang for their numerous helps during my Ph.D. study. I would also like to thank Chao Fang, Zhou Yu and Haiyi Wu for the countless discussions and good times in the group. All of them have inspired me to some extent, and I hope to maintain these invaluable friendships for the rest of my life.

During my Ph.D. Study, I have made some great friends and I would like to thank them for their support as well. Those include Dr. Bowen Ling, Dr. Shuaishuai Liu, Dr. Ziyuan Ma, Dr. Xinran Tao, Dr. Chengjian Li and many others. I want to thank my host family (Mr.&Mrs. Laiewski) for their kindness and help when I am trying to adapt to the life in the US. I also would like to thank my best friends back in China for their support.

Finally, I want to thank my passed grandfather Tianci Yang who will always be in my heart. I also want to thank my parents Xiong Yang and Juan Ma, who always support and care about me. There is nothing more important in the world than my family. Without their selfless support and love, I would not be able to pursue my Ph.D. in a different country. Thank you, Mom and Dad!

Contents

Chapter 1. Introduction.....	1
1.1 Past Works on Micro-particle Manipulation.....	4
1.2 Recent Development in Micro-particle Manipulation	11
1.2.1 Active Particles	11
1.2.2 Magnetically Steered Surface Walkers	16
1.3 Open Questions and Scope of This Dissertation.....	18
Chapter 2. Self-Diffusiophoresis of JCMs in Confined Geometries	21
2.1 Mathematical Model and Numerical Implementation	21
2.1.1 Model for Self-Diffusiophoresis	21
2.1.2 Numerical Implementation and Validation.....	25
2.2 Results and Discussion	28
2.2.1 Translocation of a Single Spherical JCM Through a Short Pore	28
2.2.2 Translocation of a Pair of Spherical JCMs through a Short Pore	38
2.2.3 Rotational Dynamics of Circular JCMs Near and in Short Pores	40
2.3 Conclusions.....	47
Chapter 3. Bubble-Induced Collective Motion of JCMs.....	49

3.1	Brief Summary of Experimental Observations	49
3.2	Evaporation-Induced Collective Motion of JCMs	53
3.2.1	Hypothesis and Scale Analysis	53
3.2.2	Numerical Simulation of Marangoni Flow in the Vicinity of a Bubble.....	56
3.3	Conclusions.....	63
Chapter 4. Bubble Behaviors in JCM Systems.....		65
4.1	Bubble Formation in JCM Systems	65
4.2	Bubble Growth in JCM Systems.....	77
4.3	Bubble Collapse in JCM Systems	85
4.4	Conclusions.....	89
Chapter 5. Particle Manipulation using AC Magnetic Fields.....		91
5.1	Brief Summary of Experimental Observations	91
5.2	Theoretical Analysis	94
5.2.1	Theoretical Model.....	94
5.2.2	Numerical Simulations Setup.....	98
5.2.3	Simulation Results and Analysis.....	101
5.3	Conclusions.....	104

Chapter 6. Summary.....	105
Reference.....	109

List of Figures

Figure 1-1. The sizes and shapes of some small-scale objects and materials. Reproduced from Ref. 15 with permission.	2
Figure 1-2. Mechanism of an atomic force microscope (AFM). (a) Schematic of an atomic force microscope. (b) Schematic of the force transducer operation. The function of the transducer is to measure the force between an AFM probe tip and the sample surface. (a) and (b) are reproduced from www.nanoscience.com and Ref. 19 with permission, respectively.	3
Figure 1-3. (a) Behaviors of particles in a uniform electric field (electrophoresis). (b) Behaviors of particles in a non-uniform electric field (dielectrophoresis). Reproduced from Ref. 39 with permission.	5
Figure 1-4. Magnetic particles are pumped through a buffer into the channel and separated by an external magnetic field. A non-uniform magnetic field is applied perpendicular to the direction of flow. Particles according to their size and magnetic susceptibility are separated from each other and from a nonmagnetic material. Reproduced from Ref. 58 with permission.	8
Figure 1-5. Acoustic forces that act on a particle. F_{Ax} is the axial component of the PRF, F_{Tr} is the transverse component of the PRF, and F_B is the interparticle force. T_1 is the time that acoustic forces act on the particles and T_2 is the time to steady state. Reproduced from Ref. 64 with permission.	9
Figure 1-6. (a) A Janus catalytic micromotor half coated with platinum. (b) A schematic of the fabrication process of a Janus catalytic micromotor. Reproduced from Ref. 86 with permission.	12
Figure 1-7. (a) The geometry of the “surface walker”. (b) Comparison of the particle trajectories obtained from experiments and simulations at different frequencies of the magnetic field (top: 5 Hz, bottom: 7 Hz). Reproduced from Ref. 128 with permission.	17

Figure 2-1. A schematic of the JCM. Half of the JCM’s surface (Γ_2 , colored in red) is coated with catalyst while the other half of the JCM (Γ_1 , colored in blue) exhibits no catalytic reactivity. The large black arrow indicates the swimming direction of JCM due to self-diffusiophoresis when the product of the catalytic reaction interacts repulsively with the JCM..... 22

Figure 2-2. Diffusiophoresis velocity of a single JCM in bulk hydrogen peroxide solution predicted by the analytical model (Equ. 2-14) and numerical simulations..... 26

Figure 2-3. Passive diffusiophoresis velocity of a sphere in a long pore computed using simulations and using the analytical solution (Equ. 2-15). Inset is a schematic of the simulation model. 27

Figure 2-4. A schematic of a JCM translocating through a narrow pore. The JCM, with its catalytic surface facing the negative z -direction, is initially positioned at a distance of R_{JCM} from the pore’s entrance. The large black arrow indicates the swimming direction of the JCM due to self-diffusiophoresis. The c_s and c_n are the product concentration at the south and north poles of JCM, respectively..... 29

Figure 2-5. Translocation of a JCM through cylindrical pores with different radii but same length ($L_p = 20R_{JCM}$). (a) position of the JCM inside the pore at three time instants; (b-c) the evolution of JCM dimensionless velocity and JCM dimensionless traveling distance as the JCM “swims” through the pore. The plus signs in (b) mark the time instants at which the JCM exits the pore. A JCM completes its translocation through the pore when it reaches $Z^*=1$, and the corresponding time instant is marked using by “x” in (c). 30

Figure 2-6. The reaction product concentration at the south and north poles of the JCM. The evolution of c_s^* (solid line) and c_n^* (dashed line) (a), and the difference of reaction product concentration at the south and north poles of the JCM (b) as the JCM “swims” through the pore. 32

Figure 2-7. Comparison of the average speed of sphere through pores driven by different mechanisms as a function of confinement $\beta_W = R_p/R_s$ (R_p and R_s are the radius of the pore and sphere, respectively). For each transport mechanism, the average speed of the sphere inside a pore U_p is scaled using the sphere's speed in the free solution, U_∞ . Insets are the sketches of different particle transport mechanisms..... 33

Figure 2-8. Translocation of a JCM through cylindrical pores with different lengths but the same radius ($R_p = 2R_{JCM}$). The evolution of JCM dimensionless velocity (a), the c_s^* (solid line) and c_n^* (dashed line) (b), JCM dimensionless position (c), and the difference of reaction product concentration at the south and north poles of the JCM (d) as the JCM “swims” through the pore. 35

Figure 2-9. Translocation of a pair of JCMs through a short pore. (a-b) Evolution of the velocity (panel a) and the position (panel b) of each JCM as a function of time. The dashed line is the result of single JCM translocation through the same short pore from Fig. 2-5. A JCM completes its translocation through the pore when it reaches $Z^*=1$. (c) Reaction product concentration field at $\tau = 0.9$, when the front JCM is about to exit the pore (the JCMs are marked by the white circles). The black circles denote the initial positions of the JCMs. The arrows denote the slip velocity on the JCMs' surface. 38

Figure 2-10. Trajectories of JCMs with different initial inclination angles θ_0 near a pore's entrance. The JCM's center is initially positioned at $z=0$. For small θ_0 , the JCM can rotate toward the pore interior and swim into the pore. For large θ_0 , the JCM either collides with the pore wall or swim away from the pore. 41

Figure 2-11. Distribution of the phoretic slip velocity u_s on the surface of JCMs when they approach the pore wall. Each JCM is originally placed at the pore entrance with an inclination angle θ_0 as shown in Fig. 2-10. The surface on which u_s points in the clockwise (counter-clockwise) direction with respect to the JCM center and the local viscous stress causes a counter-clockwise (clockwise) torque is defined as Γ_{cc} (Γ_c). In (a) and (c), u_s is taken, hypothetically, to be that for JCM in the free solution to isolate the hydrodynamic

effect on JCM rotation. In (b) and (d), the real u_s determined in simulations is shown to help delineate the chemical effects on JCM rotation. 43

Figure 2-12. The self-alignment behavior of JCM swimming inside a pore. The JCM was initially placed near the pore entrance with phoretic axis fully aligned with the pore axis. An external, clockwise torque was applied on the JCM during $\tau=0.34-0.52$ to rotate the JCM in the clockwise direction. (a-b) The trajectory (a) and the inclination angle (b) of the JCM as a function of time. (c) The distribution of the reaction product near the JCM at $\tau=0.87$. The black arrows denote the phoretic slip velocities on the JCM's surface. 45

Figure 3-1. Snapshots of JCMs as they get densely populated in a small region and the subsequent bubble and ring formations. The small black dots are the 5 μm diameter JCMs. 50

Figure 3-2. After the initial bubble collapse, the JCMs are locked in a ring. They all travel towards the center of the bubble as it grows. (a) The screenshot of an instant when new bubble starts to grow. The black lines highlight the trajectory of each motor. (b) The histogram of the decomposed displacements of JCMs in the radial and the tangential directions (for each JCM, the line pointing from the center of bubble to the center of the JCM is defined as the radial direction). 51

Figure 3-3. Log-log plot of the bubble growth radius R_b as a function of time t for different groups (hydrophobic and hydrophilic) of motors. Each different symbol represents a new bubble cycle. The red dotted line represents the power law fitting $R_b \sim t^n$ with $n = 0.7$ 52

Figure 3-4. A schematic of the evaporation induced Marangoni flow. Cooling via evaporation at the top surface of the liquid film creates a temperature gradient along bubble surface. Such a temperature gradient generates a Marangoni stress on bubble surface, which in turn induces a Marangoni flow in the vicinity of the bubble. 54

Figure 3-5. System used to investigate the evaporation-induced Marangoni flows: a spherical bubble is anchored on a substrate, which is covered by a thin liquid film.	57
Figure 3-6. The mesh used in simulations in which the bubble radius is 20 μm	61
Figure 3-7. Marangoni flow in the vicinity of the bubble within a cooling liquid film. (a) The velocity field (blue vectors) and temperature contours (red lines) are calculated for a bubble radius of 30 μm . The thickness of the liquid film is 100 μm , and a uniform cooling flux of 200 W/m^2 is applied on the liquid film surface. (b) Temperature profile across the liquid film at a radial position of 100 μm	61
Figure 3-8. The radial velocity of the Marangoni flow in the vicinity of a bubble. Flow velocities are evaluated at a position of 5 μm above the substrate (dashed line in the inset). The thickness of the liquid film is 100 μm , and a uniform cooling flux of 200 W/m^2 is applied to the film surface. The negative velocity corresponds to the flow toward the bubble base.	62
Figure 4-1. Formation of a critical bubble embryo on a solid sphere whose surface produces oxygen by catalytic reactions.....	68
Figure 4-2. Radius of critical bubble embryo attached to uniformly coated spheres and half-coated JCMs immersed in bulk solutions.	71
Figure 4-3. Setup used to simulate the O_2 concentration field generated by an isolated JCM. A JCM is placed in a liquid solution (denoted by Ω). Γ_1 denotes the boundary of the spherical liquid solution. Γ_2 and Γ_3 denote the neutral surface and catalytic surface of JCM, respectively. The domain of the liquid solution has a radius of 100 times of the JCM radius.	72
Figure 4-4. The mesh used for simulation of the system shown in Fig. 4-2.	73

Figure 4-5. The simulation domain and mesh used for computing the oxygen concentration near a cluster of four JCMs positioned above a substrate. 74

Figure 4-6. The O_2 concentration distribution near singlet JCMs and JCMs in small clusters. The JCMs ($R_p=2.5 \mu\text{m}$) are situated at $1.25 \mu\text{m}$ above the solid substrate and their catalytic surface faces the center of the cluster. The center-to-center distance between the opposing JCMs in a cluster is $10\mu\text{m}$. The O_2 production rate on the JCM's catalytic surface is $1.08 \times 10^{-3} \text{mol}/(\text{m}^2 \cdot \text{s})$. The concentration profile is shown along the dashed lines shown in the inset. $x=0$ is defined as the center of the cluster or at the position 2.5mm away from the pole of a singlet JCM. 75

Figure 4-7. A schematic of the switching of bubbling site in the first bubbling cycle. A critical bubble embryo is formed on the JCM surface and grows to touch the substrate. Following the burst of the fully-grown bubble, a residual bubble is left on the substrate, which serves as the bubbling site in subsequent bubble growth-burst cycles. 77

Figure 4-8. Simulation of bubble growth due to remote feeding by a ring of JCMs. (a) Schematic of the simulation system; (b) A 3D sketch of the system. The N JCMs surrounding the bubble are lumped into a torus structure with its inner surface (marked in red) as catalytic surface and its outer surface (marked in blue) as the neutral surface. 79

Figure 4-9. A typical mesh used in simulations of the growth of a bubble fed by a ring of JCMs around it. 82

Figure 4-10. Time evolution of the bubble radius (R_b) predicted by simulations. (a) The effect of the number (N) of JCMs in the ring surrounding the bubble on the bubble growth (the inward velocity of the JCM ring V_p is fixed at $15 \mu\text{m}/\text{s}$). (b) The effect of the JCM inward velocity toward the bubble on its growth (the number of JCMs in the ring surrounding the bubble is fixed at $N=20$). 83

Figure 4-11. The system used to investigate the coalescence of a bubble with an air-liquid interface. 86

Figure 4-12. Coalescence of a bubble inside a liquid film with the air-liquid interface. Once the bubble’s north pole merges with the air above the liquid-air interface, the bubble collapses rapidly under the action of surface-tension-induced flows..... 88

Figure 5-1. Trajectories of the MCs at two different field configurations: (a) a uniform alternating magnetic field; (b) a nuAMF generated by a single solenoid..... 92

Figure 5-2. (a) The translational speed v of MCs and (b) a single Ni NR versus different I_0 ($f_H = 10$ Hz). 93

Figure 5-3. (a) The plot of the translational moving speed v of different sized MCs and (b) a single Ni NR as a function of nuAMF frequency f_H . Here $I_0 = 2$ A..... 94

Figure 5-4. The translational and rotational motion of a magnetic cluster (MC) driven by low-frequency nuAMF. (a) External alternating H-field as a function of time. (b) Force and torque analysis of a MC in an AC H-field. (c1-2) Pressure distribution on the MC surface at $t = t_1$ and t_3 moments. Initially, the magnetic moment of the MC aligns with the external \mathbf{H} . By time instant t_1 , \mathbf{H} changes to the new orientation, which is opposite to its original orientation. The MC experiences a magnetophoresis force \mathbf{F}_{mp} pointing toward the solenoid. This \mathbf{F}_{mp} induces a weak hydrodynamic torque \mathbf{T}_{mp} on the MC, which drives it to rotate in the clockwise direction (see c1). Once the MC deviates from its original orientation, it experiences a magnetic torque \mathbf{T}_{mt} caused by \mathbf{H} , which further drives its clockwise rotation. Consequently, the MC shows persistent rotation and moves away from the solenoid ($t = t_3$ and c2) as a surface walker¹²⁸ until it fully aligns with the external magnetic field \mathbf{H} ($t = t_4$). 95

Figure 5-5. Simulation results of the motion of a magnetic cluster in one period of low-frequency nuAMF. (a) The external nuAMF. (b) The angle between the cluster’s magnetic moment and the horizontal plane. (c) The cluster’s displacement. (d) The cluster’s translational velocity. 100

Figure 5-6. Evolution of the width of a magnetic cluster projected onto the horizontal plane over several periods of AC magnetic field ($f_H = 5$ Hz or $\tau = 0.2$ s). Inset (a) show the definition of the projected width of the cluster. Inset (b) is the representative experimental result compared with simulation data. The two downward spikes correspond to the rapid alignment of the cluster with the external magnetic field once it rotates away from the 0° or 180° orientation (see Fig. 5-5b). The projected width maintains its maximal value most of the time, indicating that the cluster is fully aligned with the low-frequency magnetic field studied here. 102

Figure 5-7. Effects of the amplitude of current I_0 (a) and field frequency f_H (b) of nuAMF on the translational velocity obtained from simulations. 103

Chapter 1. Introduction

In the year 1959, Dr. Richard R. Feynman envisioned a new field at the Annual Meeting of the American Physical Society, which had not been taken seriously at that moment. In his famous talk “There’s plenty of room at the bottom”, he said:¹

“I would like to describe a field, in which little has been done, but in which an enormous amount can be done in principle. ... What I want to talk about is the problem of manipulating and controlling things at small scale.”

Since then, the miniaturization of the components used in the construction of many working devices has been pursued for decades. Numerous efforts have been devoted to developing tools and methods for fabricating or assembling micro-/nano-scale components.²⁻¹⁰ As a result, over the past 50 years, the dimensions of electronic components on CPU/GPU have reduced from the millimeter to nanometer scale and the performance of computers have steadily improved following Moore’s law.¹¹ Similar to electronic components, the miniaturization of mechanical components has also brought many benefits as the dimensions of mechanical systems have been scaled down to microdomain.^{2, 12-14} Indeed, natural and fabricated small-scale objects are ubiquitous in biological and engineering applications. Figure 1-1 shows a few examples of small-scale objects and their critical dimensions.¹⁵ However, as systems are scaled down, many operations, which are often trivial at the macro-scale, becomes challenging. A prominent example is the manipulation of small objects. At the macro-scale, one can easily pick up and manipulate objects using macroscopic tools. These seemingly trivial operations often become difficult at small scales (μm - nm) because of unfavorable scaling laws for the forces commonly relied on at the macro-scale and the emergence of new forces at micro-scale.^{14, 16-17} Hence, there is a long-standing need to develop

effective methods for manipulating small objects.

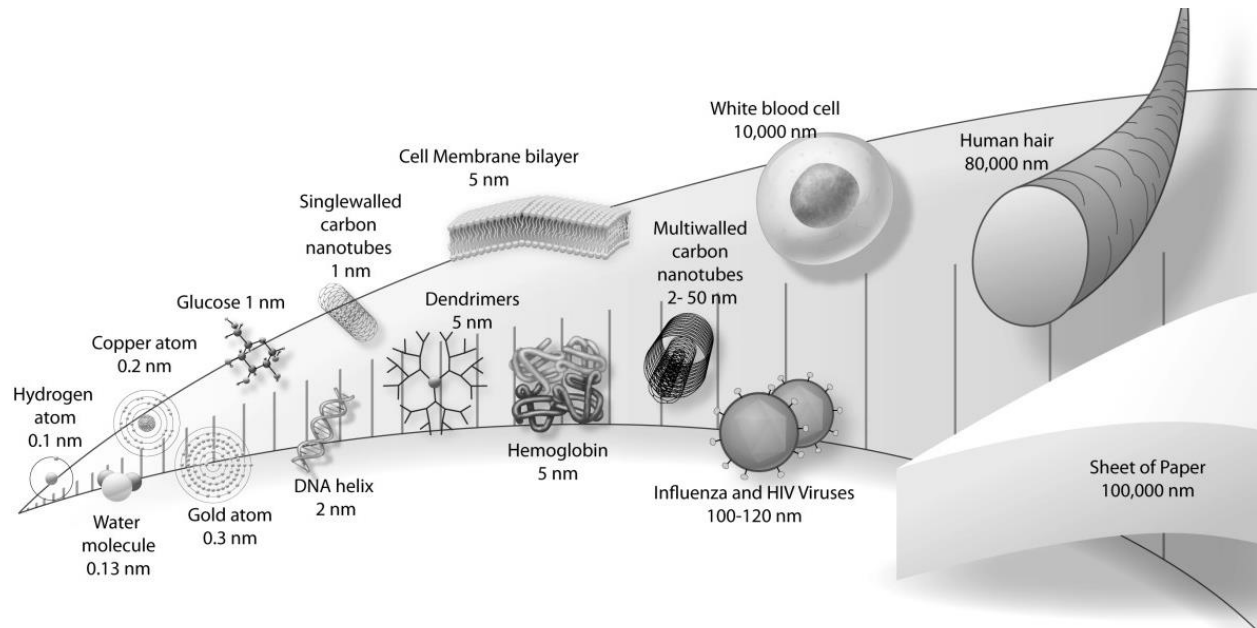


Figure 1-1. The sizes and shapes of some small-scale objects and materials. Reproduced from Ref. 15 with permission.

During the last few decades, many different tools for manipulating small objects have been developed. For instance, the atomic force microscope (AFM) has been invented to both observe and manipulate micro-objects.¹⁸⁻²⁰ As its name suggests, the atomic force microscope measures the atomic force between a sharp tip and the surface of a sample or objects. Figure 1-2 shows the schematic of the operating mechanism of an AFM. Initially, AFM is used to create an image of the microstructure of a sample surface.²¹⁻²⁵ A topographic image of the sample can be produced by plotting the deflection of the cantilever spring versus position on the sample surface. The invention of the AFM not only enables scientists to observe objects at the micro-/nano-scale but also to manipulate objects at the micro-scale. For example, the AFM has been widely used in applications such as constructing biological structures^{7, 22, 26}, moving nanoparticles²⁷, and fabricating nanowires²⁸. Overall, AFM-based systems are well suited to the “bottom-up” assembly of

microdevices due to their ability of the fine control over microstructures. In addition, besides serving as manipulator, AFMs can be employed as sensors in microsystems if needed, which gives them extra advantages.²⁹

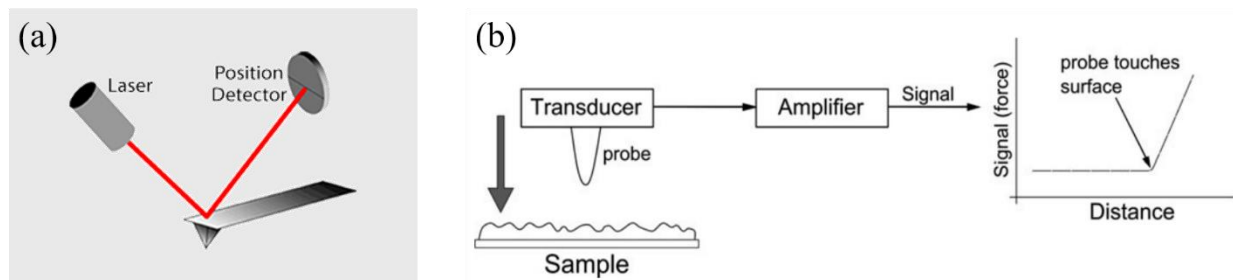


Figure 1-2. Mechanism of an atomic force microscope (AFM). (a) Schematic of an atomic force microscope. (b) Schematic of the force transducer operation. The function of the transducer is to measure the force between an AFM probe tip and the sample surface. (a) and (b) are reproduced from www.nanoscience.com and Ref. 19 with permission, respectively.

Another interesting tool developed in the past decades due to the inspiration of Dr. Feynman's talk is the artificial molecular machine.³⁰⁻³¹ An artificial molecular machine is an assembly of a set of molecular components that are designed to perform a machine-like movement (output) as the result of an appropriate external stimulation (input).³² Most molecular machines are constructed based on either topological entanglement (i.e., mechanical bonds) or isomerisable (unsaturated) bonds.³³ By gaining energy from external stimulation³⁴ (for instance, chemical fuels, UV light, *etc.*), a molecular machine can serve as a tool and create motion on length scales much larger than the machine itself. For example, a 1.25 μL diiodomethane droplet on an inclined substrate covered with molecular machines can be lifted up a short distance via the collective work of molecular machines.³⁵ By changing the arrangement of these molecular machines, the shape and direction of motion of the droplet can be controlled. Another example is embedding molecular machines in a polymer ribbon to enable the curling of the ribbon when applying UV light.² Both molecular

machines and AFMs have inspired numerous researchers in micro/nanoscale research, and come of whom were honored by the 2016 and 1986 Nobel prizes in chemistry and physics, respectively.

In many micro/nano-systems related to biology, medicine, and lab-on-a-chip, micro-particles play an important role in the system's functionality, and effective manipulation of their dynamics is essential.³⁶⁻³⁸ Typically, these micro-particles are submerged in liquid solutions, which makes their dynamics intricate and greatly complicates their manipulation. Great efforts have been devoted to developing reliable technologies for particle manipulation.³⁹⁻⁴² Below some of the most popular micro-particle manipulation technologies as well as some recent developments are reviewed.

1.1 Past Works on Micro-particle Manipulation

Over the last several decades, many methods have been developed to manipulate, separate and trap micro-particles in liquids based on the different particle dynamics induced by an external electric field, magnetic field, acoustic wave and optical light, *etc.* These methods are briefly reviewed below.

When electric fields are employed, the manipulation of micro-particles is typically achieved through electrophoresis (EP) or dielectrophoresis (DEP).⁴³ Particle electrophoresis in micro-system is the motion of a charged particle driven by an electric field as shown in Fig. 1-3a. It is a straightforward way to manipulate charged particles in microfluidic devices and is ubiquitous if electric fields are present.⁴³⁻⁴⁵ For particles with sizes much larger than the thickness of the electrical double layer and a surface potential smaller than the thermal voltage ($k_B T / e \approx 25 mV$ at room temperature), the electrophoresis velocity in an unbounded fluid can be described by the Smoluchowski equation:

$$\mathbf{u}_{EP} = \frac{\varepsilon\zeta}{\eta} \mathbf{E}, \quad (1-1)$$

where ζ is the potential, ε the fluid permittivity, and η the viscosity of the fluid, and \mathbf{E} the electric field. Commercial devices based on electrophoresis for separating/detecting proteins and DNA are commercially available.⁴⁶

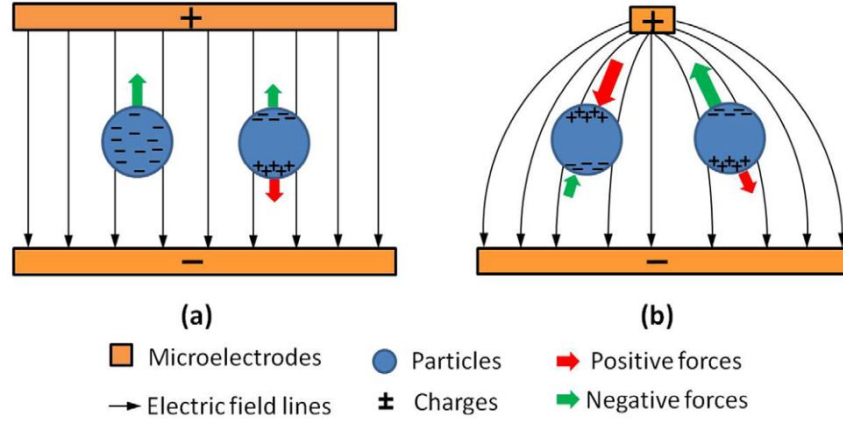


Figure 1-3. (a) Behaviors of particles in a uniform electric field (electrophoresis). (b) Behaviors of particles in a non-uniform electric field (dielectrophoresis). Reproduced from Ref. 39 with permission.

In contrast to electrophoresis, dielectrophoresis of a micro-particle requires a non-uniform electric field.⁴⁷ The term dielectrophoresis refers to the Coulomb response of an electrically polarized object in a non-uniform electric field, as shown in Fig. 1-3b. The advantages of the DEP manipulation of particles are two-fold. It does not require the particle to be charged, and it has a nonzero time-averaged effect even in AC electric fields.^{39, 43} For a particle submerged in solution, the Coulomb force acting on it can be determined from the electric field and permittivity at its surface and is given by

$$\mathbf{F}_{DEP} = \int_S \left[\varepsilon \mathbf{E} \mathbf{E} - \frac{1}{2} \delta(\varepsilon \mathbf{E} \cdot \mathbf{E}) \right] \cdot \mathbf{n} dA \quad (1-2)$$

where S is the surface of particle, δ the Kronecker delta tensor, \mathbf{n} the normal vector of the surface,

and A the surface area. Because the DEP force is independent of the field internal to the particle, many analytical models have been developed to predict the force on a real particle by replacing it with a simpler structure that creates the same electric field at the surface.⁴³ Since the DEP force mainly relies on the condition of the external non-uniform electric field, it can be conveniently controlled by changing the setting of the electric field. This feature and other advantages make it ideal for particle manipulation in microfluidic systems.^{39, 48-49} Consequently, in the past decades, DEP has been widely used for applications such as particle separation⁵⁰⁻⁵¹, transport⁵², trapping⁵³ and sorting⁴⁹.

Though particle manipulation techniques based on electric fields have been extensively studied and successfully employed in many micro-systems. A major limitation of these techniques is the complexity of the device and the potential side effects in bio-applications. This is because complex wiring and cooling systems are needed to generate strong enough electric fields. The high voltages (tens to hundreds of volts is often needed) can also cause undesired chemical reactions such as water electrolysis that could change the chemical environment of the target particles.⁵⁴⁻⁵⁵

Like electric fields, magnetic fields are also widely used for manipulating micro-particles. Compared to electric fields, magnetic fields often offer stronger manipulation forces and torques⁵⁶, which make them appealing for some applications. The most representative method of using magnetic fields to manipulate micro-particles in solution is magnetophoresis.⁴³ Theoretically, magnetophoresis is analogous to DEP. However, because of the enormous variety of magnetic materials and experimental tools for generating magnetic fields, the experimental realizations of magnetophoresis are vastly different from dielectrophoresis.

The effectiveness of magnetophoresis is greatly affected by the magnetization of particles in an magnetic field.⁵⁷⁻⁵⁸ Depending on the orbital and spin motions of the electrons, a material can

show different responses to magnetic fields. Classically, most magnetic materials can be classified into three groups: diamagnetic, paramagnetic, and ferromagnetic. Diamagnetic materials are composed of atoms which have no net magnetic moments, i.e., the electrons are all paired. When exposed to a magnetic field, a diamagnetic material produces a negative magnetization; and, thus, its susceptibility is negative. Typically, the diamagnetic effects are weak enough to be neglected and do not contribute notably to magnetophoresis. Paramagnetic materials are materials with net magnetic moments, i.e., the electrons are unpaired. However, each individual magnetic moment does not interact with other moments, and the magnetization of the material is zero when no external magnetic field is present. Once an external magnetic field is applied, the spins of the unpaired electrons align with the external magnetic field and result in a net positive magnetization. In contrast, in ferromagnetic materials such as iron, nickel, and magnetite, the atomic moments in these materials show strong interactions and lead the magnetic dipoles to lock in an orientation aligned with the field. Hence, ferromagnetic materials exhibit large net magnetization even in the absence of externally applied magnetic fields.

When a particle made of magnetic materials is placed in a non-uniform magnetic field, magnetophoresis can happen due to the interaction of a particle under magnetization and a magnetic field gradient. Magnetophoresis is analogous to the DEP of a particle. The induced dipole response of magnetic material is usually nonlinear.⁴³ The magnetophoretic force acting on a particle F_{mag} is given by

$$\mathbf{F}_{mag} = (\mu_{mag,m} m_{eff,m} \cdot \nabla) \mathbf{H}, \quad (1-3)$$

where \mathbf{H} is the external magnetic field, $\mu_{mag,m}$ is the magnetic permeability of the medium, and $m_{eff,m}$ is the magnetization induced by the field. If the magnetic field is assumed steady and particles that respond linearly to the external magnetic field, the average magnetophoretic force

acting on the particle is

$$F_{mag} = 2\pi\mu_{mag,m}R_p \left(\frac{\mu_{mag,p}-\mu_{mag,m}}{\mu_{mag,p}+2\mu_{mag,m}} \right) \nabla |H|^2. \quad (1-4)$$

where R_p is the particle radius, subscripts m and p denote the medium and particle, respectively. Magnetophoresis has been widely employed in biological applications such as drug, gene, and radionuclide delivery.⁵⁹⁻⁶⁰ Typically, depending on applied magnetic fields, magnetophoresis can be categorized as static field manipulation (SFM) or dynamic field manipulation (DFM). SFM

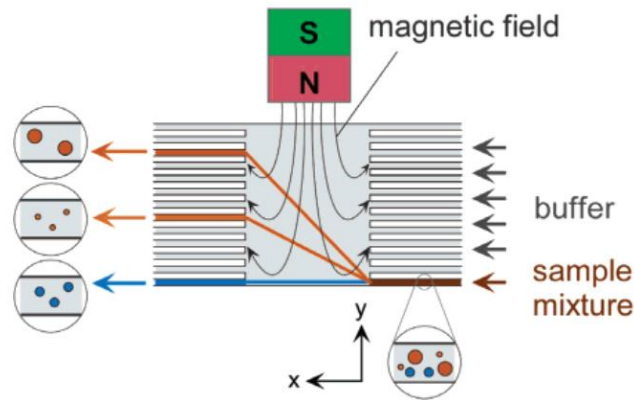


Figure 1-4. Magnetic particles are pumped through a buffer into the channel and separated by an external magnetic field. A non-uniform magnetic field is applied perpendicular to the direction of flow. Particles according to their size and magnetic susceptibility are separated from each other and from a nonmagnetic material. Reproduced from Ref. 58 with permission.

utilizes the magnetic force on a magnetic particle generated by an H-field gradient. For instance, the tip of a magnetic force microscope (MFM)^{41, 61} or similar device can generate a static local non-uniform H-field to trap a magnetic object in a fluid. The object can be transported by moving the MFM tip and then released by turning off the H-field when it arrives at the target location. The other approach, which is suitable for “lab-on-a-chip” devices, is to generate a series of patterned H-field gradients by micro-scaled current conductors (zig-zag pattern or O-ring grids) with a

programmed sequence of current signals^{42, 62-63}. The magnetic object can be transported from one field gradient to its neighbor by a sequence of trap-release steps. Figure 1-4 shows a micro-particle manipulation system developed based on magnetophoresis.

Other than electric and magnetic fields, acoustic standing waves have been used to manipulate micro-particles as well. Such a method for particle manipulation is usually called acoustophoresis. The ultrasonic standing waves used in acoustophoresis are typically generated either by the use of two opposing sound sources or by a single ultrasonic transducer facing a sound reflector.⁶⁴ The fundamental theory of acoustic standing wave forces has been extensively described by multiple groups.⁶⁵⁻⁶⁷ Normally, the force acting on a particle in a bulk acoustic wave (BAW) field is the

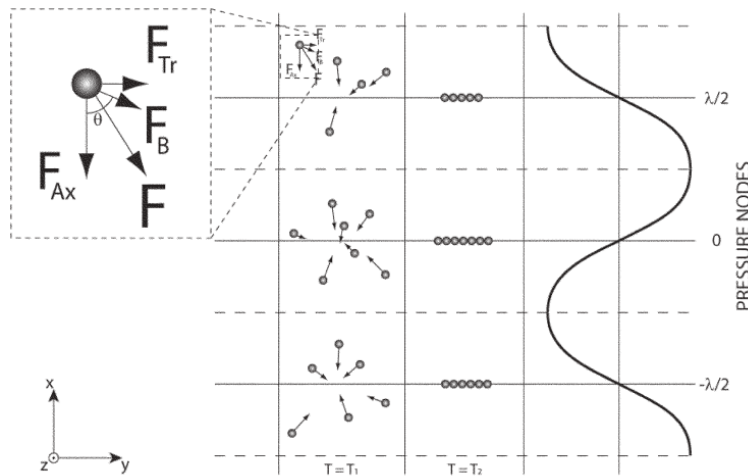


Figure 1-5. Acoustic forces that act on a particle. F_{Ax} is the axial component of the PRF, F_{Tr} is the transverse component of the PRF, and F_B is the interparticle force. T_1 is the time that acoustic forces act on the particles and T_2 is the time to steady state. Reproduced from Ref. 64 with permission.

the product of both the primary and secondary radiation forces, where the primary radiation force (PRF) originates from the standing wave and secondary radiation forces (SRF) are due to sound waves scattered by the particles. Figure 1-5 shows the primary radiation force experienced by particles from acoustic waves. The axial component of PRF is stronger than the transverse PRF

and forces particles to designed positions. The strength of axial PRF can be calculated as

$$F_{Ax} = -\left(\frac{\pi P_0^2 V_p B_m}{2\lambda}\right) \cdot \phi \cdot \sin(2kx) \quad (1-5)$$

where P_0 is the acoustic pressure amplitude, λ the wavelength, B_m the compressibility of surrounding mediums, ϕ the acoustic contrast factor, V_p the volume of the particle, and k the wave number. Recently, acoustophoresis based on so-called surface acoustic waves (SAW) has been studied as well.⁶⁸ Using acoustophoresis (BAW and SAW), many particle or cell manipulation systems have been developed for purposes such as particle focusing and separation⁶⁹, particle alignment⁷⁰, and particle directing⁷¹. For example, Yasuda *et al.*⁷² utilized ultrasound to gather red blood cells in a flow. Shi *et al.*⁷³ developed “acoustic tweezers” for particle alignment and patterning using standing surface acoustic waves. Franke *et al.*⁷¹ found the polyacrylamide particles can be directed into selected channels in water by acoustic waves. The disadvantage of acoustophoresis is the limitation of particle size that can effectively be manipulated.⁷⁴ For large objects, sedimentation often becomes a major problem.

Optical forces, which originates from the exchange of momentum between incident photons and the irradiated object, have been used to manipulate micro/nano-particles as well.⁷⁵ Unlike the methods introduced above, the optical manipulation of particles typically utilizes a laser beam instead of external fields, which makes the precise manipulation of particles feasible. In the 1970s, Ashkin and his team were the first ones who realized the potential of using a moderately focused laser beam to control micro-objects.⁷⁶ Using laser beams, they demonstrated the guiding of particles, the levitation of particles against gravity, particle trapping, *etc.*⁷⁷⁻⁷⁸ Since then, great efforts have been devoted to developing and improving optical particle manipulation techniques.⁷⁹⁻

⁸¹ One of the most popular technologies developed is the optical tweezers. This method uses a

focused Gaussian laser beam to trap dielectric particles and can manipulate objects of micrometer or sub-micrometer scale.⁸²⁻⁸³ Although it is possible to use optical tweezers to perform cell separation and sorting, its great challenge is *in vivo* applications since most visible high energy laser beams cannot penetrate the skin without damaging it.

1.2 Recent Development in Micro-particle Manipulation

Even though previous studies have greatly improved the understanding of particle dynamics in many microsystems and advanced the capability of researchers in manipulating micro-particles, each existing method still has its limitations as mentioned in the last section. Specifically, when dealing with *in vivo* systems, past methods only demonstrated limited successes and encountered great difficulties such as particle damage (e.g., in dielectrophoresis of live cells), limited accessibility (e.g., in cell manipulation by optical tweezers), and inefficiency (e.g., in cell manipulation by acoustic waves). To overcome these difficulties, new manipulation methods are continuously being developed.

1.2.1 Active Particles

Inspired by the sci-fi movie “Fantasy Voyage”, scientists tried to develop a so-called “artificial micro-swimmer”, which can perform self-propulsion at a micro-scale without direct forcing from outside input. Based on this idea, many different micro-swimmers were developed, which could be actuated by bacteria, chemical reactions, and phase-change.⁸⁴⁻⁸⁵ Among these micro-swimmers, active particles have attracted great interest from researchers recently. The key feature of the so-called active particle is that it can absorb energies from a surrounding solution and perform self-propulsion without the existence of an external field. Such a feature makes it an ideal candidate

for applications in which the usage of external fields is difficult.

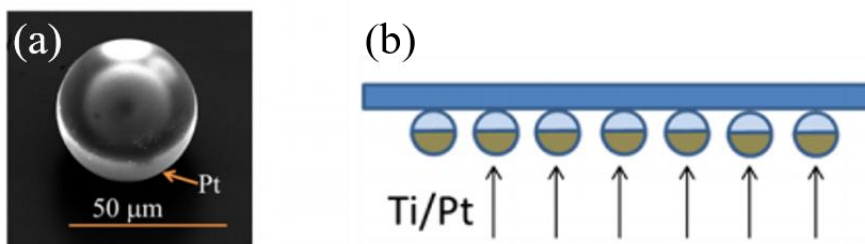


Figure 1-6. (a) A Janus catalytic micromotor half coated with platinum. (b) A schematic of the fabrication process of a Janus catalytic micromotor. Reproduced from Ref. 86 with permission.

The most commonly used active particle is a Janus catalytic micromotor (JCM) due to its easy fabrication process. JCMs are micro/nanoscale particles that feature a heterogeneous catalytic coating on their surface, as shown in Fig. 1-6. By using the catalytic reactions on their surfaces to break down the reactants in surrounding fluids, JCMs can “swim” autonomously *via* various mechanisms. Since achieving autonomous movement of small particulates has long been sought in diverse fields including biology and medicine, the demonstration of autonomous JCMs about a decade ago⁸⁷⁻⁸⁸ has since triggered intensive studies of JCMs and their dynamics.⁸⁹⁻⁹⁰ While the practical application of JCMs remains limited at present, autonomous JCMs have already been used successfully to sense, detect, and deliver micro/nanoparticles of various sizes and shapes.⁹¹⁻⁹³ With further development, JCMs can conceivably be used to execute more demanding tasks such as removing blood clots in capillaries and environmental remediation.⁹⁴⁻⁹⁵

The intensive experimental and theoretical studies on JCMs have tremendously improved the fabrication, operation, and understanding of JCMs. Several mechanisms including self-diffusiophoresis,⁹⁶⁻⁹⁷ self-electrophoresis,⁹⁸ and bubble propulsion⁹⁹⁻¹⁰¹ have been revealed to drive the movement of JCMs. Of these mechanisms, the self-diffusiophoresis and self-electrophoresis-

driven dynamics of JCMs have received the most attention. The effects of JCM design,¹⁰²⁻¹⁰³ operating conditions such as solution composition,¹⁰⁴⁻¹⁰⁵ geometrical confinement,¹⁰⁶⁻¹⁰⁷ and externally-imposed shear flows on the dynamics of JCMs have been explored in great detail.¹⁰⁸ For the applications of JCMs in drug delivery and microfluidics, geometrical confinement usually plays an important role on JCM dynamics. Because of the importance of boundaries, several studies recently have sought to understand the role of solid boundaries in determining JCM motion. Specifically, the self-diffusiophoresis of an active particle near a planar boundary has been explored *via* either experimental or theoretical methods.¹⁰⁹⁻¹¹³ For example, Uspal *et al.* investigated the self-propulsion of a catalytic active particle near a wall by combining analytical analysis and numerical simulations.¹⁰⁹ It was discovered that, depending on the choice of design parameters (catalytic coverage, surface mobility, etc.), the catalytic active particle shows different behaviors near a wall including reflection, steady sliding, and hovering. The authors suggest that the hydrodynamic effect of the wall is mainly responsible for the behaviors of the catalytically active particle. Ibrahim *et al.* captured the wall-induced distortion of solute concentration gradients, which caused wall-induced-diffusiophoresis of JCMs.¹¹⁰ Such wall-induced-diffusiophoresis promotes the translation of JCMs without affecting their rotation. Some of the simulation predictions have been observed experimentally such as by Kreuter *et al.*, who observed sliding and reflection of JCMs near channel walls.¹¹¹ In one most recent experimental study, boundaries are used to steer the motion of JCMs and eliminate the Brownian rotation of the JCMs.¹¹³

While previous research on JCMs has greatly improved the understanding of their dynamics in free solutions and near planar boundaries,^{97, 109, 114-115} the dynamics of JCMs in more complex environments remains to be clarified. For drug delivery and microfluidic applications, JCMs often must operate under confined conditions, e.g., multiple JCMs may come close to each other and

translate through a short micropore. Furthermore, most existing studies on the dynamics of JCMs use the quasi-static method and assume the system is in an equilibrium state at every instant. However, since the Peclet number may not necessarily be small in complex environments, this assumption is not always valid. Therefore, understanding the dynamics of JCMs in confined geometries is essential for facilitating realistic applications of JCMs.

Even though self-diffusiophoresis is very effective under certain circumstances, the movement of JCMs driven by these phoretic effects is typically slow, with a speed below a few tens of $\mu\text{m/s}$. A possible way of achieving faster movement of JCMs is through bubble propulsion.¹⁰¹ Specifically, when JCMs are submerged in a solution containing fuel molecules (e.g., H_2O_2), their catalyst surfaces break down fuels through catalytic reactions. If the products of this reaction are gaseous molecules, then bubbles can potentially form, grow, and collapse in the JCM system. Bubble propulsion-based JCMs can achieve speeds up to a few mm/s ,¹⁰⁰ which offers distinct advantages in applications where rapid movement is desired. In addition, the movement of bubble-propelled JCMs is less affected by the properties of liquid solutions (in particular its ionic strength) compared to that of the JCMs driven by diffusiophoresis and self-electrophoresis. Because of these and other reasons, there is a growing interest in developing bubble propulsion-based JCMs.

For bubble propulsion-based JCMs, the behavior of bubbles plays an essential role in their dynamics. First of all, whether or not bubbles exist in JCM systems dictates whether or not the JCM can be actuated by bubble propulsion.¹¹⁶ Secondly, the growth of the bubble, while it is attached to JCMs, can heavily influence the movement of JCMs. Indeed, if the bubble grows rapidly, the associated “growth force”, which originates from the inertia effects due to the displacement of fluids by the growing bubble, can dominate the movement of JCMs. Third, the collapse or burst of bubbles near a JCM can cause it to move at very high speed due to an

instantaneous local pressure depression. For example, it was observed that the burst of a bubble near a JCM leads to an instantaneous JCM speed of $\sim O(10 \text{ cm/s})$.⁸⁶ In addition, the fluid flow induced by the collapse of a bubble can entrain the neighboring JCMs and potentially change the direction of their movement.

While the important role of bubble behavior in determining the dynamics of JCMs is being recognized, research on the bubble behavior in JCM systems is quite limited. Prior experiments showed that the bubbles in JCM systems often showed anomalous behaviors compared to those formed in boiling experiments or in solution supersaturated by dissolved, incondensable gas. Specifically, many observations on the formation, growth, and collapse of bubbles are not yet well understood.

For bubble formation in JCM systems, a wide range of observations has been reported.^{86, 100-101, 116-119} For isolated JCMs (i.e., when JCMs are far away from each other), bubbles are typically observed only if the radius of the JCM is large, e.g., larger than about $10 \mu\text{m}$.^{86, 95, 120} Recently, it was discovered that whether or not bubbles form on the JCM surface also depends on the methods used to coat catalysts on the JCM's surface. For example, using chemical deposition to coat Pt on the JCM surface tends to create rougher surfaces (hence a larger liquid-Pt contact area for H_2O_2 decomposition), and, thus, bubbles can be observed even on isolated JCMs as small as $4 \mu\text{m}$.¹¹⁶ While visible bubbles usually do not form on small, isolated JCMs, recent studies show that, when a group of small JCMs forms a cluster, substrate-attached bubbles can be observed in the center of the cluster.¹⁰¹ Overall, the underlying mechanism of bubble formation in a JCM system is still not well understood and needs further study.

Another aspect of bubble formation in JCM systems is that various growth laws have been reported. Some studies reveal that, for a bubble attached to an isolated, large JCM, its radius during

growth follows a power law of $R \sim t^{0.33}$, which is consistent with the well-known direct injection mechanism reported for bubble growth near thin-wire electrodes.^{86, 117, 121} However, it is also reported that when a bubble is formed near a group of JCMs, its growth exhibits different behaviors. It is found that bubble growth fed by a ring of JCMs follows a power law of $R \sim t^{0.7 \pm 0.2}$. This unusual growth law is different from that for bubbles attached to individual JCMs ($\sim t^{0.33}$) and bubbles immersed in supersaturated bulk solutions ($\sim t^{0.5}$).¹²²⁻¹²⁵

Finally, some experiments show that the growth of the bubbles in JCM systems can be disrupted. In several recent studies, it was observed that when a bubble reaches some threshold size, it disappears in a very short period of time (< 1 ms).^{101, 116} This rapid collapse of the bubble is too fast to be explained by the diffusional dissolution mechanism.¹²⁶ While such a collapse process has been phenomenologically fitted to the Rayleigh-Plesset equation,^{86, 116} a mechanistic understanding of it is still lacking.

1.2.2 Magnetically Steered Surface Walkers

Another recently developed method for manipulating micro-particles in a liquid solution is that of magnetic surface walkers.^{56, 127-128} Unlike classical magnetophoresis, the motion of magnetic surface walkers is not directly caused by a magnetic field. Instead, the magnetic field is only used to steer the rotation of a micro-particle or a microstructure formed by magnetic particles. Such rotation, when coupled with hydrodynamic interactions between the particle and a nearby wall, can produce locomotion of the micro-particle and microstructure. For example, as shown in Fig. 1-7, driven by a rotating magnetic field method, a chain of magnetic particles can “tumble” along a solid surface to achieve particle translation. In 2010, Sing *et al.*¹²⁸ first demonstrated the locomotion of such a particle-assembled surface walker in a 30 Hz rotating magnetic field with a

velocity of $\approx 12 \mu\text{m/s}$. Their numerical analysis showed that this locomotion is mainly a result of the hydrodynamic interaction between the rotating particle(s) and a nearby solid boundary. Later, studies found the non-slip surface of a rotating particle assembly and a nearby static wall generated

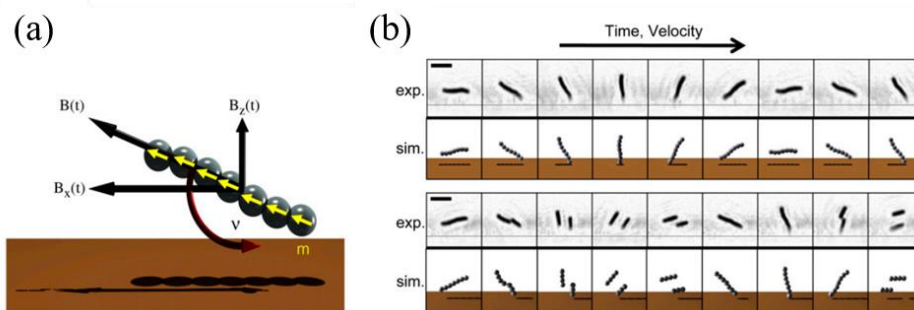


Figure 1-7. (a) The geometry of the “surface walker”. (b) Comparison of the particle trajectories obtained from experiments and simulations at different frequencies of the magnetic field (top: 5 Hz, bottom: 7 Hz). Reproduced from Ref. 128 with permission.

high shear in the solution layer between the assembly and wall, which created a propulsion force on the assembly.¹²⁹⁻¹³¹ Similarly, Zhang *et al.* used a rotating nickel microwire instead of a particle assembly to actuate and manipulate microbeads.¹³² The $10 \mu\text{m}$ long rotating nickel microwire they used could achieve a speed of $26 \mu\text{m/s}$ at 36 Hz. Kim *et al.* fabricated a double-bead microswimmer that could be driven using a 100 Hz homogeneous rotating H-field.¹³³ The double-bead microswimmer consisted of a $3 \mu\text{m}$ polystyrene micro-bead conjugated to a 150 nm magnetic nanoparticle via an avidin-biotin linker. It could rotate under a rotating H-field and the small magnetic bead would act as a propeller similar to the nanowire motor. In addition, based on the same mechanism, the so-called “magnetic carpet” is developed and used to transport cargos where particles within the assembly perform rotation individually instead of assembly-level rotation.¹³⁴

The magnetic surface walker shows great potential as a micro-particle manipulation method due to its programmable direction of motion and high speed. However, since it is a relatively new

technology, there are still some hurdles that need to be addressed before it can be used for applications in lab-on-a-chip or even *in vivo*. First, the transport speed of surface walker has a nonlinear dependence on the frequency of the applied rotating magnetic field, i.e., initially, the speed increases monotonically with the frequency and drops sharply above a critical frequency. One explanation of this nonlinear dependency is that, above the critical frequency, the assemblies can no longer maintain a phase lock with the rotating field due to the increasing viscous drag.⁵⁶ Such strong hydrodynamic viscous drag forces a phase lag¹³⁵ or even a phase ejection¹³⁶, which leads to the decrease of the transport speed of assemblies. Second, the confined geometries such as narrow channels tend to greatly affect the dynamics of the particle assemblies, which hinders using surface walkers *in vivo*. Other challenges also exist and need future study to solve them and improve the performance of surface walkers.

Among these challenges, one practical problem is that when a rotating magnetic field is used to induce the rotating of particle assemblies, at least two sets of the magnetic generator are required.^{128, 132, 137} This requirement increases both the volume and the cost of the system, which further hinders the application of the surface walker for particle manipulation. In addition, the particle assemblies also have to be designed into a specific configuration to adapt to the rotating magnetic field.

1.3 Open Questions and Scope of This Dissertation

As introduced in the sections above, past studies have greatly improved the understanding of particle dynamics in different microsystems and helped advance technologies for micro-particle manipulation. However, practical micro-particle manipulation methods for *in vivo* and bio-related applications are still lacking at present due to the limited understanding of the dynamics of micro-

particles in these complex systems. The overall objective of this dissertation is to advance the fundamental understanding of the dynamics of micro-particles in recently developed particle manipulation methods (specifically active particles and magnetically steered surface walkers) to facilitate their further development. This dissertation focuses on the dynamics of two types of micro-particles, i.e., systems featuring JCMs and magnetic particles. The main questions to be explored and answered for these systems are the following:

(1) How is the dynamics of JCMs affected by confined geometries? For example, how do JCMs translate through a micropore? Can a JCM enter a pore if it is not perfectly aligned with the pore axis? How do JCMs disturbed by an external stimulus or thermal fluctuation behave inside a pore? When multiple JCMs enter a pore, how will they affect the dynamics of each other?

(2) What are the physical mechanisms underlying the bubble behaviors observed in the JCM system, and how does the presence of bubbles affect the dynamics of the active particles? Specifically, what is the criterion for bubble formation in JCM systems? Why does the scaling law of bubble growth in JCM systems deviate from classical bubble growth laws? Why does a bubble disappear in an extremely short time scale in some experiments?

(3) Is it possible to actuate a magnetic surface walker without using a rotating magnetic field? If yes, what is the underlying mechanism of such a method? How does the translation speed of the particle depending on its size and shape and the characteristics of the external magnetic field (e.g., strength, frequency, and uniformity)?

The rest of this dissertation is arranged as follows:

In Chapter 2, the dynamics of JCMs under confined conditions are studied using numerical simulations. First, the mathematical model of self-diffusiophoresis of a JCM and its numerical

implementation are introduced and validated. Then, the translation of JCMs through narrow pores is systematically studied. Following that, the rotational dynamics of JCMs near a pore entrance and inside short pores are explored.

In Chapter 3, a new collective phenomenon of JCMs induced by a growing bubble is reported and analyzed. It is suggested that this collective motion of the micromotors, too fast for the diffusiophoresis, can be caused by the entrainment of micromotors by the evaporation-induced Marangoni flow near the bubble. Both scale analysis and numerical simulations confirm that the direction and strength of such Marangoni flow are consistent with the fast, collective motion of micromotors observed experimentally.

In Chapter 4, the peculiar behaviors of bubbles in a JCM system are studied by integrating analytical modeling and numerical simulations. The mechanisms of the formation of bubbles near an isolated JCM and near a cluster of JCMs are carefully examined. The unusual bubble growth and the ultra-fast collapse of bubbles in JCM systems are studied.

In Chapter 5, a new method of using alternating magnetic fields to manipulate small magnetic objects in fluids is studied. Different from the manipulation methods introduced above, only a single solenoid, which generates a non-uniform magnetic field, is used to actuate magnetic clusters. These clusters perform translational motions near substrate surfaces and move away from the solenoid that is used to generate the H-field. A theoretical model that combines surface effects and the magnetophoresis force is developed to understand such motion.

Finally, in Chapter 6, the key contributions of this dissertation are summarized.

Chapter 2. Self-Diffusiophoresis of Janus Catalytic Micromotors in Confined Geometries*

In this chapter, the dynamics of JCMs driven by self-diffusiophoresis in confined geometries are studied using numerical simulations. This chapter is organized as follows. First, the standard model of self-diffusiophoresis of JCMs¹¹⁵ is introduced and its numerical implementation are explained and validated. After the numerical implementations are validated, the translation of a single JCM through narrow pores is systematically studied and its dynamics is analyzed. Following this, the crowding effect of JCMs on their translation through a narrow pore is investigated by placing two aligned JCMs at the entrance of a narrow pore. Finally, the rotational dynamics of circular JCMs near pore entrance and inside short pores are explored. The effect of confinement and crowding on the dynamics of JCMs is examined and its implication for the future applications and development of active particles are presented.

2.1 Mathematical Model and Numerical Implementation

2.1.1 Model for Self-Diffusiophoresis

To focus on the dynamics of JCMs driven by self-diffusiophoresis, a spherical JCMs of radius R_{JCM} submerged in a solution (see Fig. 2-1) is considered. The JCMs are half-coated by catalysts that break down fuels in solution by chemical reaction. The reaction generates a concentration

* This chapter is adapted from the following paper (Ref. 138):

F. Yang, S. Qian, Y. Zhao, and R. Qiao, "Self-Diffusiophoresis of Janus Catalytic Micromotors in Confined Geometries", *Langmuir*, 2016, 32, 5580–5592.

Permission for using this paper in this dissertation has been granted by the American Chemical Society.

gradient of the reaction product along the JCM's surface. Such a concentration gradient induces an imbalance of interfacial forces near the JCM's surface, thus driving the self-diffusiophoresis of JCM. In practice, platinum is often used as catalytic material. If hydrogen peroxide is used as fuels, the product of the catalytic reaction is oxygen. Other fuels,¹³⁹⁻¹⁴⁰ which leads to different reaction products, can also be used. Here, to reduce the numerical difficulty, the transport of fuel is neglected and the concentration of fuels is assumed not deviate from the initial concentration notably in the simulations. This treatment is valid when the Damköhler number Da is small. Da is the ratio of the diffusion and reactive time scales, i.e., $Da = s\bar{L}/D_f C_f$, where s is the rate at which fuels are consumed on the catalytic surface, \bar{L} is the characteristic length scale involved in the supply of fuel to the catalytic surface, and D_f and C_f are the diffusion coefficient and concentration of fuel molecules, respectively. This study focus in the regime of $Da \ll 1$. Hence,

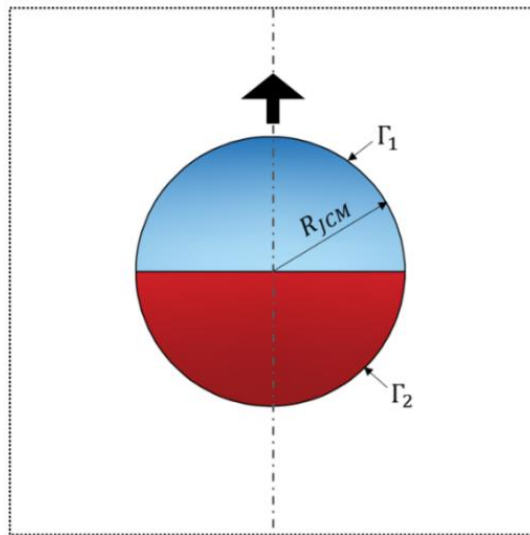


Figure 2-1. A schematic of the JCM. Half of the JCM's surface (Γ_2 , colored in red) is coated with catalyst while the other half of the JCM (Γ_1 , colored in blue) exhibits no catalytic reactivity. The large black arrow indicates the swimming direction of JCM due to self-diffusiophoresis when the product of the catalytic reaction interacts repulsively with the JCM.

the transport of the fuel does not need to be solved.

To describe the above self-diffusiophoresis of JCMs, the general model established previously is adopted.¹⁴¹⁻¹⁴³ Briefly, two sets of equations govern the reaction/transport of the reaction products and the movement of the fluids and the JCM. The concentration field of the reaction product (e.g. oxygen), c , is governed by the convection-diffusion equation

$$\frac{\partial c}{\partial t} + \mathbf{u} \cdot \nabla c = \nabla \cdot (D \nabla c) \quad (2-1)$$

where D is the diffusion coefficient of the reaction product and \mathbf{u} is the fluid velocity. The neutral (non-catalytic) surface of the JCM (i.e., Γ_1 in Fig. 2-1) is an impermeable wall, i.e.,

$$-D \nabla c(\mathbf{x}, t) \cdot \mathbf{n} = 0 \quad \text{on } \Gamma_1 \quad (2-2)$$

where \mathbf{n} is the unit normal vector of the surface. The generation of reaction products is taken into account through the boundary condition imposed on the catalytic surface (i.e., Γ_2 in Fig. 2-1)

$$-D \nabla c(\mathbf{x}, t) \cdot \mathbf{n} = \alpha \quad \text{on } \Gamma_2 \quad (2-3)$$

where α is the rate at which reaction products are generated on the catalytic surface.

The fluids are modeled as incompressible and Newtonian. Since the Reynolds number is small, the inertia effect is negligible. Thus the flow field is governed by

$$\nabla \cdot \mathbf{u} = 0 \quad (2-4)$$

$$\rho \frac{\partial \mathbf{u}}{\partial t} = -\nabla p + \mu \nabla^2 \mathbf{u} \quad (2-5)$$

where ρ and μ are the density and viscosity of the solution, and p is the pressure. The self-diffusiophoresis of JCM induced by the concentration gradient of reaction product is captured by imposing a phoretic slip on its surface.¹¹⁵ This treatment is valid in the thin-interaction layer

limit,¹¹⁴ i.e., $\lambda/L_c \ll 1$, where λ is the range of the interactions between the reaction product molecules (RPMs) and the JCM. L_c is the critical length scale in the diffusiophoresis process, e.g., the radius of the JCM (when JCM is in bulk solution) or the distance between the JCM surface and the surface of other JCM or walls. Typically, λ is of molecular dimension while L_c is hundreds of nanometers or larger. Hence $\lambda/L_c \ll 1$ holds in most situations. With the above treatment, the fluid velocity on the JCM's surface is given by¹¹⁴

$$\mathbf{u}(\mathbf{x}, t) = \mathbf{U} + \boldsymbol{\omega} \times (\mathbf{x}_s - \mathbf{x}_0) + \mathbf{u}_s \quad \text{on } \Gamma_1 \text{ and } \Gamma_2 \quad (2-6)$$

$$\mathbf{u}_s = M(\mathbf{I} - \mathbf{n}\mathbf{n}) \cdot \nabla c \quad (2-7)$$

where \mathbf{U} and $\boldsymbol{\omega}$ are the JCM's translational and rotational speed, \mathbf{x}_s and \mathbf{x}_0 are the spatial position for JCM surface and center, respectively. \mathbf{u}_s is the phoretic slip velocity. \mathbf{I} and M are the identity tensor and surface phoretic mobility. The mobility is given by⁹⁶

$$M = k_B T \lambda^2 / \mu \quad (2-8)$$

where k_B is the Boltzmann constant, T is the absolute temperature. For locally attractive/repulsive interactions between the reaction product and the JCM, the mobility M is negative (positive).

The translation and rotation of the JCM are governed by

$$m_{JCM} \frac{d\mathbf{U}}{dt} = \mathbf{F}_H \quad (2-9)$$

$$I_{JCM} \frac{d\boldsymbol{\omega}}{dt} = \mathbf{T}_H \quad (2-10)$$

where m_{JCM} and I_{JCM} are the mass and the moment of inertia of JCM, respectively. \mathbf{F}_H and \mathbf{T}_H are the force and torque exerted on the JCM by the fluids given by

$$\mathbf{F}_H = \int_{\Gamma_1 \cup \Gamma_2} \boldsymbol{\sigma}_H \cdot \mathbf{n} dS = \int_{\Gamma_1 \cup \Gamma_2} (-p\mathbf{I} + \mu(\nabla\mathbf{u} + (\nabla\mathbf{u})^T)) \cdot \mathbf{n} dS \quad (2-11)$$

$$T_H = \int_{\Gamma_1 \cup \Gamma_2} (\mathbf{x}_s - \mathbf{x}_0) \times (\boldsymbol{\sigma}_H \cdot \mathbf{n}) dS \quad (2-12)$$

where $\boldsymbol{\sigma}_H$ is the hydrodynamic stress tensor.

For the transport of JCMs in confined pores, the initial and boundary conditions for the reaction product concentration and fluid velocity must also be specified. Since these conditions are specific to each system to be studied, they are presented separately in the following sections.

2.1.2 Numerical Implementation and Validation

To solve Equ. 2-(1-12) simultaneously and thus predict the self-diffusiophoresis of JCMs, the commercial finite element package COMSOL was used.¹⁴⁴ The Arbitrary Lagrangian-Eulerian (ALE) method¹⁴⁵ was utilized to handle the movement of JCM and the evolution of reaction product concentration and flow fields, as has been done for simulation of electrophoresis of colloidal particles.¹⁴⁶ The computational domains were discretized using triangular elements, and the mesh was locally refined near the JCM surface and other solid boundaries (if present). During each simulation, multiple remeshing was typically performed to maintain the mesh quality. Mesh studies were also performed to ensure that the results are independent of the mesh size.

First, the translation of JCM in bulk hydrogen peroxide solutions is investigated, because this is a well-studied case, and compare the numerical solution to the analytical prediction by Howse *et al.*⁹⁶ Specifically, a spherical JCM with a radius of 1 μm was placed in the middle of a hydrogen peroxide (H_2O_2) solutions measuring 100 μm in radius and 200 μm in height, so that the JCM is effectively in a free solution. Oxygen is produced on the catalytic surface of the JCM at a constant rate of⁹⁶

$$\alpha = \alpha_2 \frac{[\text{H}_2\text{O}_2]_v}{[\text{H}_2\text{O}_2]_v + \alpha_2/\alpha_1} \quad (2-13)$$

where $\alpha_1=4.4\times 10^{11}\mu\text{m}^{-2}\text{s}^{-1}$, $\alpha_2=4.8\times 10^{10}\mu\text{m}^{-2}\text{s}^{-1}$, and $[\text{H}_2\text{O}_2]_v$ is the volume fraction of the fuel (H_2O_2) in the liquid solution. the mobility M is taken as $1.011\times 10^{-36}\text{m}^5/\text{s}$, consistent with previous reports.¹¹⁵ Initially, the fluids and the JCM are both stationary and the concentration of reaction product (oxygen) is zero everywhere. On the outer boundaries of the liquid solution, the zero stress condition was imposed for the fluid flow and the zero concentration condition was enforced for the reaction product. The self-diffusiophoresis of the JCM was simulated in the axisymmetric domain occupied by the liquid solution using the aforementioned model. During the simulation, the JCM reaches a steady velocity quickly (before it translates by $0.5\ \mu\text{m}$). The steady translation velocity for this problem has been predicted analytically as⁹⁶

$$U_a = \frac{M\alpha}{4D} \quad (2-14)$$

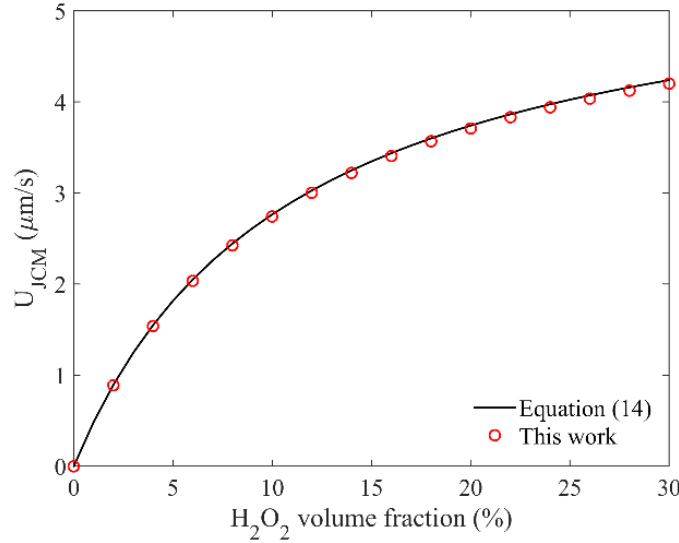


Figure 2-2. Diffusiophoresis velocity of a single JCM in bulk hydrogen peroxide solution predicted by the analytical model (Equ. 2-14) and numerical simulations.

Using the typical properties of O_2 and H_2O_2 solution ($D_{\text{O}_2}=2\times 10^{-9}\text{m}^2/\text{s}$, $\rho_{\text{H}_2\text{O}_2}=1.05\times 10^3\text{kg}/\text{m}^3$, $\mu_{\text{H}_2\text{O}_2}=1.02\times 10^{-3}\text{Pa}\cdot\text{s}$), the steady translation velocity of a JCM in a free solution is computed.

Figure 2-2 shows that the translation velocity predicted by the simulation agrees with that predicted by Equ. 2-14 very well.

Since how confinement affects the dynamics of JCMs will be studied in this work, this numerical implementation's capability of capturing dynamics of particles under geometrical confinement is next verified. The passive diffusiophoresis of a non-catalytic sphere inside a cylindrical pore is simulated (see Fig. 2-3 inset). Specifically, a sphere with a radius of R_s is positioned on the axis of a long, cylindrical pore with a radius of R_p and a length of L_p . The no-slip boundary condition is applied on the pore wall for the fluid velocity. If a concentration difference of a certain solute, Δc , exists at the pore's two ends, the sphere migrates along the pore axis *via* diffusiophoresis at a speed of¹⁴⁷

$$U_p = \frac{M\Delta c}{L_p} \left[1 - 1.290 \left(\frac{R_s}{R_p} \right)^3 + 1.896 \left(\frac{R_s}{R_p} \right)^5 - 1.028 \left(\frac{R_s}{R_p} \right)^6 + O \left(\left(\frac{R_s}{R_p} \right)^8 \right) \right] \quad (2-15)$$

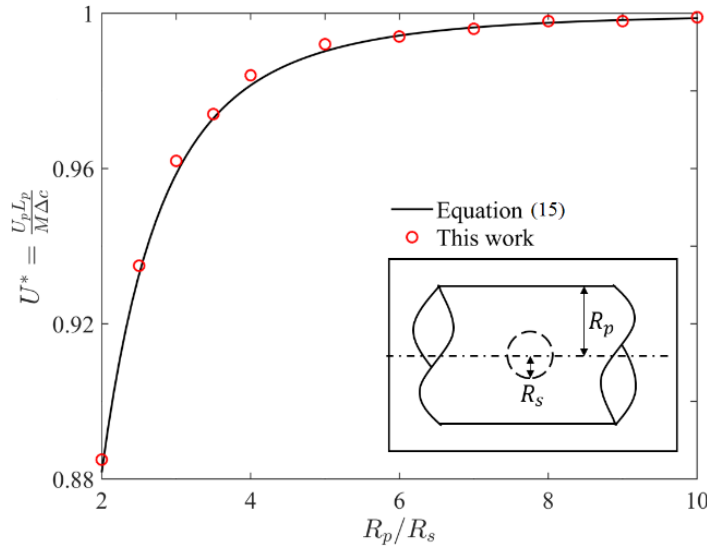


Figure 2-3. Passive diffusiophoresis velocity of a sphere in a long pore computed using simulations and using the analytical solution (Equ. 2-15). Inset is a schematic of the simulation model.

where M is the diffusiophoresis mobility of the sphere. Physically, as the particle radius R_s approaches R_p , the velocity reduces due to the confinement effects. In the simulations, a sphere with $R_s = 1 \mu\text{m}$ was placed in the middle of a cylindrical pore with $R_p = 2$ to $20 \mu\text{m}$. The length of the pore is $L_p = 40R_s$, the mobility M is $1.011 \times 10^{-36} \text{m}^5/\text{s}$ and Δc is $1 \text{mol}/\text{m}^3$. Figure 2-3 compares the sphere's normalized translation velocity $U^* = U_p L_p / M \Delta c$ in pores with various radii as predicted by the simulations and by Equ. 2-15. The good agreement between the computed translation velocity and the analytical solution verifies that the numerical methods and codes used here are accurate for simulation of diffusiophoresis of particles in confined geometries.

2.2 Results and Discussion

Using the mathematical model and numerical method introduced above, the self-diffusiophoresis of JCMs under confined conditions was studied. Both the translational and rotational dynamics of JCMs were examined to understand how confinement affects the dynamics of JCMs.

2.2.1 Translocation of a Single Spherical JCM Through a Short Pore

Here, the effect of confinement on the self-diffusiophoresis of spherical JCMs along the axis of a short cylindrical pore is studied. The system consists of a spherical JCM (radius R_{JCM} : $1 \mu\text{m}$; catalytic surface facing downward) and a cylindrical pore (radius: R_p ; length: L_p) connected to two large reservoirs (see Fig. 2-4). At $t < 0$, the center of the JCM is fixed at a distance of R_{JCM} from the pore's entrance. Fluids inside the system are at rest and free of reaction product. Note that, since the diffusion length of the reaction product per unit time is far larger than the distance from the JCM to the confining walls, the flow and reaction product concentration fields near the

JCM positioned at pore entrance reach steady state at time scale much shorter than the time scale associated with their diffusiophoresis through the pore. Hence, the initial conditions barely affect the transport of JCM. At $t = 0$, the JCMs start moving by self-diffusiophoresis. The reservoir boundaries were treated as free of hydrodynamic stress and reaction products. The no-slip and no-flux boundary conditions were enforced on the pore walls. In principle, there can exist phoretic slip on the pore wall due to the concentration gradient of the reaction products. Depending on the interactions between reaction product and pore wall and the local reaction product concentration gradient, such a phoretic slip can be in the same or opposite direction of the JCM's diffusiophoresis. This can lead to very rich JCM transport behavior in the pore, similar to the situation when electrophoresis of particles in pores is affected by electroosmotic flows near walls.¹⁴⁸ Here, in

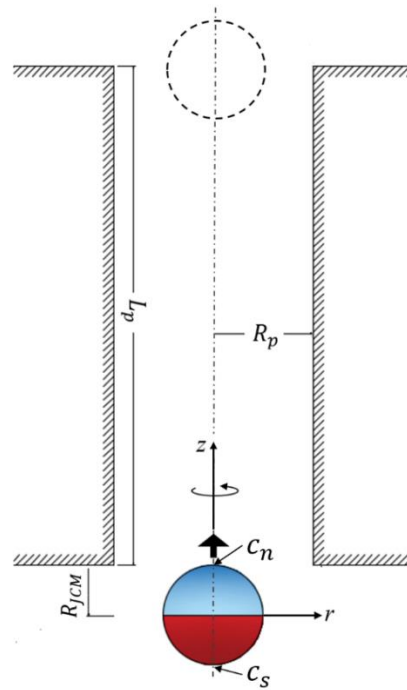


Figure 2-4. A schematic of a JCM translocating through a narrow pore. The JCM, with its catalytic surface facing the negative z -direction, is initially positioned at a distance of R_{JCM} from the pore's entrance. The large black arrow indicates the swimming direction of the JCM due to self-diffusiophoresis. The c_s and c_n are the product concentration at the south and north poles of JCM, respectively.

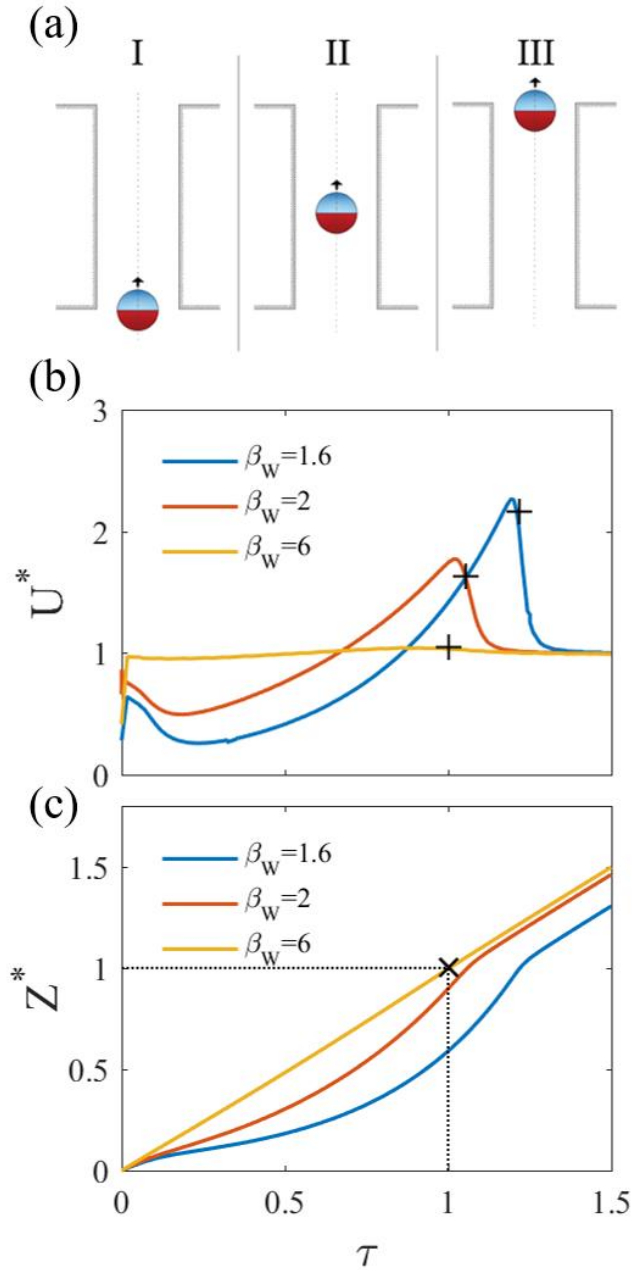


Figure 2-5. Translocation of a JCM through cylindrical pores with different radii but same length ($L_p = 20R_{JCM}$). (a) position of the JCM inside the pore at three time instants; (b-c) the evolution of JCM dimensionless velocity and JCM dimensionless traveling distance as the JCM “swims” through the pore. The plus signs in (b) mark the time instants at which the JCM exits the pore. A JCM completes its translocation through the pore when it reaches $Z^*=1$, and the corresponding time instant is marked using by “x” in (c).

order to focus on the effect of confinement, these complications are neglected and that the diffusio-phoretic slip on the pore wall are fully suppressed is assumed (e.g., by surface roughness or polymer coating).¹⁴⁹⁻¹⁵⁰

To study effects of confinement on JCM translation, both R_p and L_p are varied systematically. To first examine the effect of R_p , $\beta_W = R_p/R_{JCM}$ is gradually changed from 1.6 to 6, while keeping the pore length constant at $\beta_L = L_p/R_{JCM} = 20$. Hereafter, all variables are presented in dimensionless form. Velocity of the JCM U^* is scaled by the JCM's velocity in unbounded free solution, U_{JCM}^∞ , and JCM traveling distance Z^* is scaled by $L_t = L_p + R_{JCM}$, i.e., the distance traveled by the JCM when it fully translocate the pore (see Fig. 2-4). With these choice of reference length and velocity, the dimensionless time is constructed as $\tau = tU_{JCM}^\infty/L_t$, where L_t/U_{JCM}^∞ represents the time for a JCM to travel L_t in free solution.

Figure 2-5a shows the translation velocity of the JCM through various pores as a function of time. In all cases, after self-diffusiophoresis is enabled ($\tau = 0$), the JCM quickly achieves a velocity close to its steady velocity in free solution (i.e., $U^* = 1$). In a moderately narrow pore ($\beta_W = 2$), the evolution of the JCM's velocity shows three distinct stages (see Fig. 2-5a and b): when the JCM starts to enter the pore, its velocity decreases, reaching a minimum at $\tau < 0.25$; as the JCM moves deeper inside the pore and toward the exit, its velocity increases, and reaches a maximum before exiting the pore; as the JCM reaches the exit (marked by plus signs in Fig. 2-5b), its velocity decreases rapidly toward its steady-state velocity in the free solution. To understand such a non-monotonic evolution of the JCM velocity, note that the diffusio-phoresis of JCM is governed by the phoretic slip on its surface, which in turn depends on the gradient of the RPM along its surface. Since the latter gradient depends on the difference of the RPM concentrations $\Delta c_{sn} = c_s - c_n$ at the catalytic south pole c_s and uncoated north pole c_n (cf. Fig. 2-4), this difference and its evolution

with time are examined in Fig. 2-6a and 6b. In all figures, Δc_{sn} is normalized by the difference of the product concentrations at south and north poles of a JCM in free solution Δc_{sn}^∞ . The c_s and c_n are normalized by the product concentration at the north pole of a JCM in free solution c_n^∞ .

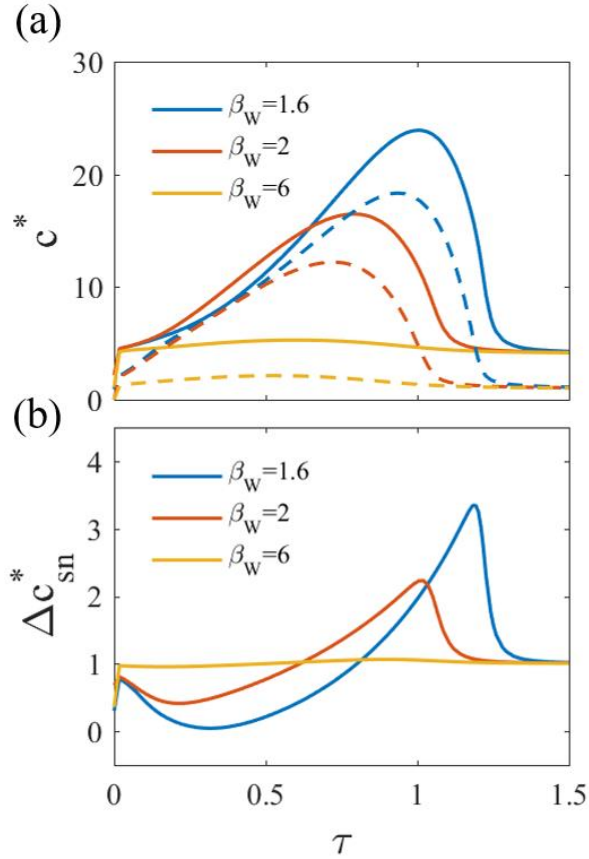


Figure 2-6. The reaction product concentration at the south and north poles of the JCM. The evolution of c_s^* (solid line) and c_n^* (dashed line) (a), and the difference of reaction product concentration at the south and north poles of the JCM (b) as the JCM “swims” through the pore.

Figure 2-6b shows that for $\beta_w = 2$, when the JCM just enters the pore, Δc_{sn}^* , decreases, which is consistent with the gradual decrease of U^* observed in Fig. 2-5a. As the JCM moves into the pore, the concentrations of reaction product at both its south and north poles increases because the diffusion of the RPMs toward the reservoir is hindered by the pore walls, leading to a buildup of

RPMs on JCM surface (see Fig. 2-6a). However, c_s^* (solid line) increases slower than c_n^* (dashed line). This is because the transport of RPMs away from the south pole of JCM, which faces a large reservoir nearby, is more efficient than from the north pole, which faces the interior of a long pore (see Fig. 2-5a's inset I). Consequently, Δc_{sn}^* decreases as the JCM moves toward the pore interior (see Fig. 2-6b) and the self-diffusiophoresis of JCM weakens. In response, JCM slows down. However, as the JCM moves deeper into the pore (see Fig. 2-5a's inset), Δc_{sn}^* increases because the product molecules generated on the catalytic surface are confined more near the catalytic surface and transported less to the uncoated surface due to the confinement by pore walls. Consequently, the JCM speeds up as shown in Fig. 2-5b. Finally, when the JCM starts to move out of the pore (see Fig. 2-5a's inset III), the concentration of reaction products near its south pole drops rapidly due to their efficient transport toward the large reservoir, leading to a rapid decrease

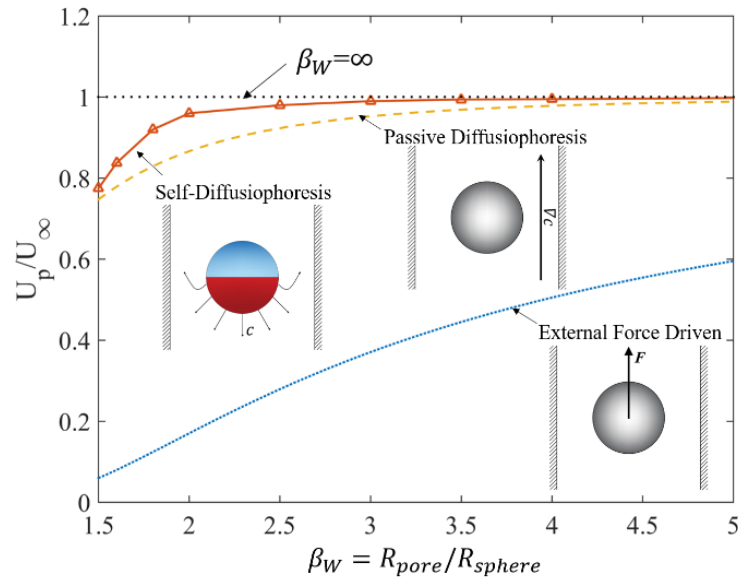


Figure 2-7. Comparison of the average speed of sphere through pores driven by different mechanisms as a function of confinement $\beta_W = R_p/R_s$ (R_p and R_s are the radius of the pore and sphere, respectively). For each transport mechanism, the average speed of the sphere inside a pore U_p is scaled using the sphere's speed in the free solution, U_∞ . Insets are the sketches of different particle transport mechanisms.

of Δc_{sn}^* and the JCM velocity toward their values in free solutions.

When the pore becomes narrower ($\beta_W = 1.6$), effect of confinement on the transport of RPMs becomes stronger and Δc_{sn}^* exhibits much larger variation as the JCM enters and leaves the pore (see Fig. 2-6b). These variations of Δc_{sn} modify the translation of JCM through the same physics discussed above, but the effects are more pronounced, e.g., the maximal speed of the JCM, which is achieved when the JCM is about to exit the pore, is 2.25 times of that in free solutions (see Fig. 2-5b). On the other hand, as the pore becomes wider ($\beta_W = 6$), the effect of confinement on JCM dynamics diminishes: the velocity of the JCM changes only slightly as the JCM passes through the pore and the JCM velocity and the translocation time are hardly affected by the presence of the pore walls (see Fig. 2-5b and c).

Overall, the translocation of JCMs through the pore is slowed down rather modestly by the confinement. In fact, the slowdown of self-diffusiophoresis by confinement is weaker compared to that for the particle transport driven by other well-known mechanisms. Figure 2-7 compares the average speed of spheres traveling through narrow pores driven by self-diffusiophoresis, external body forces,¹⁵¹ and passive diffusiophoresis.⁴⁴ In later two cases, the motion of the non-catalytic sphere is induced by an external body force and an externally imposed concentration gradient of certain solute (see the insets of Fig.2-7), respectively. For the self-diffusiophoresis of a sphere through a short pore, its average speed is defined as the mean velocity during its translocation through the pore. For transport by the latter two mechanisms, the pore is infinitely long and Stokes flow is assumed; for self-diffusiophoresis, the pore length is fixed at $20R_{JCM}$. Observing that, for $\beta_W = 2$, the velocity of a sphere driven by external force is 82% smaller than that in free solutions. Such a significant slowdown is caused by the enhanced hydrodynamic drag in narrow pores.¹⁵¹ For the passive diffusiophoresis in the same pore, its speed decreases less significantly, by 11%.

This is because, for a given externally imposed concentration gradient of solutes (usually imposed at distance away from the sphere), the solute concentration gradient near the sphere is greatly enhanced when it is confined inside a pore. This enhances the phoretic driving force and counteracts the enhanced hydrodynamic drag caused by confinement.⁴⁵ For self-diffusiophoresis

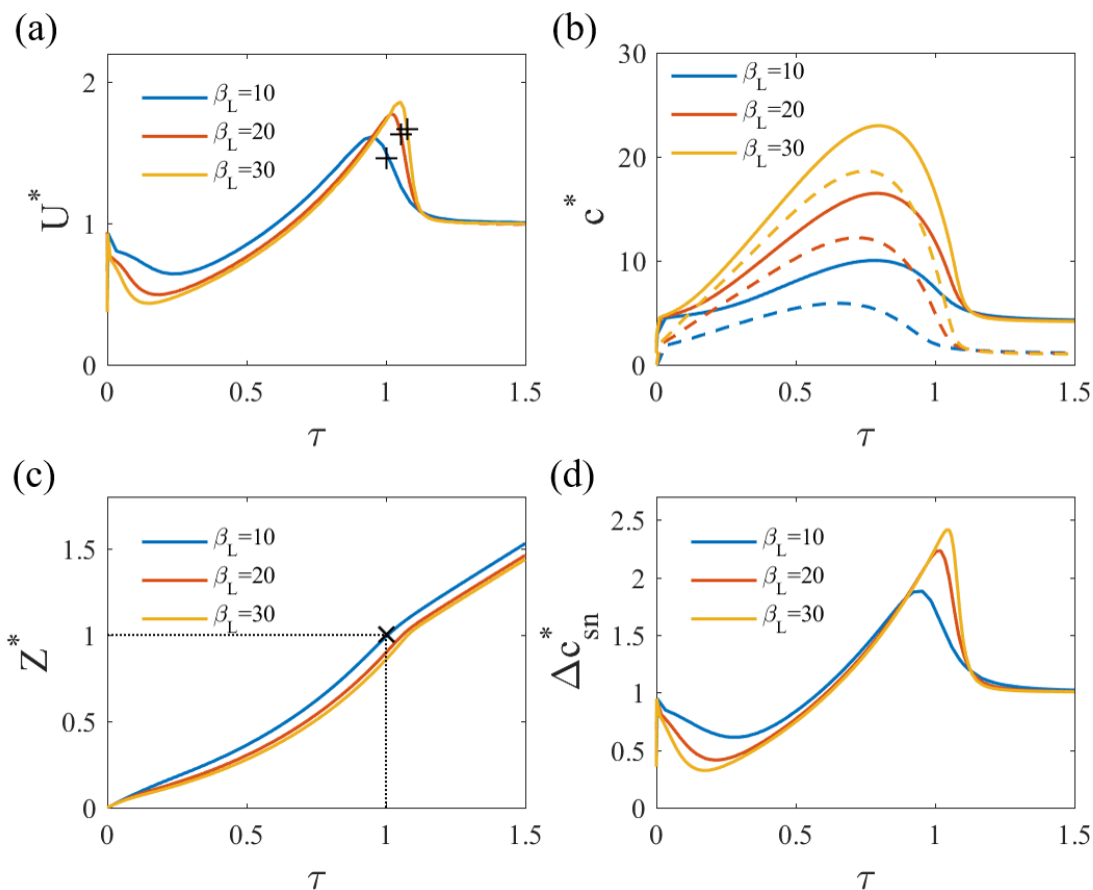


Figure 2-8. Translocation of a JCM through cylindrical pores with different lengths but the same radius ($R_p = 2R_{JCM}$). The evolution of JCM dimensionless velocity (a), the c_s^* (solid line) and c_n^* (dashed line) (b), JCM dimensionless position (c), and the difference of reaction product concentration at the south and north poles of the JCM (d) as the JCM “swims” through the pore.

of a JCM in the same pore ($\beta_w = 2$), the slowdown by confinement is even weaker ($\sim 4\%$). This can be understood as follows. First, since the RPMs are generated on the JCM’s catalytic surface and

they must diffuse toward the two ends of the pore, their concentration near the JCM's catalytic surface increases when the pore size reduces. This tends to enhance the concentration gradient of reaction product on the JCM's surface more greatly compared to the situation in passive diffusiophoresis. Second, for the translocation of JCM through a short pore by self-diffusiophoresis, the JCM travels faster than in free solution when it approaches the pore's exit, which partially compensates the slowdown of JCM near the pore entrance (see Fig. 2-5b). Since this feature is absent for passive diffusiophoresis of a sphere in a long pore, the overall slowdown is weaker for self-diffusiophoresis. Figure 2-7 also shows that when a pore becomes very narrow (e.g., $\beta_W=1.5$), and the average speed of particle transport by self-diffusiophoresis becomes similar to that by passive diffusiophoresis. This is likely because, for very narrow pores, the pore entrance greatly slows down the JCM as it enters the pore (see Fig. 2-5b), hence the JCM takes longer time to translocate the pores. On the other hand, the passive diffusiophoresis of particle is measured inside infinitely long pores and, therefore, not affected by such an entrance effect. From the above discussions, it is clear that the self-diffusiophoresis of JCMs in confined geometries exhibits interesting new features compared to other forms of particle transport in similar geometries. Identifying and understanding these features are useful for improving the performance of micro-systems in which self-diffusiophoresis is used for particle transport.

Next, the effect of pore length L_p on the JCM translocation through pores is examined by varying $\beta_L = L_p/R_{JCM}$ between 10 and 30, while fixing $\beta_W = 2$. Figure 2-8a shows that, in all pores, the three stages of JCM translocation, during which the JCM velocity varies non-monotonically, are still observed. In longer pores, the initial slowdown of JCM is more significant, consistent with the greater decrease of Δc_{sn}^* in the longer pores during this stage (see Fig. 2-8d). The latter is mostly caused by the fact that, in longer pores, RPMs build up more easily near the

north pole of the JCM (see Fig. 2-8b), which faces the interior of the pore. In longer pores, the increase of the JCM speed once it is deep inside the pore is also more obvious. For example, the maximal velocity of JCM inside a pore increases by 15% when β_L increases from 10 to 30. This is because, in longer pores, the build-up of the RPMs near the catalytic surface is more significant due to the less effective transport of these molecules from these pores to reservoir and the longer time the JCM spends inside these pores. Overall, Fig. 2-8c shows that, in moderately narrow pores ($\beta_L = 2$), the average speed of the JCM decreases only slightly as the pore becomes longer: as β_L increases from 10 to 30, the time for JCM to translocate through the pore increases by 8%, i.e., the average speed of the JCM inside the pore decreases by 8%.

The above discussion revealed that the translocation of JCMs through pores is governed by the complex interplay between hydrodynamics in confinement and the transport of reaction products near the JCM and inside the pores. The weak dependence of the JCM's average translocation speed on the pore size and length is due to the rather strong cancellation effects of these processes. From an application perspective, the fact that a JCM's average translocation speed is affected weakly by confinement of pore walls helps simplify its design for transport in pores because its velocity in free solutions can be used to estimate its translocation. It should, however, be cautioned that these results are obtained under the condition that the reaction rate is a constant, i.e., the effect of consumption of fuel on the reaction rate is assumed to be small. As discussed earlier, this assumption is reasonable when $Da = s\bar{L}/D_f C_f \ll 1$. Because the pore length is the most relevant length scale for fuel transport inside a pore, it follows that the above results on JCM dynamics in pores hold for pores with pore length smaller than $D_f C_f / s$. For much longer pores, the effects of fuel transport must be considered in analyzing the JCM dynamics.

2.2.2 Translocation of a Pair of Spherical JCMs through a Short Pore

In practical applications and many recent experiments, many JCMs could co-exist in the system.^{92, 152-153} Because of the “crowding” of JCMs in these systems, the dynamics of individual JCMs can be affected greatly by the interactions between the JCMs. Here the translocation of a pair of JCMs through a cylindrical pore is considered to gain insights on how interactions between

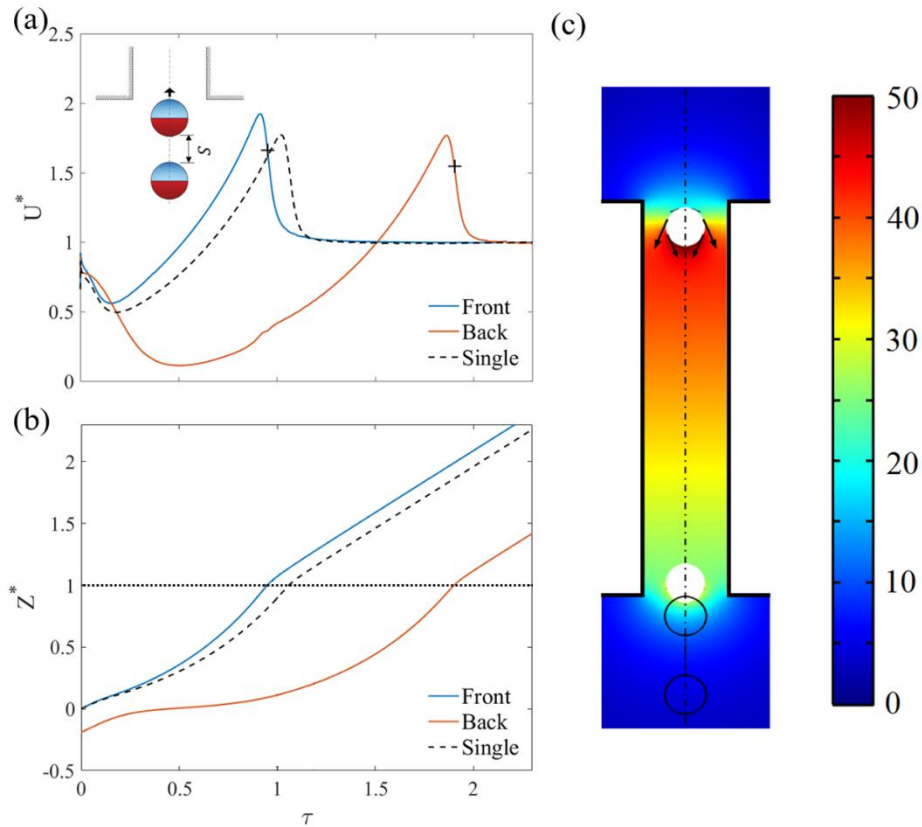


Figure 2-9. Translocation of a pair of JCMs through a short pore. (a-b) Evolution of the velocity (panel a) and the position (panel b) of each JCM as a function of time. The dashed line is the result of single JCM translocation through the same short pore from Fig. 2-5. A JCM completes its translocation through the pore when it reaches $Z^*=1$. (c) Reaction product concentration field at $\tau = 0.9$, when the front JCM is about to exit the pore (the JCMs are marked by the white circles). The black circles denote the initial positions of the JCMs. The arrows denote the slip velocity on the JCMs' surface.

JCMs affect their transport in confinement. Specifically, two JCMs ($R_{JCM} = 1 \mu m$) are positioned near the entrance of a short cylindrical pore ($R_p = 2R_{JCM}$; $L_p = 20R_{JCM}$), with their axes aligned with the pore's axis. The pore is open to large liquid solution reservoirs (length: $50R_{JCM}$; radius: $50R_{JCM}$) at both ends. The distance between the center of the JCM closer to the pore and the pore entrance is R_{JCM} . The separation between the JCMs is $2R_{JCM}$ and the catalytic surfaces of both JCMs are facing downward (see Fig. 2-9a's inset). The interactions between JCMs are relatively strong under these conditions, but it is verified in separate simulations that varying the distance between JCMs does not qualitatively change the results. The initial conditions and boundary conditions are similar to those in previous section, e.g., the JCMs are at rest for $\tau < 0$ and allowed to move by self-diffusiophoresis at $\tau = 0$.

Figure 2-9a shows the evolution of the velocity of the two JCMs (hereafter, the JCM entering the pore first is termed the front JCM, while the other JCM is termed the back JCM) as they pass through the pore. The evolution of the velocity of both JCMs exhibit the same trend found during the translocation of single JCMs through the pore (dashed line in Fig. 2-9), i.e., as a JCM passes through the pore, the slowdown-speedup-slowdown cycle of its velocity is preserved qualitatively. There are, however, quantitative differences between the dynamics of the JCMs studied here and in Fig. 2-5a. Compared to the situation when a single JCM passes through the pore, for the front JCM, its initial slowdown terminates at an earlier time, its subsequent speedup is more significant (Fig. 2-9a), and its translocation time is $\sim 12\%$ shorter (Fig. 2-9b). For the back JCM, it slows down much more greatly as it enters the pore and becomes nearly stalled; while its speed does increase later and nearly reaches the maximal velocity of a single JCM passing through the same pore (Fig. 2-9a), its net translocation time is 50% longer than that of a single JCM passing through the pore (Fig. 2-9b). Overall, the pairing of JCMs affects the translocation of the front and the back JCMs

very differently: it weakly accelerates the translocation of the front JCM, but greatly slows down the translocation of the back JCM.

The different behavior of JCMs passing through a pore as pairs and as singlets and the different effects of JCM pairing on the translocation of the front and back JCMs originate mostly from the “chemical interactions” between a pair of JCMs translocating a pore. The pairing of JCMs inside a narrow pore leads to a concentration field of the reaction product shown in Fig. 2-9c. Because of pairing, the concentration of RPM near the catalytic surface of the front JCM is enhanced greatly, which enhances the strength of diffusiophoresis of the front JCM (see the phoretic slip velocity \mathbf{u}_s indicated by the black arrows in Fig. 2-9c). Meanwhile the concentration of RPM near the non-catalytic surface of the back JCM is elevated by the pairing of JCMs, which weakens the phoretic slip on the surface of the back JCM and thus slowing down its translocation. The “chemical interactions” between adjacent JCMs confined in narrow pores may be useful in designing complex system for particulate transport, e.g., they may be harnessed to accelerate or block the motion of a certain group of particles, hence useful for local control of system behaviors.

2.2.3 Rotational Dynamics of Circular JCMs Near and in Short Pores

In free solutions, self-diffusiophoresis drives a JCM to move in the direction defined by the vector pointing from the apex of its catalytic surface to the apex of its non-catalytic surface. For convenience, this vector can be identified as the “phoretic axis” of the JCM (identified as \mathbf{r}_{sn} in Fig. 2-10). In the above discussions, all spherical JCMs are positioned with their phoretic axes coinciding with the pore’s axis and thus they do not experience rotation. In practice, however, the phoretic axis of JCMs may not be fully aligned with the pore’s axis, e.g., due to thermal fluctuations or forces imposed by external magnetic fields.¹⁵⁴ Therefore, it is important to

understand how JCMs' orientation affects their transport into and through pores. Here, the transport of single JCMs in two scenarios in which their axes are not always fully aligned with the pore axis is studied. Since simulation of particle transport in confined space, in which a particle can approach the pore wall closely, is expensive, all simulations are performed in two dimensional spaces to explore the circular JCMs' translation and rotational dynamics. Note that prior studies of the electrophoresis of charged particles in microchannel revealed that the rotation of particles driven by phoretic effects can be indeed captured quite well in two dimensional simulations.¹⁴¹⁻¹⁴³

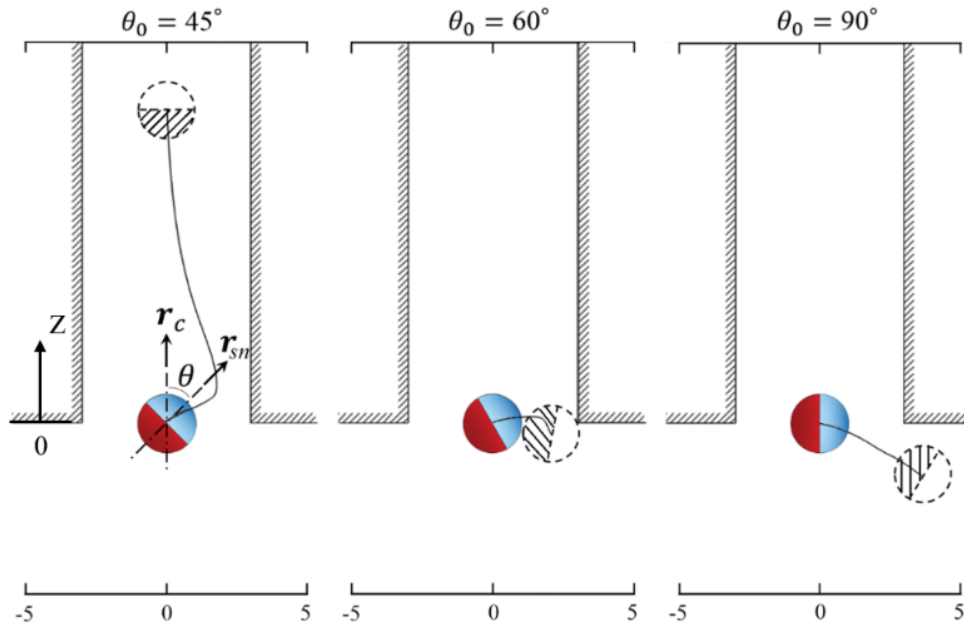


Figure 2-10. Trajectories of JCMs with different initial inclination angles θ_0 near a pore's entrance. The JCM's center is initially positioned at $z=0$. For small θ_0 , the JCM can rotate toward the pore interior and swim into the pore. For large θ_0 , the JCM either collides with the pore wall or swim away from the pore.

In this first scenario, a circular JCM is initially positioned at the entrance of a pore with its center on the pore's axis and its phoretic axis forming an inclination angle θ_0 with the pore's axis (identified as r_c in Fig. 2-10). The JCM has a radius of $R_{JCM} = 1 \mu m$ and the pore has a width of $6R_{JCM}$ and a length of $50R_{JCM}$. Two large reservoirs are included at the pore's two ends. The pore

walls are treated as no-slip and non-permeable surfaces. At $\tau = 0$, the entire system is free of RPM and both the fluids and the JCM have zero velocity. At $\tau > 0$, the JCM is allowed to move by self-diffusiophoresis.

Figure 2-10 shows the trajectories of the JCMs with different initial inclination angles θ_0 . The dynamics of the JCM greatly depends on θ_0 . For small θ_0 (e.g., $\theta_0 = 45^\circ$), initially, the JCM mostly moves toward the right pore wall with little rotation. Once it is close to the pore's right wall, the JCM rotates rapidly in the counter-clockwise direction and turns into the pore and its phoretic axis become aligned with the pore's axis. For large θ_0 (e.g., $\theta_0 = 60^\circ$ and 90°), the initial stage of JCM movement is similar to that for small θ_0 . However, by the time the JCM is close to the right pore wall, the JCM rotates in the clockwise direction. This rotation causes the JCM's phoretic axis to become less aligned with the pore's axis, and the JCM either collides with the pore entrance ($\theta_0=60^\circ$) or swims toward the reservoir ($\theta_0=90^\circ$).

To understand these observations, note that the rotation of a JCM is determined by the net torque acting on it, which in turn depends on the distribution of the viscous stress on its surface (see Eqn. 2-12). The viscous stress at any point on a JCM's surface scales as $\sigma_s \sim \mu u_t / \ell$, where u_t is the local fluid velocity tangential to the JCM's surface and ℓ is the length over which the fluid velocity decays to zero as one moves away from the JCM's surface. For a JCM near pore walls, ℓ can be taken as the distance from the JCM surface to the nearest wall, L_{sw} . Given that the velocity of fluids on the JCM surface is usually dominated by the phoretic slip velocity u_s , $\sigma_s \sim \mu u_s / L_{sw}$ is obtained. The part of a JCM's surface on which the phoretic slip velocity u_s points in the counter-clockwise (clockwise) direction with respect to its center experiences a local stress in the clockwise (counter-clockwise) direction, and is defined as Γ_c (Γ_{cc}) and labeled by green (yellow) curves in Fig. 2-11. Based on these analyses, the local viscous stress on JCM's surface is likely controlled

by two effects: the chemical effect and the hydrodynamic effect. The chemical effect refers to the fact that the viscous stress depends on u_s , which is determined by the tangential gradient of chemical species (in this case, the product of the catalytic reactions) on the JCM's surface as shown by Eqn. 2-7. The chemical effect depends strongly on the transport of the reaction products, which is affected by the confinement by pore walls. The hydrodynamic effect refers to the fact that, for a given u_s , the local viscous stress depends on the fluid flow near the JCM's surface, or roughly the distance from the JCM surface to the nearest pore wall as pointed out above.

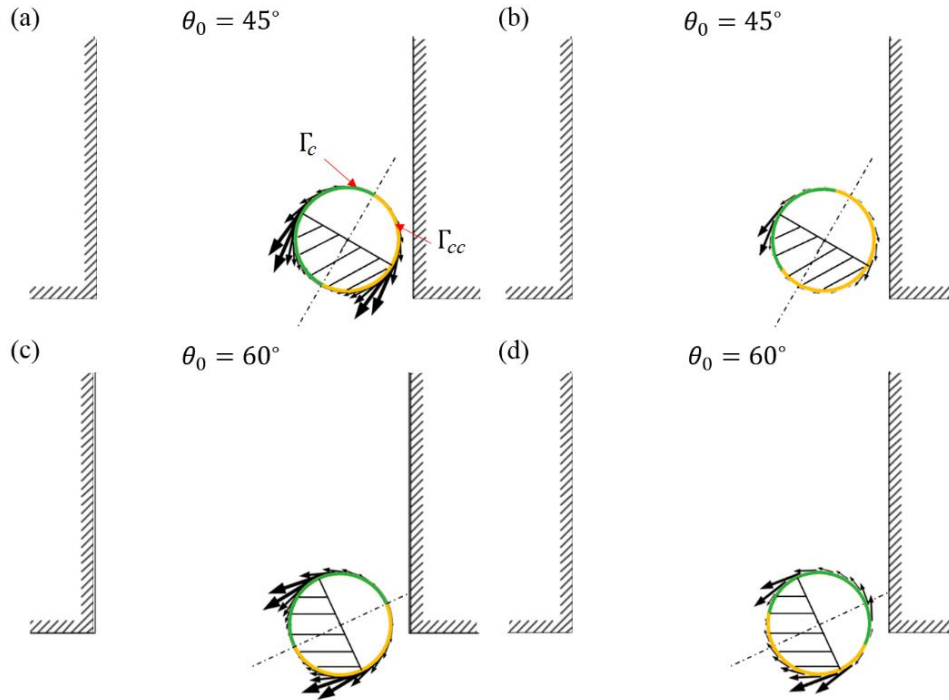


Figure 2-11. Distribution of the phoretic slip velocity u_s on the surface of JCMs when they approach the pore wall. Each JCM is originally placed at the pore entrance with an inclination angle θ_0 as shown in Fig. 2-10. The surface on which u_s points in the clockwise (counter-clockwise) direction with respect to the JCM center and the local viscous stress causes a counter-clockwise (clockwise) torque is defined as Γ_{cc} (Γ_c). In (a) and (c), u_s is taken, hypothetically, to be that for JCM in the free solution to isolate the hydrodynamic effect on JCM rotation. In (b) and (d), the real u_s determined in simulations is shown to help delineate the chemical effects on JCM rotation.

Both hydrodynamic and chemical effects contribute greatly to the dependence of a JCM's rotation on its initial inclination angle θ_0 . For clarity, the pure hydrodynamic effect is first examined. To this end, the phoretic slip velocity u_s (black arrows in Fig. 2-11) on the surface of a JCM is assumed to be identical to that when the JCM is located in unbounded free solution regardless its location and orientation in the system. When a JCM is placed at the entrance of the pore with $\theta_0 = 45^\circ$, initially, the JCM swims toward the pore wall with little rotation. Once JCM is near pore wall (e.g., at $\tau = 0.34$, see Fig. 2-11a), the viscous stress σ_s on the Γ_{cc} surface becomes larger than that on the Γ_c surface: while the slip velocity distribution on the Γ_{cc} and Γ_c surface is the same, L_{sw} is smaller on the Γ_{cc} surface than on the Γ_c because of the small inclination angle of the JCM. As a result, the net torque generated by the viscous stress on the Γ_{cc} surface is stronger than that on the Γ_c surface, and the JCM rotates in the counter-clockwise. Next the role of chemical effects in the rotation of the JCM is examined. To this end, recall that confinement affects the transport of reaction product near the JCM and thus the u_s distribution on JCM's surface. In Fig. 10b, the real u_s (black arrows) on the JCM's surface at $\tau = 0.34$ is plotted. The area of the JCM's surface (yellow) on which u_s points to the clockwise direction is larger than the area of the JCM's surface (green) on which u_s point to the counter-clockwise direction, i.e., Γ_{cc} is larger than Γ_c . The larger area of Γ_{cc} than Γ_c tends to increase the net torque exerted on the JCM in the counter-clockwise direction, and thus the JCM rotates in the counter-clockwise direction and swims deeper into the pore.

For the JCM with an initial inclination angle of $\theta_0 = 60^\circ$, again the pure hydrodynamic effects is considered. Figure 2-11c shows the sketch of the JCM at $\tau = 0.24$, in which the slip velocity u_s on the JCM's surface is taken as that for JCM in free solution. In this case, because of its large θ_0 , most of the Γ_{cc} surface faces the reservoir instead of right pore wall and most of the Γ_c surface

faces the pore interior, which are in sharp contrast with the situation for the JCM with $\theta_0=45^\circ$ (see Fig. 2-11a). As a result, the L_{sw} for the majority of the Γ_{cc} surface is larger than that for the majority of the Γ_c surface. Hence the viscous stress is stronger on the Γ_c surface than on the Γ_{cc} surface, and the resulting net torque drives the JCM to rotate in the clockwise direction. The chemical effect is examined by considering the real phoretic slip velocity u_s on the JCM surface (see Fig. 2-11d). Compared to those shown in Fig. 10c, the area of the Γ_c surface facing the pore interior/wall and the area of the Γ_{cc} surface facing the reservoir both increases. Consequently, the L_{sw} on the Γ_{cc} surface increases, while the L_{sw} on the Γ_c surface decreases. These changes enhance (reduce) the viscous stress on the Γ_c (Γ_{cc}) surface and increase the net torque acting on the JCM in the clockwise direction. Hence, the chemical effect further enhances the clockwise rotation of the JCM.

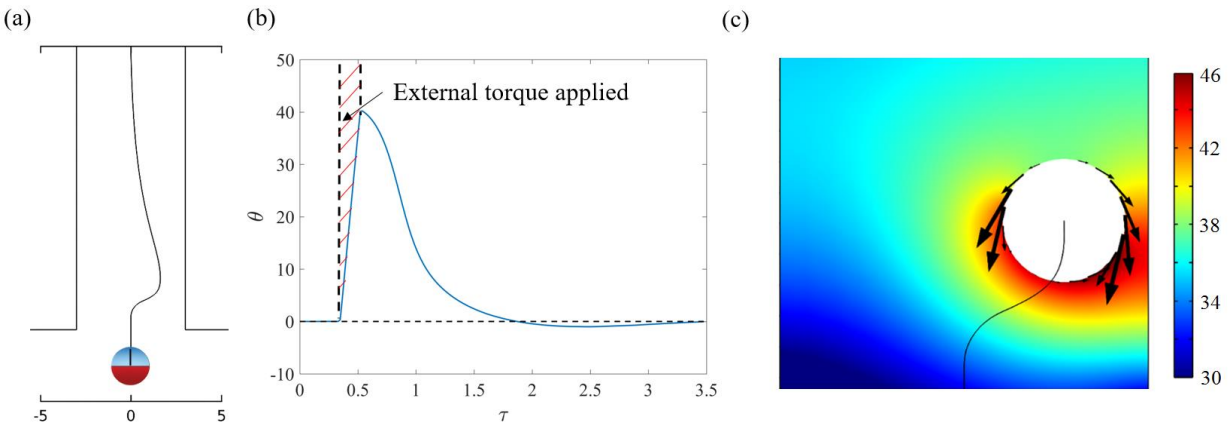


Figure 2-12. The self-alignment behavior of JCM swimming inside a pore. The JCM was initially placed near the pore entrance with phoretic axis fully aligned with the pore axis. An external, clockwise torque was applied on the JCM during $\tau=0.34-0.52$ to rotate the JCM in the clockwise direction. (a-b) The trajectory (a) and the inclination angle (b) of the JCM as a function of time. (c) The distribution of the reaction product near the JCM at $\tau=0.87$. The black arrows denote the phoretic slip velocities on the JCM's surface.

For $\theta_0 = 90^\circ$, the mechanism of the rotational motion of JCM is similar to $\theta_0 = 60^\circ$. The imbalance of stress distribution causes net, clockwise torque acting on the JCM and drives it to rotate in clockwise direction. However, because of the larger initial inclination angle, the JCM swims toward the reservoir instead of colliding with the pore wall.

In this second scenario, the rotation of a JCM inside a pore when its phoretic axis becomes misaligned with the pore axis is studied. As shown in Fig. 2-12a, initially a JCM swims toward a pore entrance with its phoretic axis fully aligned with the pore axis. At $\tau = 0.34$, when the JCM is inside the pore, an external torque is applied on the JCM for 1s, forcing it to rotate in the clockwise direction. At $\tau = 0.52$, the inclination angle of the JCM reaches 40° . The external torque is then removed and the JCM swims solely by self-diffusiophoresis. This problem mimics the situation in which the JCM become misaligned with the pore axis due to reasons such as thermal fluctuations. The size of the JCM, the pore, and the reservoir are the same as those in the scenario 1.

Figure 2-12 shows the trajectory of the JCM and its inclination angle as a function of time. The JCM exhibits a self-alignment behavior after the external torque was removed: (1) it moves away from the right pore wall and its inclination angle decreases, (2) eventually, the JCM becomes centered across the pore with its phoretic axis aligned with the pore axis. The first observation is similar to that observed when a JCM approaches an open, planar wall with its phoretic axis initially forming an angle less than 90° .¹⁰⁹⁻¹¹⁰ This self-alignment behavior is a result of the combined chemical and hydrodynamic effects. When the JCM deviates from the pore axis and approaches the right pore wall as shown in Fig. 2-12a, the distance between the JCM's surface facing the right wall decreases, and hydrodynamics effects causes the viscous stress $\sigma_s \sim \mu u_s / L_{sw}$ on this surface to increase. Meanwhile, the phoretic slip velocity on the JCM's surface facing the right wall increases due to chemical effects, and thus enhances the viscous stress on this surface. The

increased viscous stress on the JCM's surface facing the right wall leads to a net counter-clockwise torque acting on the JCM. Such a net torque drives the JCM to rotate in counter-clockwise direction so that its phoretic axis becomes more aligned with the pore axis. Moreover, when the JCM is close to wall and rotating, it generates a high concentration zone for the reaction product near the wall (see Fig. 2-12c). Such a high concentration zone triggers the horizontal diffusiophoresis of the JCM toward the pore center. Because of the rotation and horizontal movements, the JCM tends to swim away from the pore wall and thus exhibit the self-alignment behavior shown in Fig. 2-12a and b.

2.3 Conclusions

The translational and rotational dynamics of JCMs in confined geometries driven by self-diffusiophoresis were studied using direct numerical simulations. The simulations revealed that JCMs can exhibit rich dynamic behavior under confined conditions. For the translocation of a single spherical JCM through a short cylindrical pore, while the JCM is slowed down by the pore on average, the speed of the JCM can exceed that in free solutions when the JCM approaches the pore exit. The overall slowdown of self-diffusiophoresis becomes more obvious when the pore size reduces, but its dependence on the pore size is much weaker than the transport of particles driven by external force or externally imposed concentration gradients. For the translocation of a pair of JCMs through a pore, when both of their catalytic surfaces are facing the bottom reservoir direction, the front JCM speedups but the back JCM slows down. For a circular JCM near a pore entrance and with its phoretic axis not aligned with the pore axis, the JCM can enter the pore and its phoretic axis becomes fully aligned with the pore axis if its initial inclination angle is small. Otherwise, the JCM either collides with the pore entrance or moves away into the reservoir. For a

JCM already inside a pore, self-diffusiophoresis can align the JCM's phoretic axis with the pore axis and drive it toward the pore center for the parameters considered here.

Analyses showed that these rich behaviors have both hydrodynamic and chemical origins. In particular, the modification of the chemical species concentrations surrounding a JCM by wall confinement and its neighboring JCMs, which is called "chemical effect", plays a key role in determining the translation and rotation of the JCMs. In ordinary particulate transport problems, chemical species in the solution and their transport have little or no impact on the particulate transport. In the self-diffusiophoresis of JCMs, however, chemical effects become important because the gradient of chemical species on their surface impacts the phoretic slip velocity on the surface. These effects, while received relatively little attention so far, are especially significant when the confinement is severe or when JCMs approach each other. Given these situations are increasingly encountered in the applications of JCMs, these chemical effects should be taken into account in the design and operation of JCMs in these applications.

Chapter 3. Bubble-Induced Collective Motion of JCMs[†]

In this Chapter, a new collective movement of Janus catalytic motors (JCMs) induced by bubble nucleation, growth, and collapse is studied. Experimentally, it has been observed that, when multiple JCMs are randomly crowded into a small region, bubbles start to form. When a single bubble is formed, it sets off the collective motion of its neighboring JCMs. During its growth, the bubble forces the participating JCMs to arrange around its base in a ring-like structure and draws them towards the center of the ring, until the bubble collapses. This process repeats until the fuel is exhausted. This process is very different from the previously reported collective/schooling behaviors and bubble propulsion of micromotors. Below the experimental setup involved in this collective movement of JCMs is briefly reviewed. Next a hypothesis for the newly discovered collective motion of JCMs is proposed. Finally, numerical simulations are performed to support the hypothesis and the validation of the hypothesis by controlled experiments are presented.

3.1 Brief Summary of Experimental Observations

A droplet of suspension loaded with JCMs was first deposited on clean Si and observed under the microscope. Another droplet of 10 – 20 % H₂O₂ solution was then added to the first droplet. For the high concentration (3×10^5 motors/ml) 5- μ m JCM suspended in the H₂O₂ solution, no bubbles are observed initially and the JCMs exhibit autonomous diffusiophoretic motion.^{117, 155}

[†] This chapter is adapted from the following paper (Ref. 101):

M. Manjare, F.C. Yang, R. Qiao, and Y.P. Zhao, “Marangoni Flow Induced Collective Motion of Catalytic Micromotors”, *J. Phys. Chem. C* **2015**, 119, 28361-2836732, 5580–5592.

Permission for using this paper here has been granted by the American Chemical Society. The experimental work reviewed briefly in this chapter was performed by Manjare, M. and Zhao, Y. P. of University of Georgia.

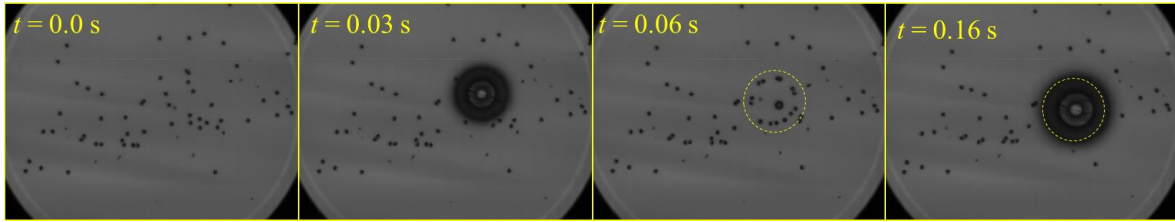


Figure 3-1. Snapshots of JCMs as they get densely populated in a small region and the subsequent bubble and ring formations. The small black dots are the 5 μm diameter JCMs.

However, after a short period of time ($\sim 30\text{--}60$ s), when JCMs drift randomly in the droplet, sometimes more than 2 or 3 JCMs come very close to each other. This type of “aggregation” is assumed to be random since it is observed to occur repeatedly at different locations in the liquid film. Once the JCMs come close to each other, a visible bubble starts to form in between JCMs. The bubble forces the adjacent JCMs to arrange at its base in a circle. As the bubble grows, it draws the JCMs in its vicinity towards the center of the circle. Once the bubble grows to a critical R_{\max} (typically between 50 – 75 μm), it collapses within a short period of time (<1 ms). However, the circular ring of JCMs is maintained and a new bubble starts to nucleate at the center of the ring and the above process repeats till the fuel is exhausted. The number of JCMs that can induce such a phenomenon is arbitrary. Figure 3-1 is a series of snapshots of a video taken during this process. It shows the process of initial swarming of JCMs, the bubble growth, and then the new bubble nucleation after previous one has collapsed. The new bubble also reaches approximately the same radius, R_{\max} , before it collapses and the cycle continues. It is important to note that the bubble is not attached to the surface of any JCMs and all the JCMs seem to collectively feed the bubble with O_2 from their catalytic conversion of H_2O_2 . As the time stamps indicate, the bubble growth-collapse cycles can be very fast. In one second, as many as 20 to 30 cycles of bubble growth and

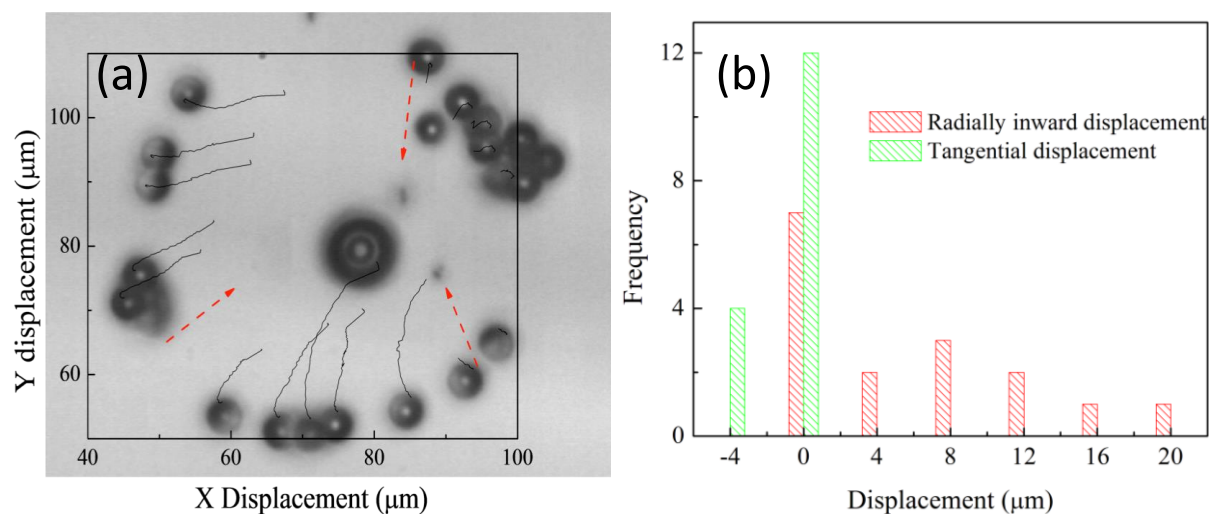


Figure 3-2. After the initial bubble collapse, the JCMs are locked in a ring. They all travel towards the center of the bubble as it grows. (a) The screenshot of an instant when new bubble starts to grow. The black lines highlight the trajectory of each motor. (b) The histogram of the decomposed displacements of JCMs in the radial and the tangential directions (for each JCM, the line pointing from the center of bubble to the center of the JCM is defined as the radial direction).

collapse can be observed and the JCM's speed during those cycles can reach a few hundred $\mu\text{m/s}$. However, slower cycles which take up to 1 s are also observed. The expected motion of JCMs due to diffusiophoresis, which is to travel in the opposite direction of the catalyst surface, is ceased and the micromotors are locked in these ring structures. Figure 3-2a shows the snapshot of a video sequence at a moment when the initial bubble of the cycle has just collapsed. Superimposed are the trajectories that each JCM motor follows after this image was taken. The red arrows denote the directions of the JCM motions. The JCMs all travel approximately toward a common point, which is the center of the bubble. This can be seen more clearly by examining the histograms of the displacement of each JCM. Specifically, for each JCM, it is defined the line pointing from the center of bubble to the center of the JCM as the radial direction. Then the JCM's displacement during one bubble growth-burst cycle is decomposed into a radial and a tangential component. As shown in Fig. 3-2b, the histogram of these two displacement components demonstrates that the net

displacement of JCMs is towards the bubble center. The bubble itself is not necessarily fixed to a location on Si substrate and is sometimes observed to move in the horizontal plane, with the ring moving with it. For example, the bubbles move laterally with a translation speed varying from 20 $\mu\text{m/s}$ to 60 $\mu\text{m/s}$ depending on the ring size.

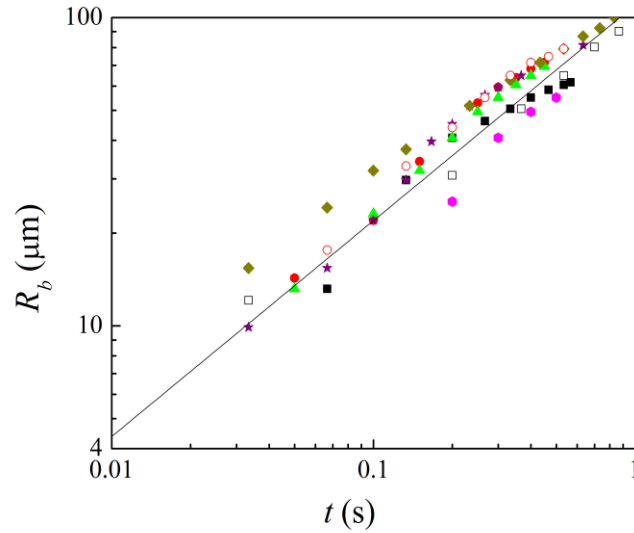


Figure 3-3. Log-log plot of the bubble growth radius R_b as a function of time t for different groups (hydrophobic and hydrophilic) of motors. Each different symbol represents a new bubble cycle. The red dotted line represents the power law fitting $R_b \sim t^n$ with $n = 0.7$.

The bubble growth in crowded JCM system followed a power law that deviates from the typical one observed in supersaturation-driven bubble growth. Figure 3-3 shows that the growth of bubble follows a power law,¹⁵⁶ i.e. $R_b \sim t^n$, with $n = 0.7 \pm 0.2$, for all cases observed. Such a growth law differs significantly from that for bubbles attached to single JCMs, where n is typically ~ 0.33 due to the nearly constant feed of oxygen into bubble.^{117, 155} The growth law observed here also differs from the growth of bubbles in homogeneous fluids supersaturated with oxygen, where $R_b \sim t^{0.5}$.

Several interesting bubble behaviors are observed in this bubble-induced collective motion of

JCMs. As established in previous reports^{117, 155}, no bubbles can be observed on individual 5 μm JCM beads. However, in this reported bubble-induced collective motion of JCMs, bubbles appeared when multiple JCMs came together. Finally, the collapse of the bubbles happens within 1 ms, which is too fast to be explained by dissolving. The underlying mechanisms of bubble formation, growth and collapse are discussed in details in Chapter 4.

3.2 Evaporation-Induced Collective Motion of JCMs

3.2.1 Hypothesis and Scale Analysis

In this section, the mechanism of the bubble-induced collective motion of JCMs is investigated through scale analysis and numerical simulations. Although the collective motion has been studied in detail in biological systems and many theoretical models exist on the prediction of their behaviors¹⁵⁷, the same approach could not be used for the phenomenon observed. The collective motion of the JCMs is synchronized with the bubble growth and collapse cycles. As noted before, the orientation of motors does not influence the motion. This implies that diffusiophoresis is not the dominant driving mechanism. The motion analysis of JCMs observed during bubble growth indicates that JCMs move toward the bubble's base with a speed up to a few hundreds of micrometers per second. Such a collective movement of the JCMs is too fast to be caused by the self-diffusiophoresis mechanism.¹⁵⁸⁻¹⁵⁹ The collective movement of JCM can also be due to the entrainment by bubble growth-induced flows, but calculations indicated that entrainment due to such flow ($\sim O(1 \mu\text{m}/\text{s})$) is too weak to explain the fast movement of JCMs observed experimentally.

Here, it is hypothesized that the fast movement of JCMs toward bubble's base is caused by the

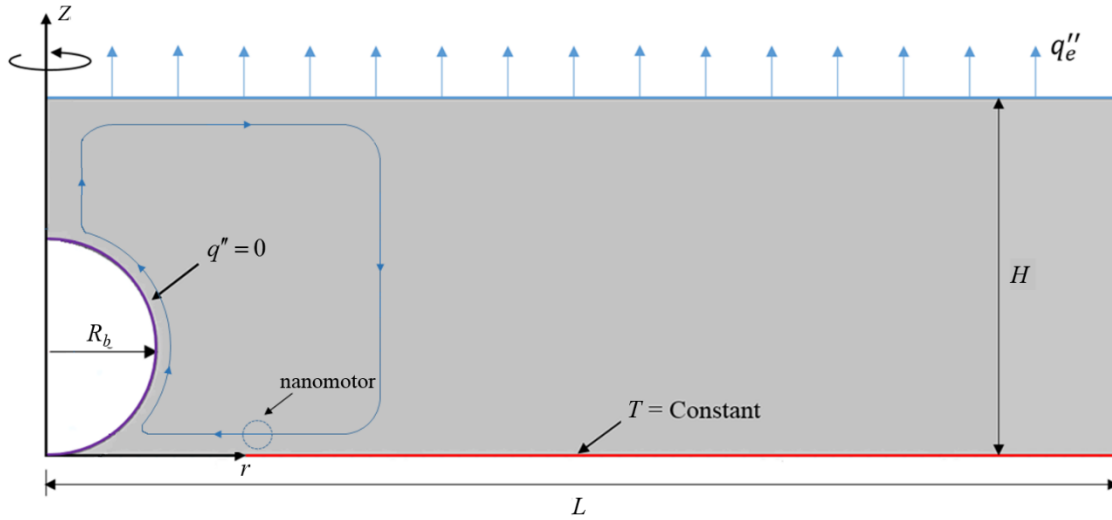


Figure 3-4. A schematic of the evaporation induced Marangoni flow. Cooling via evaporation at the top surface of the liquid film creates a temperature gradient along bubble surface. Such a temperature gradient generates a Marangoni stress on bubble surface, which in turn induces a Marangoni flow in the vicinity of the bubble.

evaporation-induced Marangoni flow near the bubble since the observing liquid drop is thin ($\sim 100 \mu\text{m}$) on Si substrates. As shown in Fig. 3-4, the evaporation of water on the top surface of the liquid film induces a heat flux, q''_e , which causes the liquid at the bottom of the bubble to be warmer than that at the top of the bubble. Since the surface tension of water decreases as temperature increases, the surface tension of water is higher at top of the bubble than at the bottom of the bubble. This variation of the surface tension along the bubble surface drives a Marangoni flow¹⁶⁰, which can entrain JCMs near the substrate toward the bubble's base.

To estimate whether the Marangoni flow postulated above can entrain JCMs with the speed observed experimentally, a scale analysis is performed next. Previous studies indicate that the evaporation rate at the surface of the droplet and thin liquid films is governed by the diffusion of water vapor from the liquid-air interface toward the surrounding atmosphere, and the air at liquid film surface is saturated by water¹⁶¹. Therefore, for the thin liquid film containing the JCMs, the

average cooling rate q_e^{C} on its top surface due to evaporation is given by

$$q_e'' = h_w \dot{m}_{eva}; \text{ and } \dot{m}_{eva} = D \frac{S}{\pi R_f^2} C_w^* (1 - \varphi), \quad (3-1)$$

where R_f is the radius of the thin liquid film, h_w is the latent heat of water, $S = 4R_f$ is the shape factor for mass diffusion from a thin film of radius R_f toward a semi-infinite domain¹⁶², D here is the diffusion coefficient of water vapor in the air, C_w^* is the saturation concentration of water in air, and φ is the relative humidity of surrounding atmosphere. In the present experiments, the water film on the substrate has a radius of ~ 5 mm. Hence, the cooling flux is calculated as

$q_e^{\text{C}} = 200 \text{ W} / \text{m}^2$ if the relative humidity of the surrounding environment is 50% and the

thermophysical properties of water at room-temperature are used ($k = 0.563 \text{ W}/(\text{m}\cdot\text{K})$, $D = 2.82 \times 10^{-5} \text{ m}^2/\text{s}$, $h_w = 2260 \text{ kJ}/\text{kg}$). This cooling heat flux generates a temperature gradient along bubble surface, which in turn leads to a surface tension gradient (i.e. Marangoni stress) and flow along the bubble surface. The strength of the induced flow can be estimated by balancing the Marangoni

stress with the viscous stress, i.e., $\frac{d\sigma}{dT} \nabla_s T \sim \mu \nabla_n u_\tau$, where u_τ is the fluid velocity tangential to the

bubble surface, σ is the surface tension, μ is the viscosity of water, and ∇_s (∇_n) is the gradient along the tangential (normal) direction of the bubble surface. Using the bubble radius as the characteristic length for the induced flow and assuming that the temperature gradient along the

bubble surface $\nabla_s T$ is similar to the average temperature gradient of fluid temperature across the

liquid film $\frac{\partial \bar{T}}{\partial y}$, the fluid velocity at bubble surface is $U \sim \frac{\beta}{\mu} \frac{\partial \bar{T}}{\partial y} R_b$, where R_b is the bubble radius.

Since the heat transfer in the liquid film is dominated by conduction, $\frac{\partial \bar{T}}{\partial y} \sim \frac{q_e''}{k}$, where k is the

thermal conductivity of water. Therefore, the velocity scales as $U \sim \frac{\beta}{\mu} \frac{q_e''}{k} R_b$. Hence, for a $10 \mu\text{m}$ -

radius bubble in such a water film, the velocity of the Marangoni flow is $\sim 100\mu\text{m}/\text{s}$ at the bubble surface if the relative humidity of the environment is 50% and the thermophysical properties of water at room-temperature are used ($\mu=0.001\text{ Pa}\cdot\text{s}$ and $\beta=d\sigma/dT=-1.514\times 10^{-4}\text{N}/(\text{m}\cdot\text{K})$). The entrainment of JCMs by such a strong Marangoni flow can potentially lead to the fast transport of JCMs observed in experiments.

3.2.2 Numerical Simulation of Marangoni Flow in the Vicinity of a Bubble

To quantify the strength of the evaporation-induced Marangoni flow, such flow near a single bubble under the axisymmetric condition is simulated as sketched in Fig. 3-5. The bubble is treated as spherical, attached to the substrate with an approximately zero contact angle. Since the Marangoni flow mainly exists in the vicinity of the bubble, the length of the simulation domain, L , is set to be $300\mu\text{m}$ (using a larger length only changes the result slightly). The thickness of the liquid film, H , is set as $100\mu\text{m}$, similar to that in the experiments. Since the dimension of simulation domain is much smaller than the liquid film, the top surface of the simulation domain can be treated as flat.¹⁶³ The simulation system features a single bubble attached to a substrate covered by a thin liquid film. To simulate the fluid flow and heat transfer near the bubble, the temperature and flow fields are assumed to be at quasi-steady state during the growth of the bubble. This is a good approximation because both the Peclet and Reynolds numbers are small.¹⁶⁴ Specifically, in this case, using the bubble radius as the characteristic length scale ($R_b \sim O(10\mu\text{m})$), and the JCM velocity as the characteristic velocity scale ($U \sim O(100\mu\text{m}/\text{s})$), the Peclet number $Pe \sim O(10^{-2})$ and the Reynolds number $Re \sim O(10^{-3})$ are obtained. Under the quasi-steady conditions, the temperature field observes the Laplace equation, and the flow field observes the Stokes equations. In the heat transfer model, zero heat flux is applied on the bubble surface. The

temperature of the substrate is set to $T_s = 293.15$ K. Generally, the cooling flux on the surface of a finite-sized liquid film/droplet is non-uniform, which plays a key role in generating the Marangoni flow that spans the entire liquid film/droplet.¹⁶⁵⁻¹⁶⁷ However, in this study, this non-uniformity is neglected and the uniform cooling flux of $q_e^{\text{C}} = 200$ W/m² computed above is implemented. Such a treatment is reasonable here for two reasons. First, because the water film has a much larger radius compared to the bubble and most bubbles are positioned away from the edge of the film, the cooling flux on the surface of the water film near these bubbles is rather uniform. Second, the non-uniformness of the cooling on the surface of the liquid film only weakly affects the Marangoni flow *near the bubble*, the focus of the present study. To capture the flow induced by the Marangoni stress and growth of the bubble, the bubble surface moves with a speed measured from experiments, and an extra Marangoni stress due to the temperature gradient is added to both bubble surface and the liquid film surface. The substrate is set as a no-slip and impermeable wall. The detailed mathematical models and implementation for the fluid and thermal transport problem is described below.

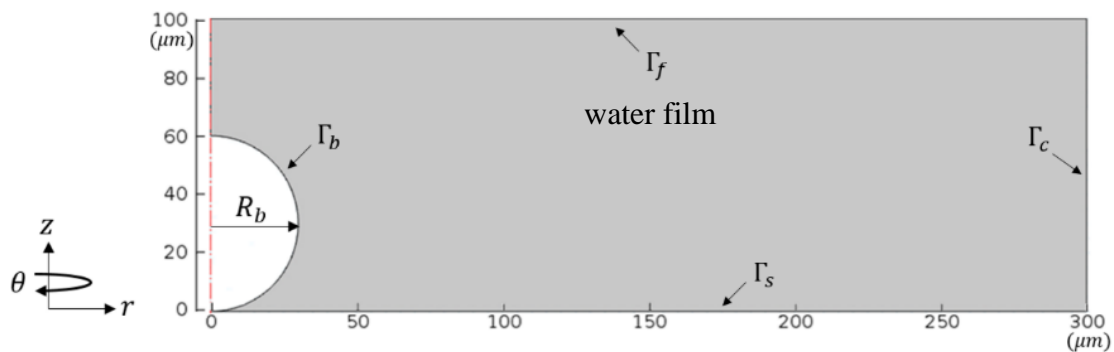


Figure 3-5. System used to investigate the evaporation-induced Marangoni flows: a spherical bubble is anchored on a substrate, which is covered by a thin liquid film.

Figure 3-5 shows a detailed schematic of the simulation system, with each boundary labeled. Since the gas inside has a low viscosity and thermal conductivity comparing to the liquid, the flow and heat transfer inside the bubble is neglected. The thermal transport in the system is governed by¹⁶⁴⁻¹⁶⁵

$$\nabla^2 T = 0, \quad (3-2)$$

with boundary condition given by

$$-\mathbf{n} \cdot (-k\nabla T)|_{\Gamma_b} = 0 \quad (\text{adiabatic bubble wall}), \quad (3-3)$$

$$T|_{\Gamma_s} = 293.15\text{K} \quad (\text{fixed substrate temperature}), \quad (3-4)$$

$$-\mathbf{n} \cdot (-k\nabla T)|_{\Gamma_c} = 0 \quad (\text{adiabatic wall at domain boundary } \Gamma_c), \quad (3-5)$$

$$-\mathbf{n} \cdot (-k\nabla T)|_{\Gamma_f} = q_e'' \quad (\text{uniform cooling flux on film surface}), \quad (3-6)$$

where T is the temperature, \mathbf{n} is the surface normal vector, and k is the thermal conductivity of the liquid film (taken as water). q_e'' is the cooling flux due to evaporation and is taken to be 200 W/m^2 as explained in the main text. The fluid flow is governed by the Stokes equations

$$\nabla \cdot \mathbf{u} = 0, \quad (3-7)$$

$$\mu \nabla^2 \mathbf{u} = \nabla p, \quad (3-8)$$

where \mathbf{u} and p are the velocity and pressure, respectively. μ is the viscosity of the water (taken as $1 \text{ mPa}\cdot\text{s}$). The boundary conditions for equations (6) and (7) are given by

$$\mathbf{u}|_{\Gamma_s} = 0 \quad (\text{no-slip on substrate}), \quad (3-9)$$

$$\mu(\nabla \mathbf{u} + (\nabla \mathbf{u})^T) \cdot \mathbf{n}|_{\Gamma_c} = 0 \quad (\text{stress free domain boundary } \Gamma_c), \quad (3-10)$$

$$\mu \frac{\partial \mathbf{u}}{\partial \mathbf{n}}|_{\Gamma_f} = \beta \frac{\partial T}{\partial s}|_{\Gamma_f} \quad (\text{Marangoni stress on film's top surface}), \quad (3-11)$$

where s is the tangential direction of a surface. The boundary conditions on bubble surface are more complicated and are determined as follows. In addition to the Marangoni stress on the top surface of the liquid film (Equ. 3-11), the fluid flow in the system is driven by two additional sources: the Marangoni stress on the bubble surface and the growth of the bubble, which displaces surrounding fluids. The former induces a velocity tangential to the bubble surface, \mathbf{u}_1^b . The latter leads to a generally outward velocity \mathbf{u}_2^b on the bubble surface. Hence the boundary conditions on the bubble surface can be given by

$$\mathbf{u}|_{\Gamma_b} = \mathbf{u}_1^b + \mathbf{u}_2^b. \quad (3-12)$$

The velocity field corresponding to \mathbf{u}_1^b satisfies

$$\mu \frac{\partial \mathbf{u}_1^b}{\partial n} |_{\Gamma_b} = \beta \frac{\partial T}{\partial s} |_{\Gamma_b}. \quad (3-13)$$

Experimentally, it was observed that the bubble typically grows to $\sim 60 \mu\text{m}$ in $\sim 0.6\text{s}$ with its bottom barely lifting from the substrate. In line with these observations, velocity \mathbf{u}_2^b was constructed to satisfy two conditions simultaneously (1) the bubble radius grows at a speed of $100 \mu\text{m/s}$ and (2) the bubble remains spherical and its south pole remains in touch with the substrate.

Equations 3-(2-13) form a complete description of the temperature and velocity field within the system. At any time instant t , the bubble radius was determined using the constant growth speed assumed above. The quasi-static temperature field was then computed by solving Equ. 3-(2-6). Next, the quasi-static velocity field was obtained by superimposing the velocity fields of two auxiliary problems, i.e., $\mathbf{u} = \mathbf{u}_1 + \mathbf{u}_2$. In the first auxiliary problem, the bubble surface has no outward velocity (i.e., bubble does not grow), and the bubble surface and the liquid film surface are subjected to the Marangoni stress. In the second auxiliary problem, the bubble surface moves

according to the \mathbf{u}_2^b constructed above, while the bubble surface and the liquid film surface experience no tangential stress. The velocity field \mathbf{u}_1 is governed by

$$\nabla \cdot \mathbf{u}_1 = 0 \quad (3-14)$$

$$\mu \nabla^2 \mathbf{u}_1 = \nabla p_1 \quad (3-15)$$

$$\mathbf{u}_1|_{\Gamma_s} = 0 \quad (3-16)$$

$$\mu(\nabla \mathbf{u}_1 + (\nabla \mathbf{u}_1)^T) \cdot \mathbf{n}|_{\Gamma_c} = 0 \quad (3-17)$$

$$\mu \frac{\partial \mathbf{u}_1}{\partial \mathbf{n}}|_{\Gamma_f} = \beta \frac{\partial T}{\partial s}|_{\Gamma_f} \quad (3-18)$$

$$\mathbf{u}_1 \cdot \mathbf{n}|_{\Gamma_b} = 0 \quad (3-19)$$

$$\mu \frac{\partial \mathbf{u}_1}{\partial \mathbf{n}}|_{\Gamma_b} = \beta \frac{\partial T}{\partial s}|_{\Gamma_b} \quad (3-20)$$

The velocity field \mathbf{u}_2 is governed by

$$\nabla \cdot \mathbf{u}_2 = 0 \quad (3-21)$$

$$\mu \nabla^2 \mathbf{u}_2 = \nabla p_2 \quad (3-22)$$

$$\mathbf{u}_2|_{\Gamma_s} = 0 \quad (3-23)$$

$$\mu(\nabla \mathbf{u}_2 + (\nabla \mathbf{u}_2)^T) \cdot \mathbf{n}|_{\Gamma_c} = 0 \quad (3-24)$$

$$\mu \frac{\partial \mathbf{u}_2}{\partial \mathbf{n}}|_{\Gamma_f} = 0 \quad (3-25)$$

$$\mathbf{u}_2|_{\Gamma_b} = \mathbf{u}_2^b \quad (3-26)$$

It is straightforward to show that $\mathbf{u} = \mathbf{u}_1 + \mathbf{u}_2$ satisfies Equations 3-(7-13).

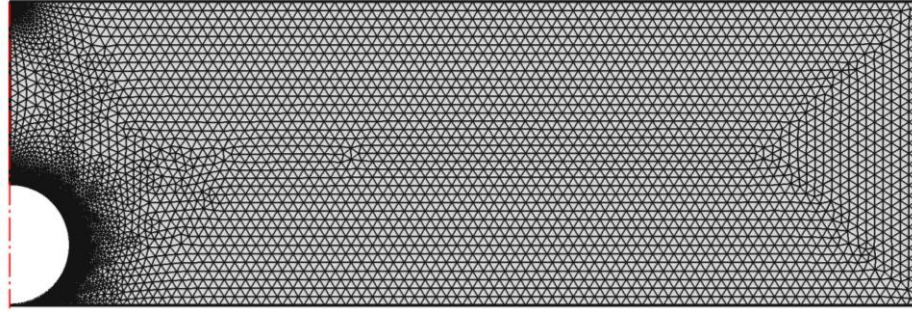


Figure 3-6. The mesh used in simulations in which the bubble radius is $20\mu\text{m}$.

The models described above were solved using a finite element package COMSOL. The computational domain is discretized into a triangular mesh. A typical mesh used in simulations, which consisted of 22645 free triangle elements, is shown in Fig. 3-6. The temperature and velocity field were solved using COMSOL's CFD and heat transfer modules. The simulations corresponding to time instants were performed at which the bubble radius was 10, 20 and $30\mu\text{m}$.

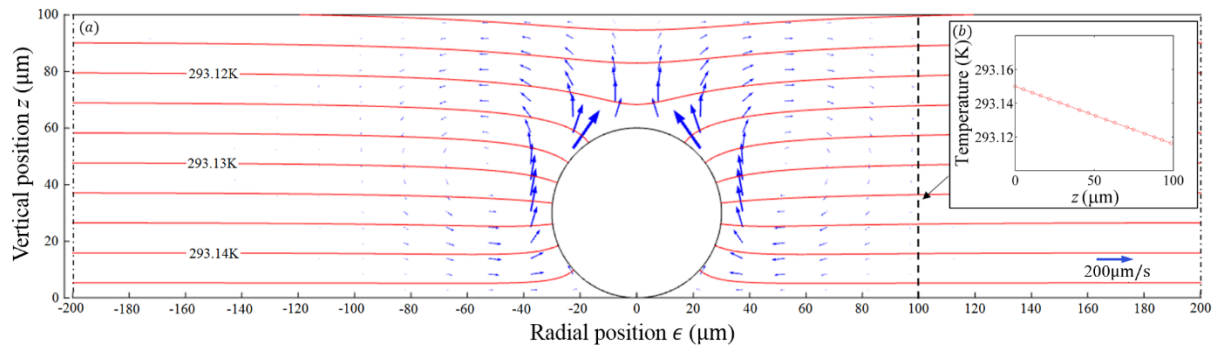


Figure 3-7. Marangoni flow in the vicinity of the bubble within a cooling liquid film. (a) The velocity field (blue vectors) and temperature contours (red lines) are calculated for a bubble radius of $30\mu\text{m}$. The thickness of the liquid film is $100\mu\text{m}$, and a uniform cooling flux of 200W/m^2 is applied on the liquid film surface. (b) Temperature profile across the liquid film at a radial position of $100\mu\text{m}$.

Based on above setup, the thermal and fluid transport inside water were solved (i.e., outside of the bubble, see the shaded region in Fig. 3-5) and obtained the velocity and temperature fields near a bubble attached to the substrate during bubble growth. Figure 3-7 shows the velocity and

temperature fields at the moment when bubble radius R_b is $30\ \mu\text{m}$. It is observed that the cooling at the top surface of the liquid film induces a temperature gradient along bubble surface. This temperature gradient generates a strong Marangoni flow in the vicinity of the bubble. The magnitude of the Marangoni flow is on the order of $O(100\ \mu\text{m/s})$, which is consistent with the observations above. Figure 3-7 shows that the Marangoni flow at positions near the substrate is directed toward the bubble base, which can potentially entrain JCMs toward the bubble. To more quantitatively examine the entrainment of JCMs by the Marangoni flow, the radial velocity of the Marangoni flow at a distance of $5\ \mu\text{m}$ above the substrate is plotted (see Fig. 3-8), where the JCMs

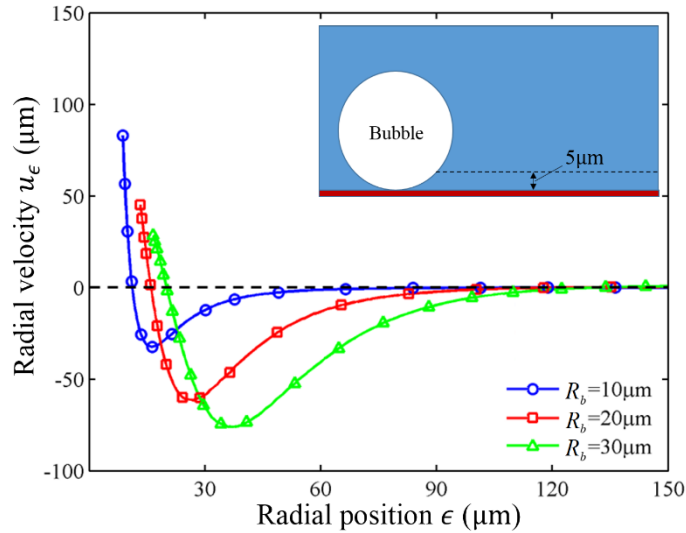


Figure 3-8. The radial velocity of the Marangoni flow in the vicinity of a bubble. Flow velocities are evaluated at a position of $5\ \mu\text{m}$ above the substrate (dashed line in the inset). The thickness of the liquid film is $100\ \mu\text{m}$, and a uniform cooling flux of $200\ \text{W/m}^2$ is applied to the film surface. The negative velocity corresponds to the flow toward the bubble base.

are observed in the experiments. A positive/negative velocity means the flow is directed outward/toward bubble base. Figure 3-8 shows that, except in the immediate vicinity of bubble surface, the fluid moves toward bubble base. For example, for a bubble with a radius of $10\ \mu\text{m}$, fluids movement toward bubble base with a speed $\sim O(10\ \mu\text{m/s})$ exists in the region $\sim 2R_b$ from

the bubble surface. As the bubble grows larger, the flow that can entrain JCMs enhances; but its speed remains $\sim O(10-100 \mu\text{m/s})$, and the region within which JCMs are strongly entrained remains $\sim 2R_b$. Note that there exists a region in the immediate vicinity of bubble surface, where the radial velocity is positive. This positive velocity corresponds to the deflection of the fluid flow by the bubble surface (Fig. 3-4). From Fig. 3-7 and 3-8, it is found that the direction and speed $\sim O(10-100 \mu\text{m/s})$ of the evaporation-induced Marangoni flow predicted in the simulation help explain the fast, collective movement of JCMs toward the bubble base.

As the Marangoni effects are induced by the evaporation of water at the top surface of the liquid film, whose intensity is controlled by the relative humidity of the surrounding air (see Equ. 3-1), it is expected that the collective motion of JCMs to be suppressed if the relative humidity of the air is increased. Preliminary experiments were performed to confirm this claim by placing the entire liquid film loaded with micromotors inside a glass enclosure sealed by a glass slide. The bottom portion of the glass enclosure was filled with warm water to increase the humidity and prevent liquid evaporation. Under this condition, the collective bubbling effect disappeared, which supports the hypothesis that the Marangoni effects are responsible for the collective motion of JCMs observed in Fig. 3-1. Note that, if the motors were located at the air-liquid interface, the collective motion could have been explained by capillary forces.¹⁶⁸⁻¹⁶⁹

3.3 Conclusions

A new collective motion behavior of JCMs accompanied by periodic bubbling is analyzed in this Chapter. Experimentally, it was found that individual 5- μm JCMs submerged in solution cannot form bubble independently. However, at high JCM density, JCMs aggregate locally and collectively enable the nucleation and growth of bubbles. As the bubble grows, the JCMs exhibit

a collective, synchronized motion. This motion is fast and its direction is towards the center of the bubble, regardless the orientation of catalytic surface on the JCMs. It is proposed that the motion of JCMs towards the bubble center is caused by the Marangoni flow effects. Scale analysis showed that the strength of this Marangoni flow is of the same order of magnitude as that observed experimentally. Furthermore, to quantitatively examine this hypothesis, a mathematical model is established and implemented into COMSOL. Simulations show that the Marangoni effect can produce similar speeds observed in the experiments. The collective motion should also be observed for other catalytic particles. This is because the formation of the bubble and consequently the Marangoni flow near the bubble should exist as long as gas molecules are released from the surface of catalytic particles, regardless whether the particle is half- or fully-coated with catalysts. This result could be expected to garner interest for collective task management with fewer size restrictions as far as bubble nucleation is concerned.

Chapter 4. Bubble Behaviors in JCM Systems[‡]

As mentioned in Chapter 1 and shown in Chapter 3, the underlying mechanisms behind the bubble behaviors (formation, growth, and collapse) observed in active particle system (particularly, JCM system) are still not well understood. Specifically, for bubble formation, what is the criterion of bubble formation in JCM systems? Why cannot a small JCM nucleate bubble independently? Why bubbles form as multiple small JCMs come close to each other? For bubble growth, why does the scaling law of the bubble growth in JCM systems deviate from the classical bubble growth laws? For bubble collapse, why does bubble disappear in extremely short time scale in some experiments?

Most previous studies on the role of bubbles and their behaviors in active particle system relies on experimental observation, while theoretical analysis and numerical simulations of these problems are largely absent. Hence, in this Chapter, both theoretical analysis and numerical simulations are utilized to investigate and answer these above questions regarding the formation, growth, and collapse of bubbles in an active particle system.

4.1 Bubble Formation in JCM Systems

Before trying to understand the formation of oxygen bubbles in JCM systems, the formation (i.e., nucleation) of a bubble in homogenous liquid solutions is first briefly reviewed. According

[‡] This chapter is adapted from the following paper (Ref. 170):

F.C. Yang, M. Manjare, Y.P. Zhao and R. Qiao, “On the peculiar bubble formation, growth, and collapse behaviors in catalytic micro-motor systems”, *Microfluid. Nanofluid.* **2017**, 21, 6

Permission for using this paper in this dissertation has been granted by Springer. The experimental work reviewed briefly in this chapter was performed by Manjare, M. and Zhao, Y. P.

to the classical nucleation theory, bubble formation is an activation process, i.e., for a bubble to grow to macro-scale, it must reach a critical radius R_c by overcoming a nucleation energy barrier.¹²⁵ Usually, such a process is facilitated by high levels of supersaturation.¹⁷¹⁻¹⁷² Here, starting by considering a spherical oxygen bubble of critical size submerged in static hydrogen peroxide solution. If this bubble is in mechanical equilibrium with the solution (neither growing nor shrinking), the pressure difference between inside and outside of the bubble follows the Young-Laplace equation¹⁷³, i.e.,

$$p_b - p_\infty = \frac{2\sigma}{R_c} \quad (4-1)$$

where R_c is the critical radius of the bubble embryo (i.e., in equilibrium with solution), σ is the surface tension of the solution, p_b is the pressure within the bubble, and p_∞ is the pressure in bulk liquids. The energy barrier¹⁷⁴ for this critical bubble to form is

$$\Delta G_{homo} = \frac{4\pi\sigma R_c^2}{3} \quad (4-2)$$

Assuming the bubble only consists of oxygen molecules, the oxygen concentration in the thin liquid layer in contact with the bubble is given by Henry's law¹²²

$$c_{g,l} = \kappa_H \left(p_\infty + \frac{2\sigma}{R_c} \right) \quad (4-3)$$

where κ_H is the Henry's constant of oxygen at the room temperature. If the oxygen concentration in bulk liquids is smaller than $c_{g,l}$, the diffusion of oxygen molecules away from the bubble will drive its shrinkage. Therefore, $c_{g,l}$ is the critical oxygen concentration in the bulk liquid for the formation of a critical bubble with a radius of R_c . In another word, to form a critical bubble embryo of radius R_c , the concentration in its surrounding solution must fulfil Equ. 4-3 and an energy barrier of ΔG_{homo} must be overcome. It follows that, in bulk solutions, the critical radius of bubble

embryo and the energy barrier, when bubble nucleation occurs, increases (decreases) as the oxygen concentration in the solution decreases (increases).

Equations 4-(1-3) are for the homogeneous nucleation of bubbles in a uniform concentration field. In JCM systems, bubbles are usually formed by heterogeneous nucleation on solid surfaces. Bubble formation on solid surfaces is facilitated by the existence of gas-filled cavities on the surfaces. However, the typical size of JCMs used in the experiments is small and the coated surface is relatively smooth. Hence, the effect of pre-existing gas cavities on the formation of bubbles is neglected. The physics of heterogeneous nucleation of bubbles on a smooth surface exposed to a uniform concentration field is similar to that of the homogeneous nucleation except that the energy barrier is modified. The energy barrier for the heterogeneous nucleation of a bubble on a spherical solid object, ΔG_{hetero} , is given by¹⁷⁵

$$\Delta G_{hetero} = \Delta G_{homo} \cdot f(m, x) \quad (4-4)$$

where $f(m, x)$ is the shape factor given by¹⁷⁶

$$f(m, x) = \frac{1}{2} \left\{ 1 + \left(\frac{1-mx}{g} \right)^3 + x^3 \left[2 - 3 \left(\frac{x-m}{g} \right) + \left(\frac{x-m}{g} \right)^3 \right] + 3mx^2 \left(\frac{x-m}{g} - 1 \right) \right\}, \quad (4-5)$$

$$\begin{cases} g = (1 + x^2 - 2mx)^{\frac{1}{2}} \\ m = -\cos\theta \\ x = R_p/R_c \end{cases}$$

where θ is the contact angle of the liquid solution on the solid surface and R_p is the radius of the solid sphere. Note f has a maximal value of 1, which means the energy barrier of heterogeneous nucleation is usually lower than homogeneous nucleation for the same bubble embryo. This is because, in heterogeneous nucleation, the wetted surface truncates part of the bubble embryo and thus reduces the energy barrier for the formation of gas-liquid interface. However, if the wetting

is excellent (i.e., the contact angle of water on the JCM's surface is small), the truncation of bubble embryo by the solid surface will be small. In turn, the reduction of the energy barrier for nucleation is not significant. In JCM systems, for typical JCMs ($1\mu\text{m} < R_p < 100\mu\text{m}$) with a small contact angle (e.g., $\theta < 30^\circ$), f is larger than 0.985, which only has minor effect on the energy barrier. Hence, the nucleation of bubble on JCM surfaces depends rather weakly on the contact angle and JCM size. Hereafter, without a loss of generality, the contact angle is taken to be zero and thus the shape factor is 1.

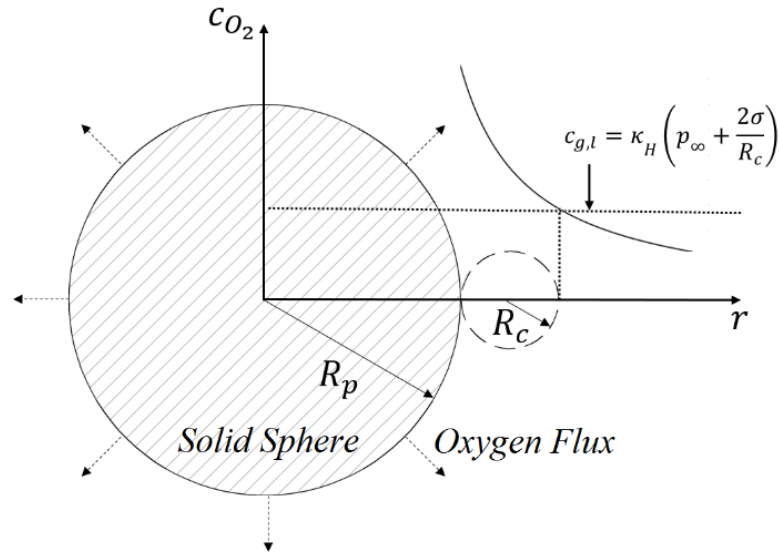


Figure 4-1. Formation of a critical bubble embryo on a solid sphere whose surface produces oxygen by catalytic reactions.

Using Equ. 4-(1-3) to understand the formation of bubbles in JCM systems, however, faces another issue. Specifically, since oxygen molecules are generated on the catalytic surface of a JCM, the oxygen concentration field near JCM is not uniform and decreases as one moves away from the surface (see Fig. 4-1). Inspired by previous studies of bubble nucleation in non-uniform temperature fields during boiling¹⁷⁷⁻¹⁷⁸, it is suggested the following criterion for the formation of a critical bubble embryo in a non-uniform concentration field. As shown in Fig. 4-1, to form a

critical bubble embryo with a radius of R_c , the oxygen concentration in the liquid solution in contact with *any* point on the bubble surface must be greater than that given by Equ. 4-3, i.e.,

$$c|_{\Gamma} \geq c_{g,l}, \quad (4-6)$$

where Γ denotes the surface of the bubble embryo. This criterion ensures that a critical bubble embryo does not shrink due to the diffusion of oxygen away from its surface. Using Equ. 4-6 requires the oxygen concentration field near the solid sphere. In principle, this concentration field depends both on the size and growth history of the bubble embryo, which will greatly complicate the analysis of bubble nucleation. Here, in spirit of the prior works on the bubble nucleation in non-uniform temperature fields ¹⁷⁷⁻¹⁷⁸, these effects are neglected and it is assumed that the concentration field near the solid sphere is not perturbed by the presence of a critical embryo, i.e., the critical embryo is a “phantom” bubble as far as the oxygen transport near the solid sphere surface is concerned. This simplification is partially consistent with the fact that the amount of oxygen for forming a critical bubble is small, and as it will see later, analysis based on this simplification produces results consistent with experimental observations.

Before using Equ. 4-6 to study the bubble formation on JCMs, first a related but simpler problem is considered, i.e., bubble formation on a sphere fully coated with Pt and immersed in a stagnant solution. For this problem, one can predict analytically the minimal sphere size for the formation of a bubble on it. If an oxygen flux of \dot{q} is imposed on the sphere’s surface and the bulk solution has an oxygen concentration of c_{∞} , then solving the diffusion equation ¹⁶² for oxygen transport leads to

$$c(r) = \frac{\dot{q}R_p^2}{Dr} + c_{\infty}, \quad (4-7)$$

where D is the diffusion coefficient of oxygen in the solution, r is the radial distance from the

sphere's center. For the critical bubble embryo shown in Fig. 4-1, using the criterion given by Equ. 4-6, it is obtained that

$$\frac{\dot{q}R_p^2}{D\kappa_H(R_p+2R_c)} - \beta p_\infty = \frac{2\sigma}{R_c}, \quad (4-8)$$

where $\beta = 1 - y_{g,\infty}$ and $y_{g,\infty}$ is the molar fraction of oxygen in the atmosphere surrounding the liquid solution. For simplicity, assuming that $y_{g,\infty}=1$, it can be simplified to

$$R_c = \frac{R_p}{(R_p/\alpha)^2 - 2}, \quad \alpha^2 = \frac{2\sigma D\kappa_H}{\dot{q}} \quad (4-9)$$

Equation 4-9 shows that the radius of critical bubble embryo increases as the sphere radius R_p and the O_2 flux \dot{q} on the sphere surface decreases. Since the energy barrier for the formation of a critical embryo decreases with the embryo radius (see Equ. 4-2), it follows that formation of critical bubble embryo becomes more difficult as the sphere becomes smaller or as the O_2 flux on the sphere surface decreases, which is consistent with experimental observations.¹⁰¹ In addition, when the sphere radius R_p decreases toward $\sqrt{2}\alpha$, the radius of critical bubble embryo diverges, i.e., no bubble can be nucleated on sphere with $R_p < \sqrt{2}\alpha$. Physically, when the size of sphere is small, it is hard to maintain a high supersaturation of oxygen molecules near the sphere's surface due to the efficient dissipation of the oxygen generated on its surface toward bulk solution, thus making bubble nucleation difficult.

For the JCMs used in Chapter 3, the O_2 flux on their catalytic surface was measured to be $\dot{q}=1.08 \times 10^{-3} \text{ mol}/(\text{m}^2 \cdot \text{s})$, when the H_2O_2 concentration was 10%. Using the thermophysical properties of oxygen and water at room temperature ($\sigma=0.072 \text{ N} \cdot \text{m}$, $\kappa_H=1.3 \times 10^{-3} \text{ mol}/(\text{L} \cdot \text{atm})$, $D=2 \times 10^{-9} \text{ m}^2/\text{s}$), the radius of the critical bubble embryo is calculated using Equ. 4-9, and results

are shown in Fig. 4-2. It is found that the size of the critical bubble embryo diverges as the sphere's radius R_p reduces toward $2.8\mu\text{m}$, suggesting that no bubble can be formed on such small particles.

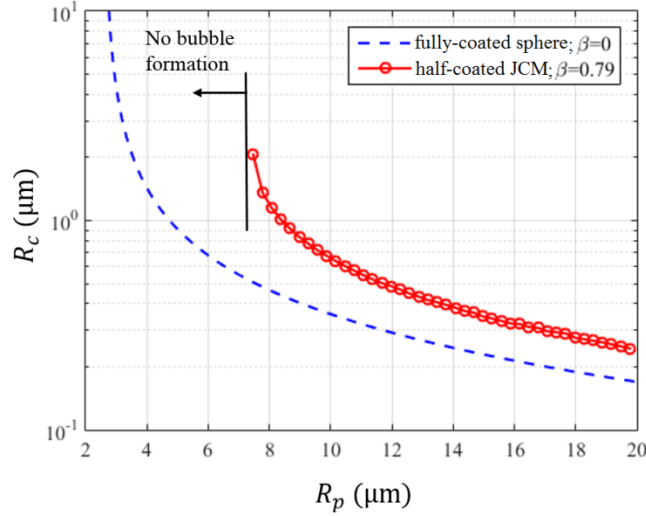


Figure 4-2. Radius of critical bubble embryo attached to uniformly coated spheres and half-coated JCMs immersed in bulk solutions.

Two restrictive assumptions were made in the above analysis, i.e., the environment surrounding the liquid solution was assumed to contain oxygen only and there was an O_2 flux on the entire surface of the JCM. To remove these restrictions, the O_2 concentration field near spherical JCMs with only half of their surface coated by platinum is computed.

Figure 4-3 shows a schematic of the simulation system, with each boundary labeled. The system consists of a JCM placing in static, free solution. Since bubble embryo tends to form in the region with the highest oxygen concentration, this study focuses on the concentration of oxygen along the pole of the catalytic surface (i.e., the dotted dash line in Fig. 4-2). Because of the small Peclet number, the O_2 concentration field is governed by the Laplace equation

$$\nabla^2 c = 0 \quad (4-10)$$

with boundary conditions given by

$$c = c_{g,l}^{\infty} \quad \text{on } \Gamma_1 \quad (4-11)$$

$$-D\nabla c(\mathbf{x}, t) \cdot \mathbf{n} = 0 \quad \text{on } \Gamma_2 \quad (4-12)$$

$$-D\nabla c(\mathbf{x}, t) \cdot \mathbf{n} = \dot{q} \quad \text{on } \Gamma_3 \quad (4-13)$$

where c here is the O_2 concentration, \mathbf{n} is the surface normal vector, and $c_{g,l}^{\infty}$ is the oxygen concentration of bulk liquid solution, which is determined by the oxygen partial pressure of the environment in which the bulk solution is placed. The O_2 flux on the catalytic surface of a JCM is the same as above. $y_{g,\infty}$ is taken as 0.79 because the solution containing JCMs were exposed to air in the experiments.

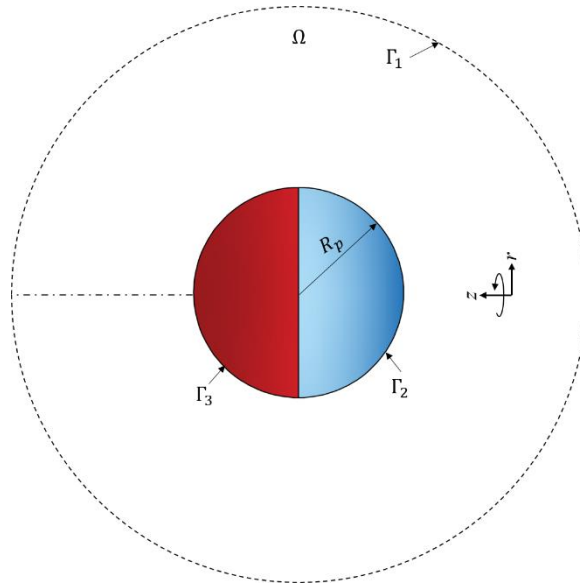


Figure 4-3. Setup used to simulate the O_2 concentration field generated by an isolated JCM. A JCM is placed in a liquid solution (denoted by Ω). Γ_1 denotes the boundary of the spherical liquid solution. Γ_2 and Γ_3 denote the neutral surface and catalytic surface of JCM, respectively. The domain of the liquid solution has a radius of 100 times of the JCM radius.

The system described above were solved using a finite element package COMSOL.¹⁴⁴ Taking advantage of the symmetry, the problem can be simplified to a 2D axisymmetric problem. The computational domain is discretized into triangular meshes. A typical mesh used in the simulations

(see Fig. 4-4) consisted of 15130 free triangle elements. The concentration field was solved using COMSOL's chemical transport modules and stationary solver.

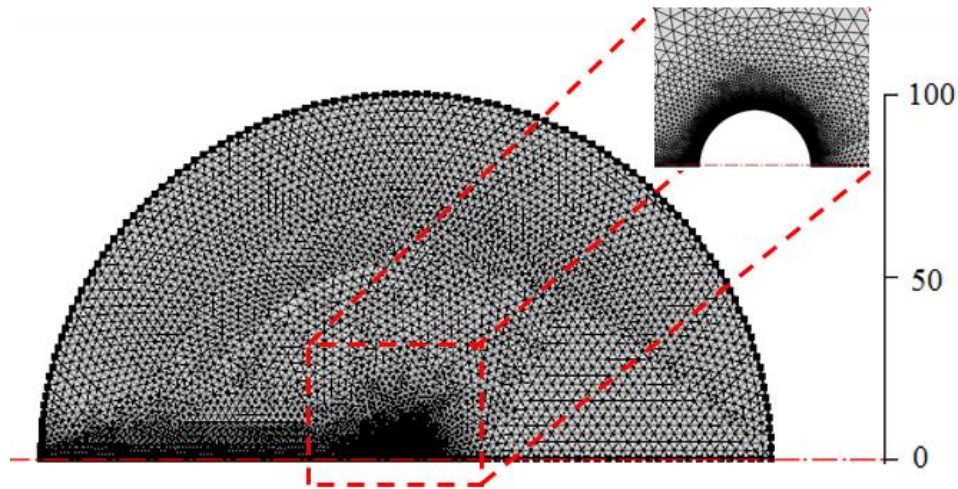


Figure 4-4. The mesh used for simulation of the system shown in Fig. 4-2.

The oxygen concentration profile obtained from above simulation is then used to calculate the radius of critical bubble embryo formed on the JCM surface. Because the highest O_2 concentration appears at the pole of the JCM's catalytic surface, it is assumed that the bubble embryo was attached to this pole and used Equ. 4-6 to find the radius of the critical bubble embryo. Figure 4-2 shows that when the radius of JCM is smaller than $7.4 \mu m$, no finite-sized critical bubble embryo can be formed on the JCM's surface. This cut-off radius of $7.4 \mu m$ is similar to prior experimental observations that, when R_p is smaller than $5 \mu m$, bubble rarely forms on individual JCMs⁸⁶. The smaller cut-off radius for bubble formation in the experimental systems is likely caused by the fact that, in experiments, many JCMs exist in the solution and the production of O_2 from them elevates the O_2 concentration in the bulk solution. Since such an elevation of the O_2 concentration is not taken into account in the analysis, it is expected to overestimate the cut-off radius of JCMs for bubble formation.

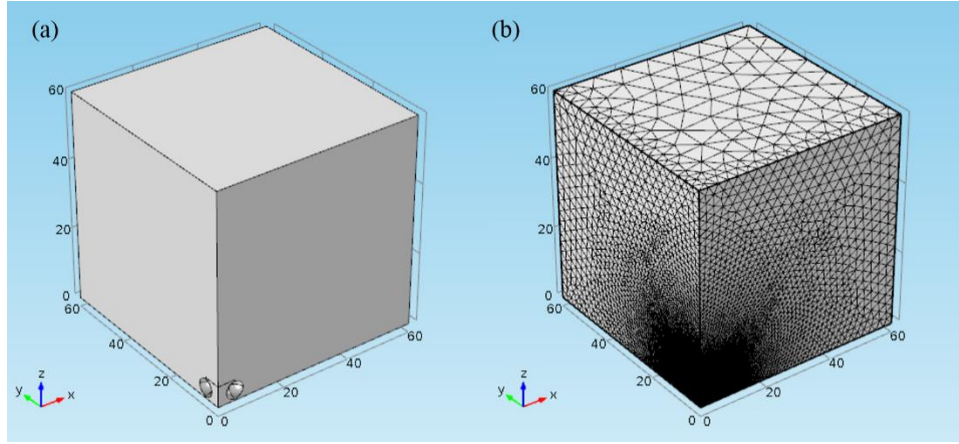


Figure 4-5. The simulation domain and mesh used for computing the oxygen concentration near a cluster of four JCMs positioned above a substrate.

The above results show that increasing JCM's size or the O_2 production rate on its surface facilitates the bubble formation. Equation 4-7 suggests that increasing the O_2 concentration in the bulk solution (i.e., c_∞) has a similar effect. This is supported by the observation that bubble can form when several small JCMs form a cluster (see Fig. 3-1). To understand this semi-quantitatively, the O_2 concentration field near a cluster of JCMs is examined by solving the diffusion equation for O_2 transport. these JCMs are assumed to be located at $R_p/2$ above the solid substrate. This assumption is consistent with the experiments shown in Chapter 3 in which the JCMs were usually found at a short distance above the solid substrates. The cluster contained two and four JCMs with a radius of $2.5 \mu m$. The distance of gaps (indicated by dashed lines in Fig. 4-6) between JCMs was $2R_p$. The governing equations and boundary conditions for the oxygen concentration are the same as Equations 4-(10-13). In addition, a no-flux condition is applied on the substrate surface

$$-D\nabla c(\mathbf{x}, t) \cdot \mathbf{n} = 0 \quad \text{on substrate surface} \quad (4-14)$$

Since the system considered here involves a cluster of four JCMs and the substrate, a 2D asymmetrical model is no longer applicable. Here, taking advantage of symmetry, it only needs to

simulate one-quarter of the entire system. Figure 4-5 shows the rectangular simulation domain with two JCMs. The rectangular domain has a size of $60\mu\text{m} \times 60\mu\text{m}$ and is divided into 1.7×10^7 tetrahedral elements. For the system mentioned above, the concentration field was also solved using COMSOL's chemical transport modules and stationary solver.

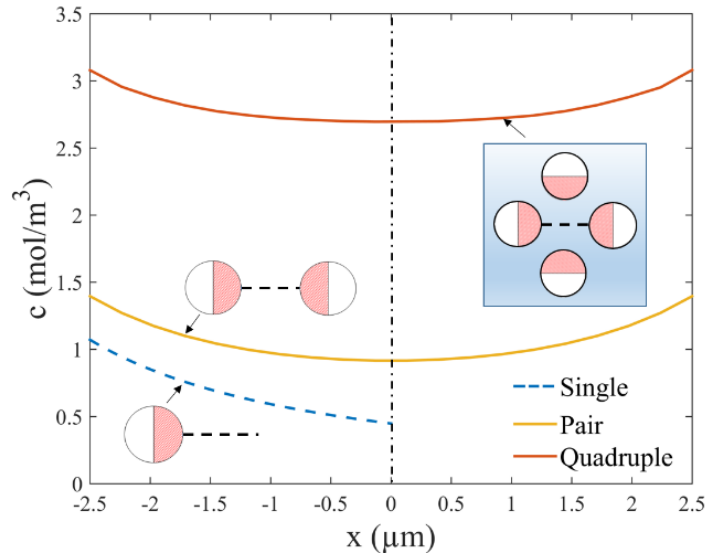


Figure 4-6. The O_2 concentration distribution near singlet JCMs and JCMs in small clusters. The JCMs ($R_p=2.5\mu\text{m}$) are situated at $1.25\mu\text{m}$ above the solid substrate and their catalytic surface faces the center of the cluster. The center-to-center distance between the opposing JCMs in a cluster is $10\mu\text{m}$. The O_2 production rate on the JCM's catalytic surface is $1.08 \times 10^{-3}\text{mol}/(\text{m}^2 \cdot \text{s})$. The concentration profile is shown along the dashed lines shown in the inset. $x=0$ is defined as the center of the cluster or at the position 2.5mm away from the pole of a singlet JCM.

The simulation results indicated that the highest O_2 concentration in the system occurs on the JCM's catalytic surface. Figure 4-6 shows the O_2 concentration profiles along the line passing through the JCM's center and the pole of its catalytic surface, and two effects of the clustering of JCMs are evident. First, as illustrated in the Fig. 4-6, the highest O_2 concentration on the surface of a JCMs within a cluster is higher and it increases as the number of JCMs forming the cluster increases, e.g., the maximal O_2 concentration near a cluster of two (four) JCMs is 27% (182%)

higher than near an isolated JCM with the same size. In fact, the maximal O_2 concentration on the surface of a $2.5\ \mu\text{m}$ -radius JCMs within a four-JCMs cluster is higher than that on the surface of an isolated, $7\ \mu\text{m}$ -radius JCM, which can form bubbles on its own.⁸⁶ Second, the O_2 concentration also drops more slowly as moving away from the JCM surface. Together, these two effects enable the formation of critical bubble embryos on the surfaces of JCMs that are too small to generate bubbles by themselves, i.e., bubbles can be formed by a cluster of JCMs with radius smaller than the cut-off radius of isolated JCMs.

Since the highest O_2 concentration in a JCM system occurs on the JCM's catalytic surface regardless whether it exists in isolation or in a cluster, the critical bubble embryos should appear preferably on the catalytic surfaces of JCMs and then grow. However, Fig. 3-2a shows that, for JCMs forming a cluster, the bubble appears mostly on the substrate rather than on the surface of any JCMs in the cluster. To understand this apparent paradox, note that these observations were made when the bubble growth-burst cycle has already repeated many times, and thus they do not necessarily show where bubbles are formed during the very first bubbling cycle. It is suggested that the apparent paradox is a result of the switching of bubbling site during the first bubbling cycle. Figure 4-7 shows a schematic for the steps involved in this process: (1) a critical bubble embryo initially forms on the catalytic surface of one JCM; (2) the critical bubble embryo grows to a large size ($R_b \sim 50\text{-}100\ \mu\text{m}$) and touches the substrate; (3) the fully-grown bubble collapses and leaves small residual bubbles on the substrate and JCMs. Note that small residual bubbles are frequently reported for bubbles in boiling experiments¹⁷⁹ and its existence in the JCM system is consistent with the image shown in the right panel of Figure 1c. The residual bubble left on the substrate should be much larger than the residual bubble left on the JCM's surface due to the JCM's small size ($R_p \sim 2.5\ \mu\text{m}$). Because of the Ostwald ripening effects, the large residual bubble on the

substrate grows while the smaller residual bubble on the JCM surface shrinks⁸⁶. Consequently, in the subsequent bubble growth-burst cycles, the bubble is observed on the substrate rather than on the JCM's surface.

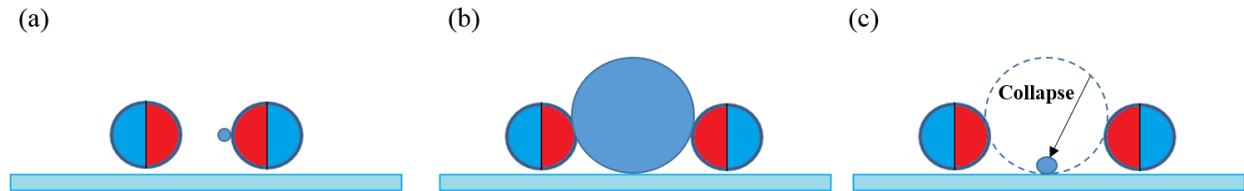


Figure 4-7. A schematic of the switching of bubbling site in the first bubbling cycle. A critical bubble embryo is formed on the JCM surface and grows to touch the substrate. Following the burst of the fully-grown bubble, a residual bubble is left on the substrate, which serves as the bubbling site in subsequent bubble growth-burst cycles.

4.2 Bubble Growth in JCM Systems

Next, numerical simulations were used to understand the growth behavior of the bubbles shown in Fig. 3-2 and 3-4, i.e., when a bubble is fed by the oxygen released from several JCMs, the growth of its radius follows a scaling law of $R_b \sim t^{0.7 \pm 0.2}$. This growth law deviates from the conventional supersaturation-driven bubble growth ($\sim t^{0.5}$). In the experiments, a single bubble is surrounded by a ring of N JCMs, and both the bubble and JCMs are immersed in a liquid film. In the simulation system (see Fig. 4-8), the bubble and liquid film are explicitly modeled while the ring of N JCMs was lumped into a torus structure. The inner surface of the torus structure (colored red in Fig. 4-8b), representing the catalytic surfaces of the JCMs, faces towards the bubble. A uniform outward flux of O_2 , J_{O_2} is imposed on this inner surface of the torus structure (J_{O_2} is chosen so that the net O_2 flux on the torus' surface matches the net flux of O_2 from the N JCMs). This treatment allows us to perform the simulations in a two-dimensional axisymmetric space while

still capturing the essential physics of the bubble growth.

In the simulations, a bubble with an initial radius of R_0 is placed on the substrate with a zero contact angle. At $t < 0$ s, the solution is at rest and in chemical equilibrium with the bubble, i.e. it has an O_2 concentration given by equation (3). This setup mimics the fact that, after the disappearance of a large bubble from a site on the substrate, a small bubble is left at the same site. At $t > 0$ s, the O_2 generation on the inner surface of the torus is enabled, and the torus radius L_p decreases at a constant speed of V_p . The latter is consistent with the results in Chapter 3. At $t > 0$, the generation of O_2 and the transport of O_2 and fluids in the liquid film (i.e., the shaded region in Figure. 4-8a) are solved to predict the growth of bubble. Assuming that, during its growth, a bubble stays spherical and its south pole is pinned to the substrate, which are consistent with experimental observations in Chapter 3. Similarly, an initial bubble radius of $R_0 = 10 \mu m$ is used. The torus representing the ring of N JCMs is placed on the substrate and has an initial radius of $L_p = 40 \mu m$. As the dimension of the simulation domain is much smaller than the liquid film used in experiments, the top surface of the simulated liquid film is treated as flat¹⁶³. The thickness of the liquid film, H , is $100 \mu m$, similar to that in the experiments. the length of the simulation domain L , is set to $200 \mu m$. Using a larger length only changes the result slightly. The detailed mathematical model and numerical implementation of the simulations are summarized below.

As mentioned above, to reduce the computational cost, the ring of JCMs around a bubble is lumped into a continuous torus structure, and it is assumed that the catalytic surfaces of JCMs all face the bubble center (see Fig. 4-8b). Taking advantage of the symmetry of this simplified system, the bubble growth in this system can be simulated in 2D axisymmetric space. Because of the small Reynolds number involved, the flow field observes the Stokes equations. The transport of oxygen molecules in the solution observes the convection-diffusion equation. Because the gas inside has

low viscosity and density compared to those of the liquid solution, the air flow inside the bubble is neglected. Since the focus of this simulation is on the bubble growth, the motion of the JCM is prescribed as the value measured from experiments instead of directly determining its motion by solving the underlying Marangoni flow. Specifically, each JCM moves at a constant speed of V_p during the growth of the bubble.

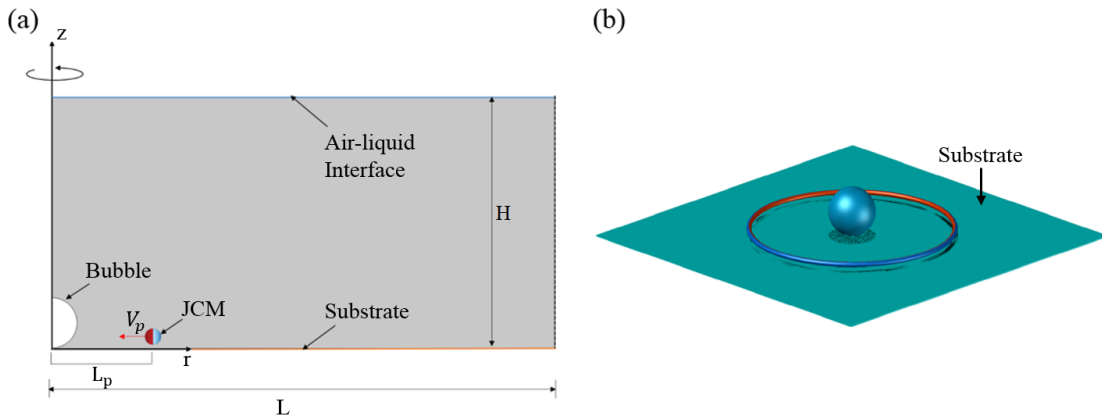


Figure 4-8. Simulation of bubble growth due to remote feeding by a ring of JCMs. (a) Schematic of the simulation system; (b) A 3D sketch of the system. The N JCMs surrounding the bubble are lumped into a torus structure with its inner surface (marked in red) as catalytic surface and its outer surface (marked in blue) as the neutral surface.

The simulation starts at the instant right after the burst of the previous bubble. To prevent the shrinkage of this bubble, the dissolved oxygen in the entire solution is assumed to be in equilibrium with the oxygen gas inside the residue bubble. Specifically, the initial O_2 concentration in the liquid solution is set to the liquid saturation concentration computed from Equ. 4-3. All fluids in the system assumed to be at rest before the simulation starts.

The mathematical model for the bubble growth driven by “remote feeding” by JCMs consist of two sets of equations governing the reaction/transport of the oxygen molecules and the dynamics of the fluids and the JCM. The oxygen concentration field, c , is governed by the convection-diffusion equation

$$\frac{\partial c}{\partial t} + \mathbf{u} \cdot \nabla c = \nabla \cdot (D \nabla c) \quad (4-15)$$

The oxygen concentration on the bubble surface is set to the equilibrium value corresponding to the oxygen pressure inside the bubble.

$$c|_{\Gamma_1} = \kappa_H \left(p_\infty + \frac{2\sigma}{R_b} \right) \quad (\text{Saturation at bubble surface}) \quad (4-16)$$

Since the dissipation of oxygen from the solution to the environment through the air-liquid interface is small, zero oxygen flux is applied on both the air-liquid interface and the substrate.

$$-D \nabla c(\mathbf{x}, t) \cdot \mathbf{n}|_{\Gamma_4} = 0 \quad (\text{Air-liquid interface}) \quad (4-17)$$

$$-D \nabla c(\mathbf{x}, t) \cdot \mathbf{n}|_{\Gamma_5} = 0 \quad (\text{Non-penetrable substrate}) \quad (4-18)$$

$$c|_{\Gamma_6} = \kappa_H \left(p_\infty + \frac{2\sigma}{R_0} \right) \quad (\text{Bulk solution}) \quad (4-19)$$

The no-flux and fixed oxygen flux are applied on the neutral and catalytic surface of the JCM, respectively.

$$-D \nabla c(\mathbf{x}, t) \cdot \mathbf{n}|_{\Gamma_2} = 0 \quad (\text{Non-penetrable neutral surface of the JCM}) \quad (4-20)$$

$$-D \nabla c(\mathbf{x}, t) \cdot \mathbf{n}|_{\Gamma_3} = J_{O_2} \quad (\text{Catalytic surface of JCM}) \quad (4-21)$$

The flux on inner surface of torus structure is computed using

$$J_{O_2} = \frac{N \dot{m}_p}{A_t^i(t)} \quad (4-22)$$

where R_p is the radius of the JCM, \dot{m}_p is the oxygen flux on the catalytic surface of each JCM, N is the total number of JCMs lumped as the torus structure, and $A_t^i(t)$ is area of the torus structure's surface facing the bubble at time t . The fluids are modeled as incompressible and Newtonian. Since the Reynolds number is small, the inertia effect is negligible. Thus the flow field is governed by

$$\nabla \cdot \mathbf{u} = 0 \quad (4-23)$$

$$-\nabla p + \mu \nabla^2 \mathbf{u} = \mathbf{0} \quad (4-24)$$

where ρ and μ are the density and viscosity of the solution, respectively, p is the pressure. In simulations, an inward velocity of $-V_p$ pointing to the bubble center is prescribed to the torus structure. A zero velocity is prescribed to the torus structure in the height (z -) direction. V_p was varied within the range of JCM speed observed experimentally. The growth of the bubble is driven by the diffusion of oxygen molecules through its surface. Consistent with experimental observations, it is assumed that, during the growth of a bubble, the bubble remains spherical and its south pore is in touch with the substrate with a zero contact angle. With the above description, the boundary conditions are obtained:

$$\mathbf{u}|_{\Gamma_2 \& \Gamma_3} = \mathbf{u}_p \quad (\text{prescribed JCM motion}) \quad (4-25)$$

$$\mu \frac{\partial \mathbf{u}}{\partial \mathbf{n}}|_{\Gamma_4} = 0 \quad (\text{no tangential stress on bubble surface}) \quad (4-26)$$

$$\mathbf{u}|_{\Gamma_5} = 0 \quad (\text{no-slip condition}) \quad (4-27)$$

$$\mu(\nabla \mathbf{u}_2 + (\nabla \mathbf{u}_2)^T) \cdot \mathbf{n}|_{\Gamma_6} = 0 \quad (\text{stress-free open boundary}) \quad (4-28)$$

The increase of the bubble radius bubble growth is governed by

$$\frac{dR_b}{dt} = \frac{1}{4\pi R_b^2 \rho} \frac{dm}{dt} = \int_{\Gamma_1} \frac{1}{4\pi R_b^2 \rho} \dot{q}_{O_2} ds \quad (4-29)$$

where \dot{q}_{O_2} is inward mass flux at bubble surface, which is obtained from mass transfer equations.

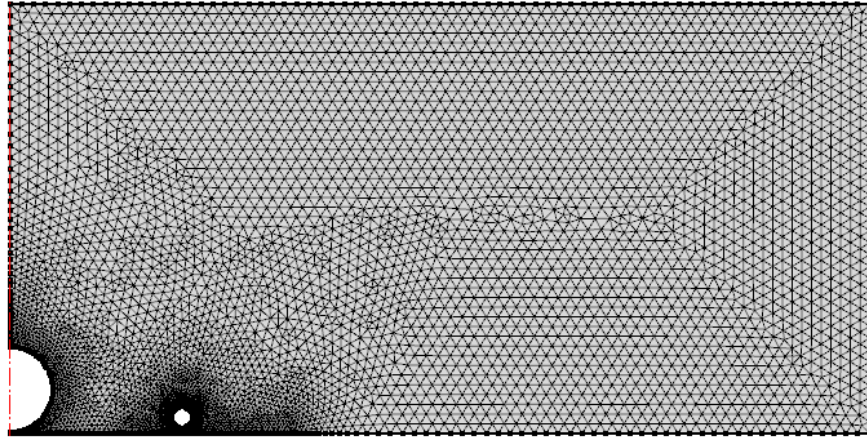


Figure 4-9. A typical mesh used in simulations of the growth of a bubble fed by a ring of JCMs around it.

Equations 4-(15-29) form the complete mathematical description of the bubble growth process. To solve these equations, the commercial finite element package COMSOL was used.¹⁴⁴ The computational domain is discretized into a triangular mesh. A typical mesh used in simulations, which consisted of 10520 free triangle elements, is shown in Fig. 4-9. The Arbitrary Lagrangian-Eulerian (ALE) method¹⁴⁵ was utilized to handle the movement of JCM and the bubble-liquid interface. During each simulation, multiple remeshing was typically performed to maintain the mesh quality. Mesh studies were also performed to ensure that the results are independent of the mesh size.

Figure 4-10 shows the log-log plot of the bubble growth behavior predicted by the simulations. The number of JCMs surrounding the bubble and their radial velocity toward the bubble are varied within the range found experimentally.¹⁰¹ Specifically, the number of JCMs surrounding the bubble is taken into account implicitly by changing the O₂ flux on the inner surface of the torus structure, see Equ. 4-22. The results show that bubble growth approximately follows a power law, $R_b \sim t^\eta$, and the exponent η is in the range between 0.69 to 0.8, which quite well with the experimental

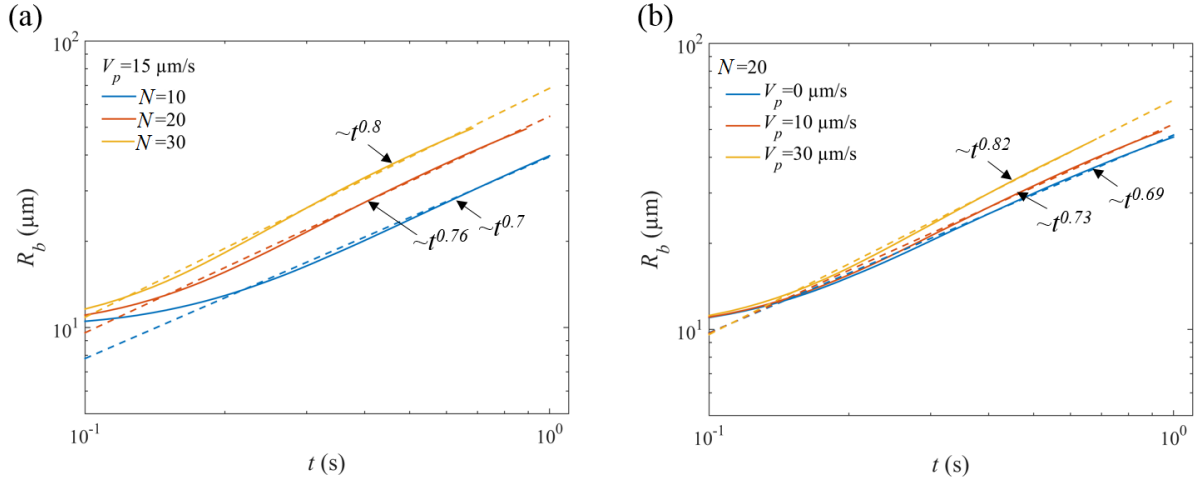


Figure 4-10. Time evolution of the bubble radius (R_b) predicted by simulations. (a) The effect of the number (N) of JCMs in the ring surrounding the bubble on the bubble growth (the inward velocity of the JCM ring V_p is fixed at $15 \mu\text{m/s}$). (b) The effect of the JCM inward velocity toward the bubble on its growth (the number of JCMs in the ring surrounding the bubble is fixed at $N=20$).

value $\eta=0.7\pm 0.2$. For $V_p=15 \mu\text{m/s}$, it is found that, as N increases from 10 to 30, the bubble grows faster and η of the fitted power law increases from 0.7 to 0.8 (Fig. 4-10a). The same trend is observed for when V_p increases from 0 to $30 \mu\text{m/s}$ while N is fixed at 20 (Fig. 4-10b). The dependence of the power law exponent on N and V_p helps explain the scattering of the power law exponent observed experimentally because different bubbles usually have different N and V_p associated with them in the experiments. During the early stage ($t < 0.2 \text{ s}$), the growth of the bubble is very slow and only gradually reaches the $R_b \sim t^n$ ($n \sim 0.7$) scaling law. The slow growth and gradual transition to the power law scaling are caused primarily by the surface tension effect. In our simulations, the initial background oxygen concentration ($c_{O_2,l}^0$) is used to set the initial bubble radius according to Eqn. 4-1 and 4-3 and the oxygen concentration on the bubble surface ($c_{O_2,b}$) is identical to $c_{O_2,l}^0$. Therefore, the bubble does not grow till the oxygen generated by JCMs diffuses to the bubble surface. Even after the oxygen concentration near the bubble is elevated by such

diffusion, $c_{O_2,b}$ is still pinned to a high value by the surface tension effect: since the bubble is small, the capillary pressure due to surface tension dominates the oxygen pressure inside bubble, which in turn sets $c_{O_2,b}$ to a high value via Henry's law. Therefore, the mass flux of oxygen into the bubble is small and the bubble grows very slowly. As the bubble grows larger, the surface tension effect becomes weaker and the bubble growth eventually reaches the $R_b \sim t^n$ ($n \sim 0.7$) scaling law. We note that the observed slow growth of bubble during the initial stage is similar to that observed for the growth of bubbles in uniformly superheated liquids,¹⁸⁰⁻¹⁸¹ which has been investigated extensively in boiling research. In addition, the bubble grows to the maximum size in ~ 1 s, a time scale in general agreement with the experiments in Chapter 3 (see Fig. 3-3).

The anomalous bubble growth with an exponent of $\eta > 0.5$ is mostly a result of the cooperative action of supersaturation-induced growth and mutual motion between the JCMs and the growing bubble. The growth of bubble due to the diffusion of gas molecules from a liquid solution toward its surface leads to a growth law of $R_b \sim t^{0.5}$,¹²³ and this mode of bubble growth is at work in the present system. While the bubble is initially in equilibrium with its surrounding solution, the production of oxygen in the solution by catalytic reactions leads to a supersaturation of oxygen. This causes the bubble to grow. In addition, as the bubble grows, the pressure in the bubble drops due to the reduction of the Laplace pressure. This leads to a reduction of the oxygen saturation concentration at the liquid-bubble interface, which in turn drives oxygen diffusion toward the bubble to feed its growth. Finally, as the bubble grows, the distance between the JCMs and the bubble surface reduces because of the expansion of the bubble and the inward movement of the JCMs. This relative motion facilitates the transport of oxygen into the bubble, and its effect can be observed in Fig. 4-10b: as V_p increases from 0 to 30 $\mu\text{m/s}$, the exponent η increases from 0.69 to 0.82.

4.3 Bubble Collapse in JCM Systems

Finally, the peculiar bubble collapse phenomena are studied: bubbles with a radius of 50-100 μm disappeared rapidly ($<1\text{ms}$) at the end of each bubbling circle. Besides this extremely short time scale for the bubble collapse, it was often found that, at same bubbling site, bubbles from different circles approached similar maximum radius before collapsing. It is suggested that the liquid-air interface plays a fundamental role in the above peculiar behaviors. Specifically, while rarely highlighted, the dynamics of JCMs were often studied not in a bulk solution but in thin liquid films: in many experiments (for example, experiments in Chapter 3), liquid droplets containing H_2O_2 were first deposited onto hydrophilic substrates, and droplet loaded with JCMs was next deposited on the thin film of H_2O_2 . Hence, this bubble collapse is likely caused by the coalescence of a bubble with the air-liquid interface. This hypothesis helps explain why the maximal bubble size at a given bubbling site is usually same (as bubble tends to merge with the air above the air-liquid interface once its size approaches the thickness of the liquid film near the bubbling site). Further, the rapid collapse of the bubble is consistent with the short time scale of the coalescence between the bubble and the air above the air-liquid interface. The coalescence between a bubble of radius R_b with a planar air-liquid interface is characterized by the surface tension time scale¹⁸²⁻¹⁸⁵

$$t_c = \sqrt{\frac{\rho_l R_b^3}{\sigma}} \quad (4-30)$$

where ρ_l is the density of liquid phase. For a bubble with a radius of $50\mu\text{m}$ merging with the air-water interface, $t_c \sim \text{O}(50\mu\text{s})$, which is in line with the rapid collapse of bubbles reported earlier.⁸⁶

To further validate this hypothesis, a simulation of micro-bubble merging with an air-liquid interface is performed to determine the time scale of this process. In the simulation system, a

bubble with $R_b=50 \mu m$ is placed at a distance of $0.1 \mu m$ above a substrate covered by a liquid film with a thickness of $100 \mu m$. At $t=0$, the north pole of the bubble coalesces with air-liquid interface, as shown in Fig. 4-11. The system is then set into motion by solving the Navier-Stokes equations to track the evolution of bubble surface driven by surface tension. The mathematical model and numerical implementation of this system are summarized below.

Figure 4-11 shows the simulation domain, with each domain and boundary labeled. For simplicity, the air/water is chosen as the gas/liquid phase in the system, because of their comparable physical properties to oxygen and hydrogen peroxide solution. Initially, the domain Ω_1 is occupied by air, while the domain Ω_2 is occupied by water. At $t = 0s$, the bubble merges with the atmosphere under the effect of surface tension. To track the air-liquid interface during the coalescence process, the coupled level set and volume-of-fluid method (CLSVOF) is employed for solving the two-phase flow.¹⁸⁶

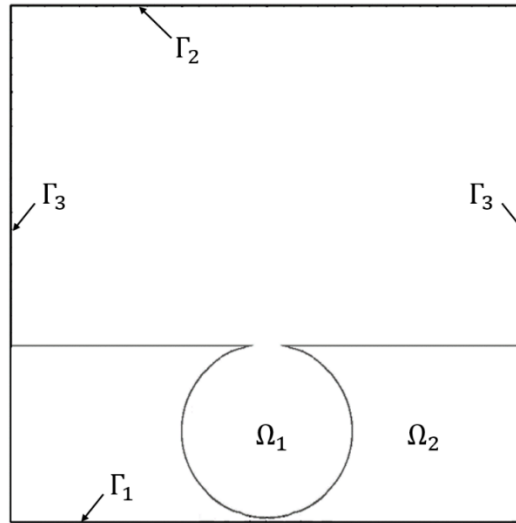


Figure 4-11. The system used to investigate the coalescence of a bubble with an air-liquid interface.

Assume both air and water are incompressible, the continuity and momentum equations for the

single-phase regions (i.e., either the gas or the liquid) are¹⁸⁷

$$\nabla \cdot \mathbf{u} = 0 \quad (4-31)$$

$$\rho(\phi) \left(\frac{\partial \mathbf{u}}{\partial t} + \nabla \cdot \mathbf{u}\mathbf{u} \right) = -\nabla p + \rho(\phi)\mathbf{g} + \nabla \cdot [\mu(\phi)(\nabla \mathbf{u} + (\nabla \mathbf{u})^T)] - \mathbf{F}_{sf} \quad (4-32)$$

where density ρ and viscosity μ depends on the level-set function ϕ ,

$$\rho(\phi) = \rho_g[1 - H(\phi)] + \rho_l H(\phi) \quad (4-33)$$

$$\mu(\phi) = \mu_g[1 - H(\phi)] + \mu_l H(\phi) \quad (4-34)$$

where $H(\phi)$ is the Heaviside function. The surface tension term \mathbf{F}_{sf} is given as

$$\mathbf{F}_{sf} = \sigma \kappa(\phi) \mathbf{n} \delta(\phi) \quad (4-35)$$

where σ is the surface tension of water, $\kappa(\phi)$ is the curvature of the interface, \mathbf{n} is the normal vector, and $\delta(\phi)$ is the smoothed delta function. The interface is marked by the level set (LS) function, who is evolved using

$$\frac{\partial \phi}{\partial t} + \mathbf{u} \cdot \nabla \phi = 0 \quad (4-36)$$

$$\phi(\mathbf{r}, t) \begin{cases} < 0 & \text{in the gas region} \\ = 0 & \text{at the interface} \\ > 0 & \text{in the liquid region} \end{cases} \quad (4-37)$$

When discretizing the level-set advection equation, the volume-of-fluid function α is also simultaneously solved using

$$\frac{\partial \alpha}{\partial t} + \nabla \cdot (\mathbf{u}\alpha) = 0 \quad (4-38)$$

Taking advantage of the symmetry of the simulation system, the coalescence process is simulated in the 2D axisymmetric domain. The simulation domain has a dimension of $200\mu\text{m} \times 300\mu\text{m}$.

Since focus of this study is on the behavior of bubble, the side walls Γ_3 is treated as slip walls. Then the following boundary conditions are used to solve the two-phase flow

$$\mathbf{u}|_{\Gamma_1} = 0 \quad (\text{on substrate}) \quad (4-39)$$

$$P|_{\Gamma_2} = 0 \quad (\text{far-field atmosphere}) \quad (4-40)$$

$$\mu \frac{\partial \mathbf{u}}{\partial \mathbf{n}}|_{\Gamma_3} = 0 \quad (\text{slip wall}) \quad (4-41)$$

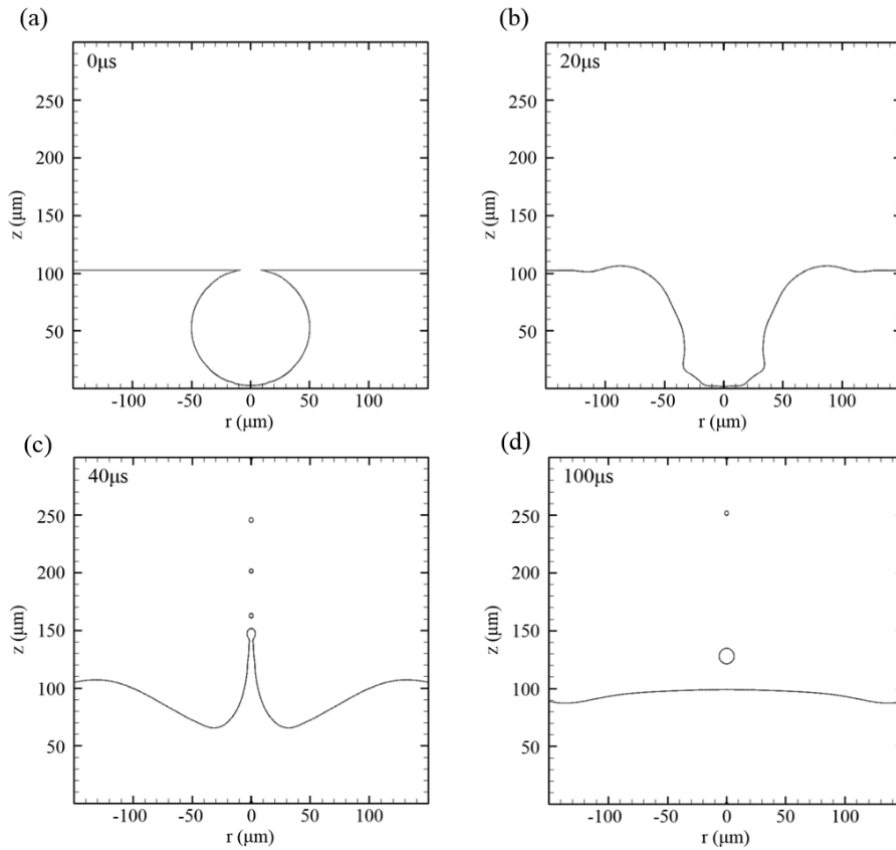


Figure 4-12. Coalescence of a bubble inside a liquid film with the air-liquid interface. Once the bubble's north pole merges with the air above the liquid-air interface, the bubble collapses rapidly under the action of surface-tension-induced flows.

At $t < 0$ s, the domain Ω_1 is occupied by water, while the domain Ω_2 is occupied by air. All fluids and interfaces are static. At $t = 0$ s, the north pole of the bubble is set to merge with the liquid-air interface and the fluid flow and evolution of the air-liquid interface are determined by solving Equ.

4-(31-41). The above model is solved by using the commercial finite volume package FLUENT.¹⁸⁷ The computational domain were discretized using rectangular elements, and the mesh was locally refined near the air-liquid interface and the liquid-solid boundary. Mesh studies were performed to ensure that the results are independent of the mesh size.

Figure 4-12 shows the snapshots from the simulation for $t = 0, 20, 40,$ and $100 \mu s$, respectively. These snapshots show that a bubble with an initial radius of $50 \mu m$ disappears within $100 \mu s$ after it merges with the air-liquid interface, thus supporting the idea that the coalescence of a bubble with the air-liquid interface can lead to the rapid bubble collapse reported in prior experiments.

4.4 Conclusions

While bubbles often play an essential role in the operation of JCMs, their behaviors are not yet well understood. In this work, some of the behaviors related to the formation, growth, and collapse of bubbles in JCM systems reported in recent experiments are investigated. First, a criterion is derived for the formation of bubbles on JCM's surface based on consideration of the mass transfer near the JCM and thermodynamics of bubble nucleation. Using this criterion, it is explained why bubbles are not observed on very small isolated JCM, why the formation of bubbles on the JCM surface depends on the catalytic activities of the JCM surface, and why bubble can form near a cluster of small JCMs. The numerical simulation of the growth of bubble fed by a ring of JCMs produced an anomalous growth law of $R_b \sim t^\eta$, where η is larger than 0.5 and depends on the number of JCMs in the ring and the inward velocity of the JCM toward the bubble. This uncommon bubble growth behavior was caused by the combination of supersaturation environment and relative movement between growing bubble and the JCM. Finally, it is suggested that the rapid bubble collapse observed in recent experiments was due to the coalescence of the bubble with the

air-liquid interface. The hypothesis was supported by the agreement between the short time scale of such coalescence observed in experiments and in the simulations.

The present study highlights the importance of the mass transport in regulating the bubble formation and hence the transition of JCM propulsion between self-diffusiophoresis to bubble-propulsion. It shows that interesting new bubble behavior can emerge when multiple JCMs form a cluster and/or when bubbles interact with their environment (e.g., liquid-air interfaces). Since JCMs often do not operate in isolated and bulk solution environments, these behaviors warrant further study and should be taken into account when designing and using JCMs. While the dynamics of JCMs in these situations will be more complex than those in bulk/isolated conditions and thus more challenging to understand, they also provide exciting new opportunities to realize new JCM functions.

Chapter 5. Particle Manipulation using AC Magnetic Fields[§]

In this Chapter, a novel method of using a non-uniform alternating magnetic field (nuAMF) to manipulate small magnetic objects in fluids is analyzed. Different from the conventional manipulation methods introduced in Chapter 1, the manipulation targets of this new method can be arbitrary anisotropic shaped magnetic clusters (MCs) that spontaneously formed by the aggregation of ferromagnetic Fe₃O₄ nanorods (NRs). These clusters perform translational motions near substrate surfaces and move away from the solenoid that is used to generate the H-field. This translation motion induced by nuAMF cannot simply be explained by the classical magnetic particle manipulation mechanisms. To understand such a translational motion, a theoretical model that combines surface effects and the magnetophoresis force is developed and tested through numerical simulations. Using this model, the dynamics of MCs during this magnetic manipulation process is analyzed and explained.

5.1 Brief Summary of Experimental Observations

Suspensions loaded with Fe₃O₄ NRs (0.1 mg ml⁻¹) was first deposited into a rectangular glass capillary tube (height: 100 μm and width: 2 mm). Due to the relatively high concentration and ferromagnetic property of Fe₃O₄ NRs, they naturally form small MCs. During the experiment, a

[§] This chapter is adapted from the following paper (Ref. 188):

W. J. Huang, F.C. Yang, L. Zhu, R. Qiao, and Y.P. Zhao, “Manipulation of magnetic nanorod clusters in liquid by non-uniform alternating magnetic fields”, *Soft Matter*, 2017(13), 3750-3759.

Permission for using this paper in this dissertation has been granted by the Royal Society of Chemistry. The experimental work reviewed briefly in this chapter was performed by Huang, W. J., Zhu, L. and Zhao, Y. P. of University of Georgia.

solenoid was placed at the left-hand side. The sample was placed $L = 4.5$ cm away from the front face of the solenoid and, according to the calibration curve, the maximal H-field generated at $I_0 = 2$ A was 4.2 mT and the field gradient was -0.13 mT mm^{-1} .

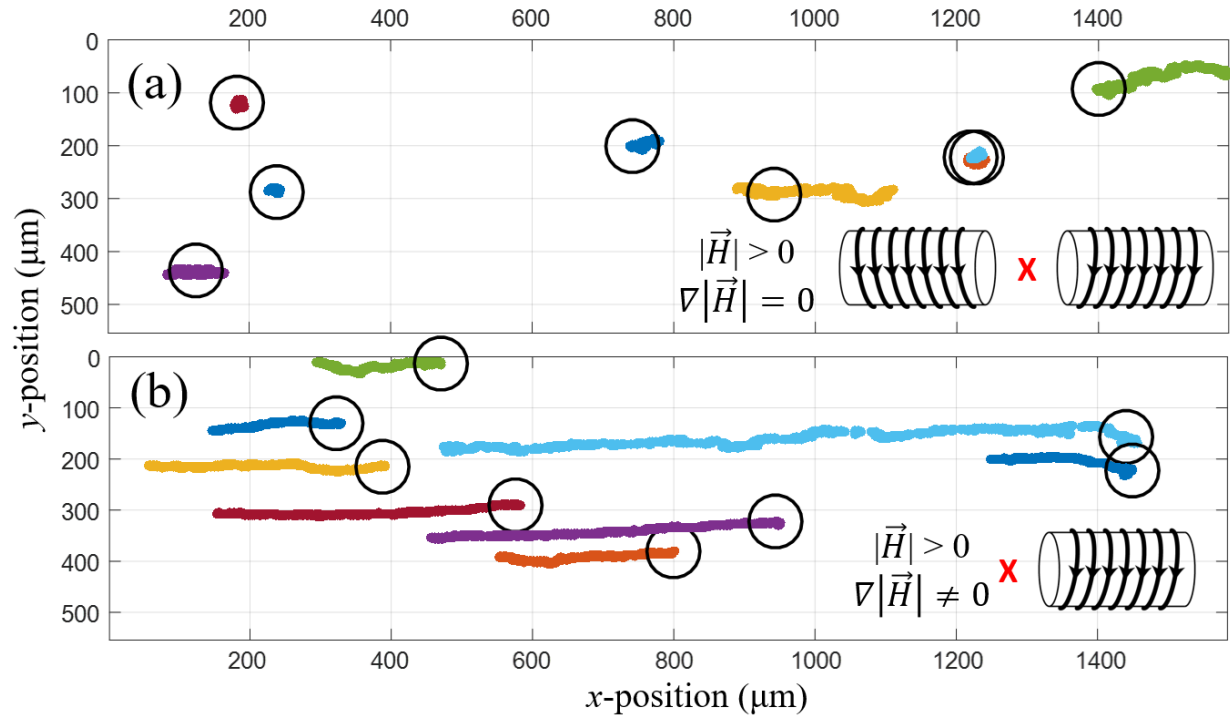


Figure 5-1. Trajectories of the MCs at two different field configurations: (a) a uniform alternating magnetic field; (b) a nuAMF generated by a single solenoid.

One can observe that when the nuAMF is applied, the MC starts to flip out of the x - y plane while performing a translational motion toward the right side (away from the solenoid). The induced translational motion is mostly along the x -direction with a large x -component speed $v_x = 77 \mu\text{m s}^{-1}$ and a small y -component speed $v_y = 8.8 \mu\text{m s}^{-1}$. Unlike a permanent magnet pulling a magnetic object, the MCs move away from the solenoid (see Fig. 5-1b), and the speed of the translation motion is closely related to the size of the MC. The experimental results indicate that there are three necessary conditions for the translational motion to occur: (a) The MCs must locate near a substrate surface. Controlled experiment shows that, once the MCs is far away from the

substrate, this translational motion of MCs vanishes. (b) The H-field must be alternating and strong enough to induce a rotation; (c) The H-field must be non-uniform (see Fig. 5-1a).

This nuAMF induced translational motion of MCs is affected by both the current input (I_0) and the frequency (f_H) of the external field. A systematic experiment with different I_0 for a fixed $f_H = 10$ Hz at the same location is performed to investigate how MCs move under different field conditions. Figure 5-2 shows the relationship between translational speed of MCs v and the current input I_0 . The results showed that, when I_0 is low ($I_0 < 0.5$ A), the MCs would not move but only vibrate. As I_0 increases, all MCs start to move and the moving speed v increases monotonically with I_0 . When I_0 reaches a relatively large value, v approaches a constant.

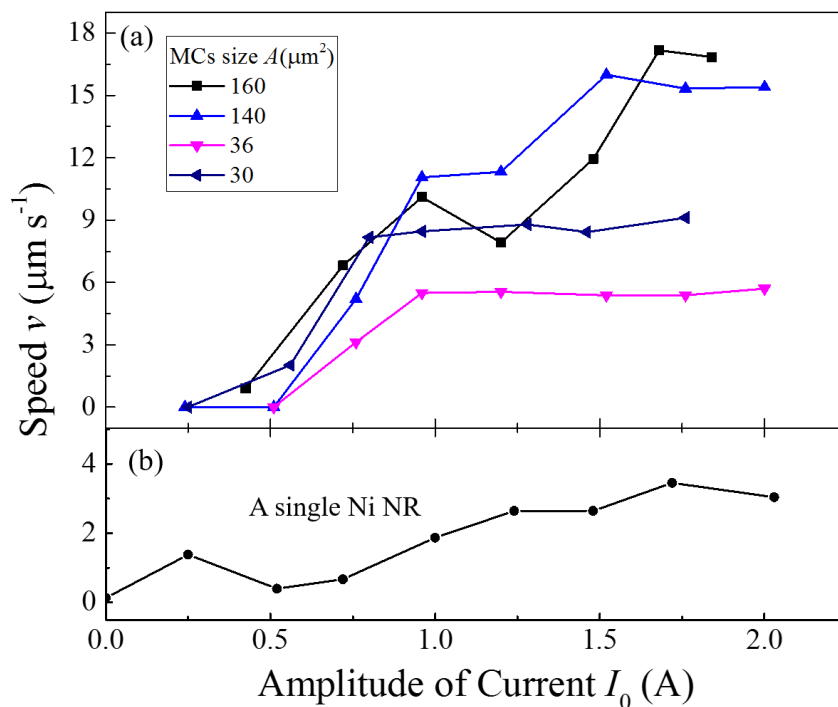


Figure 5-2. (a) The translational speed v of MCs and (b) a single Ni NR versus different I_0 ($f_H = 10$ Hz).

Other than I_0 , the effect of field frequency f_H is investigated as well. By systematically increasing f_H while keeping $I_0 = 2$ A, the relationship between v and f_H is obtained as shown in Fig. 5-3. For different sized MCs, the v versus f_H relationship follows a similar trend: when f_H increases

initially, v increases dramatically; then v reaches a maximum value when f_H increases to a threshold value f_H^m ; when f_H increases further, v gradually decreases, till it approaches to zero when $f_H \geq 140$ Hz.

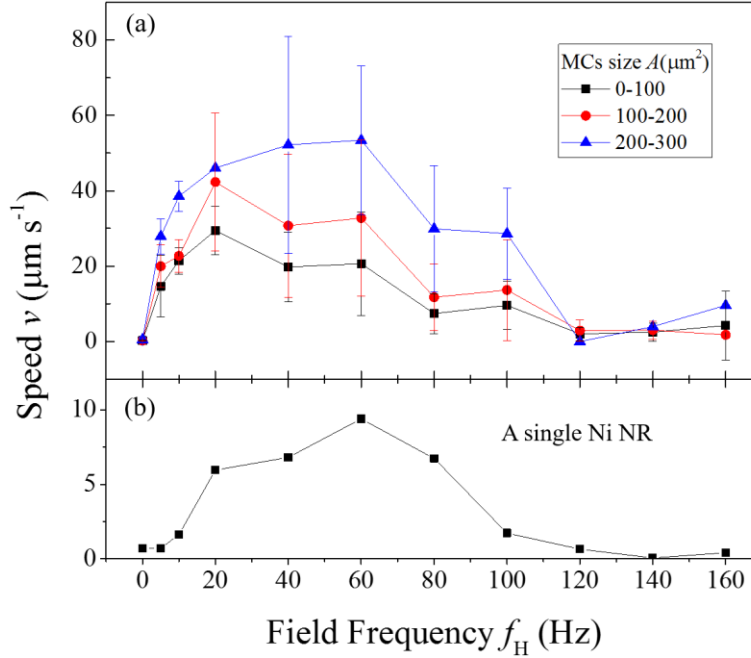


Figure 5-3. (a) The plot of the translational moving speed v of different sized MCs and (b) a single Ni NR as a function of nuAMF frequency f_H . Here $I_0 = 2$ A.

Moreover, FFT analysis of displacement of the MCs shows that the nuAMF-induced motion exhibits a fluctuation with a major frequency twice that of the field frequency f_H . This double frequency feature of MC motion holds for a field frequency $f_H < 80$ Hz. The underlying mechanisms of these experimental observations are investigated in the following sections.

5.2 Theoretical Analysis

5.2.1 Theoretical Model

According to classical hydrodynamic theory, if a MC is performing a rotational motion in a bulk solution, due to the small Reynolds number ($\text{Re} < 0.01$) and the symmetry of its rotation, its

rotation should not induce a translational motion. However, if such a rotation occurs near a wall, the wall will break the rotational symmetry and could induce a translational motion of the MC.^{56, 128} According to the experiments, the MCs are very close to the bottom substrate (within 10 μm distance). Hence, the substrate likely plays an important role in the MCs' translational motion. Therefore, it is hypothesized that such a translational motion is caused by the nuAMF-induced persistent out-of-plane rotation of the MC near a wall (see Fig. 5-4).

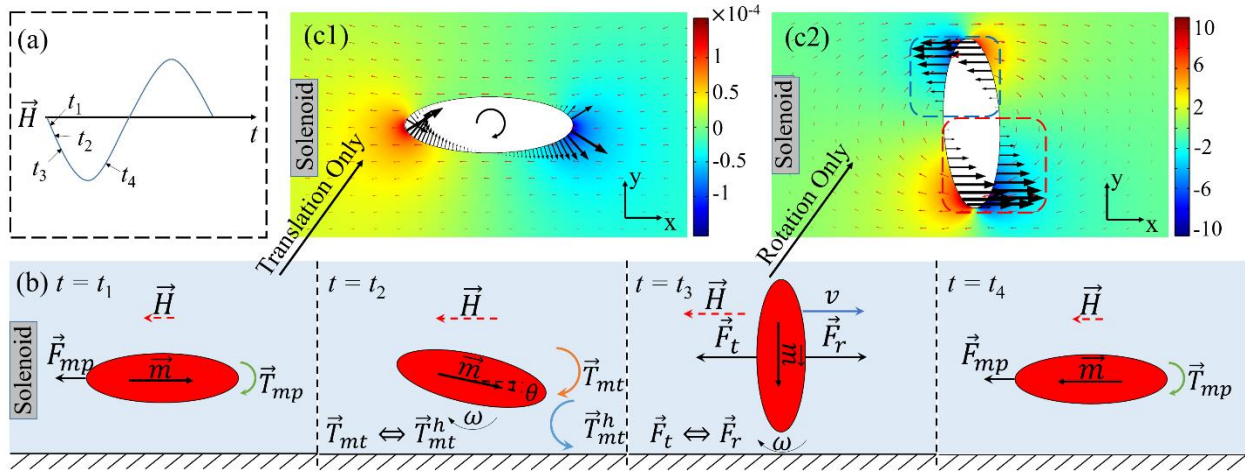


Figure 5-4. The translational and rotational motion of a magnetic cluster (MC) driven by low-frequency nuAMF. (a) External alternating H-field as a function of time. (b) Force and torque analysis of a MC in an AC H-field. (c1-2) Pressure distribution on the MC surface at $t = t_1$ and $t = t_3$ moments. Initially, the magnetic moment of the MC aligns with the external \mathbf{H} . By time instant t_1 , \mathbf{H} changes to the new orientation, which is opposite to its original orientation. The MC experiences a magnetophoresis force \mathbf{F}_{mp} pointing toward the solenoid. This \mathbf{F}_{mp} induces a weak hydrodynamic torque \mathbf{T}_{mp} on the MC, which drives it to rotate in the clockwise direction (see c1). Once the MC deviates from its original orientation, it experiences a magnetic torque \mathbf{T}_{mt} caused by \mathbf{H} , which further drives its clockwise rotation. Consequently, the MC shows persistent rotation and moves away from the solenoid ($t = t_3$ and c2) as a surface walker¹²⁸ until it fully aligns with the external magnetic field \mathbf{H} ($t = t_4$).

A key observation from the experiments is that most of the MCs rotate in the same direction during their out-of-plane rotation. Typically, to induce persistent out-of-plane rotation of a magnetic cluster or chain in one direction, a rotating H-field is required. Non-rotating uniform

alternating H-fields generally cannot independently induce persistent rotation in any direction. This is because once the MC becomes aligned with the external field, the magnetic torque exerted on it vanishes and the cluster maintains its orientation. When the alternating H-field reverts its direction, the MC can rotate either forward or backward depending on the thermal noise. However, the alternating magnetic field (non-rotating) used in the experiments is not uniform and has a non-zero gradient along its center axis. The symmetry of the rotation direction in an alternating H-field could be broken by the non-uniformity of the field and cause persistent out-of-plane rotation of the MCs. Such a persistent rotation can be induced jointly by the magnetic torque and the magnetophoresis force in a nuAMF. To simplify the problem, the MC is approximated as a rigid ellipsoid with a permanent magnetic moment \mathbf{m} . Figure 5-4a shows the strength of the nuAMF used in the experiments during one period of AC input. When the MC is placed in an external H-field, it experiences a magnetic torque,

$$\mathbf{T}_{\text{mt}} = \mu_0 \mathbf{m} \times \mathbf{H}, \quad (5-1)$$

where μ_0 is the magnetic permeability of vacuum. Driven by this torque, the cluster will rotate till \mathbf{m} is aligned with \mathbf{H} .^{128, 137, 189} As mentioned before, once the cluster is fully aligned with \mathbf{H} , \mathbf{T}_{mt} will become zero. At this very moment, the out-of-plane rotation is driven by the magnetophoresis force and the hydrodynamic interactions between the MC and substrate, as shown in Fig. 5-4b.

The magnetophoresis force \mathbf{F}_{mp} can be expressed as^{43, 57}

$$\mathbf{F}_{\text{mp}} = \frac{1}{2} \mu_0 \chi_m V_p \nabla |\mathbf{H}|^2, \quad (5-2)$$

where χ_m is the volume-averaged susceptibility. The direction of this magnetophoresis force is independent of the direction of the H-field and always points toward the solenoid as shown in Fig. 5-4b. Because of the small H-fields applied in the experiments, this force is so small that the

associated magnetophoresis velocity is at least an order of magnitude smaller than the translational velocity caused by the rotation. However, it can introduce a torque to rotate the MC through the hydrodynamic interactions between the MC and the substrate. As shown in Fig. 5-4c1, when the cluster moves toward the solenoid, the pressure on the left side is higher than that on the right side. This unbalanced pressure induces a clockwise net torque \mathbf{T}_{mp} on the cluster, thus forcing it to rotate in the clockwise direction. Hence, for an aligned cluster, when the H-field changes direction, the subtle magnetophoresis force effectively steers the cluster to rotate in the clockwise direction and outweighs the effect of thermal noise. As a result, the cluster exhibits a persistent out-of-plane clockwise rotation.

Once the cause of the MC's persistent out-of-plane rotation is understood, their translational motion can be analyzed as shown in Fig. 5-4b. When $t < 0$ s, the cluster is fully aligned with the external H-field. By the moment of $t = t_1$, the direction of the external nuAMF changes by 180° , but the magnetic torque \mathbf{T}_{mt} is close to zero. As explained above, steered by the magnetophoresis force \mathbf{F}_{mp} , the cluster slowly rotates in the clockwise direction. Once the cluster deviates from its original orientation ($t = t_2$), \mathbf{T}_{mt} increases dramatically. This \mathbf{T}_{mt} further drives the cluster to rotate in the clockwise direction, which tends to realign its \mathbf{m} with the external H . The hydrodynamic torque associated with this rotation (denoted by \mathbf{T}_{mt}^h) balances \mathbf{T}_{mt} and the cluster is torque-free overall. During this realigning rotation ($t = t_3$), the hydrodynamic interactions between cluster and substrate generate a force \mathbf{F}_r on the cluster due to the imbalance of the x -component of the pressure forces on the left and right portion of the MC's surface (see Fig. 5-4c2). This \mathbf{F}_r drives the MC to move away from the solenoid. The cluster's translational speed v is determined by the balance between the drag force \mathbf{F}_t (induced by the translational motion of the MC), and the force \mathbf{F}_r because the cluster is force-free overall. This translational motion of the cluster lasts until the

cluster becomes fully aligned with the external \mathbf{H} ($t = t_4$).

5.2.2 Numerical Simulations Setup

To validate the above hypothesis, numerical simulations are used to investigate the actuation of an ellipsoidal magnetic rod by a nuAMF in two-dimensional space. The simulation system features an ellipsoidal magnetic rod placed inside a 150 μm -thick and 400 μm -wide liquid, and 35 μm above a solid substrate surface (see Fig. 5-5 for a schematic). For the low-frequency situation, a rigid elliptical magnetic rod with a major radius R_a of 15 μm and a minor radius R_b of 5 μm is placed 35 μm above the substrate. Initially, the \mathbf{m} of the rod is aligned with \mathbf{H} , pointing in the positive x -direction, and the liquid around it is stationary. An external nuAMF is applied by a solenoid placed on the left-hand side with an input AC with the amplitude I_0 . The external magnetic field is generated by a solenoid with total coil number of $n = 550$, coil radius $R_s = 3$ cm, solenoid length $L_s = 15$ cm. The axis of the solenoid is 35 μm above the solid substrate. The magnetic rod is initially placed on the axis of the solenoid and its distance from the right end of the solenoid is 4.5 cm. The nuAMF generated by the solenoid along its axis is given by¹⁹⁰

$$\mathbf{H} = \frac{\mu_r n I_0 \sin(2\pi f_H t)}{2} \left[\frac{L_s/2 - x}{\sqrt{(x - L_s/2)^2 + R_s^2}} + \frac{L_s/2 + x}{\sqrt{(x + L_s/2)^2 + R_s^2}} \right], \quad (5-3)$$

where $\mu_r = 200$ is the relative permeability of the solenoid's iron core, I_0 is the input current. The magnetic torque and magnetophoresis force induced by the solenoid on the rod were computed using Equ. 5-1 and 5-2, respectively.

The flow field \mathbf{u} in the system is governed by the Stokes equation since the Reynolds number is small in the system,

$$\nabla \cdot \mathbf{u} = 0, \quad (5-4)$$

$$\eta \nabla^2 \mathbf{u} - \nabla p = 0, \quad (5-5)$$

where η is the viscosity of water and p is pressure. The air-liquid interface is treated as a slip wall, while the substrate is treated as a no-slip wall. The left and right boundaries of the system are set as stress-free open boundaries. As mentioned earlier, the rod exhibits both rotational and translational motions in a nuAMF. Applying the no-slip boundary condition on the rod's surface, the fluid velocity on the rod's surface is given by

$$\mathbf{u}(\mathbf{x}_s, t) = \mathbf{v} + \bar{\omega}_r \times (\mathbf{x}_s - \mathbf{x}_0), \quad (5-6)$$

where \mathbf{v} and $\bar{\omega}_r$ are translational and rotational velocity, \mathbf{x}_0 is the geometrical center of the rod, and \mathbf{x}_s is the position of any point on the rod's surface.

At $t < 0$ s, the rod is fully aligned with external magnetic field and the fluids are stationary. At $t = 0$ s, the external magnetic field changes direction and the rod starts to rotate in the clockwise direction under the effect of magnetophoresis (see Fig. 5-4(b1)). This rotation with an angular velocity $\bar{\omega}_r$ is then driven primarily by the magnetic torque \mathbf{T}_{mt} , which is balanced by the hydrodynamic torque associated with this rotation \mathbf{T}_{mt}^h

$$\mathbf{T}_{mt}^h = \int_{\Gamma} (\mathbf{x}_s - \mathbf{x}_0) \times (\boldsymbol{\sigma}_h \cdot \mathbf{n}) dS = -\mathbf{T}_{mt}, \quad (5-7)$$

where Γ represents the surface of the rod and $\boldsymbol{\sigma}_h$ is the hydrodynamic stress tensor. Hence, the rod is torque free overall. The rotation near a solid boundary (substrate) exerts a hydrodynamic force \mathbf{F}_r on the rod. This force is balanced by a hydrodynamic drag \mathbf{F}_t associated with the translational motion of the rod. Hence, the rod is force free overall,

$$\mathbf{F}_{tot} = \mathbf{F}_r + \mathbf{F}_t = \int_{\Gamma} \boldsymbol{\sigma}_h \cdot \mathbf{n} dS = 0. \quad (5-8)$$

To solve Equ. 5-(1-8) simultaneously and predict the behavior of the magnetic rod, a commercial finite element package COMSOL was used.¹⁴⁴ Both the torque and force free conditions are ensured by iterating the $\bar{\omega}$ and v at each time step until Equ. 5-7 and 5-8 are satisfied. Then the position of the magnetic rod and mesh are updated with velocities obtained using arbitrary Lagrangian-Eulerian (ALE) method.^{145, 191}

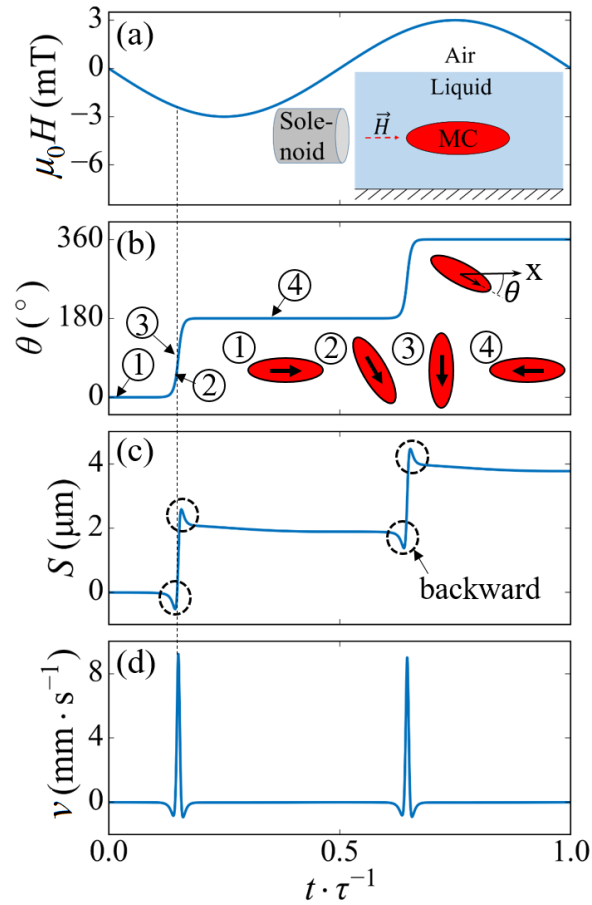


Figure 5-5. Simulation results of the motion of a magnetic cluster in one period of low-frequency nuAMF. (a) The external nuAMF. (b) The angle between the cluster's magnetic moment and the horizontal plane. (c) The cluster's displacement. (d) The cluster's translational velocity.

The computational domain was discretized using triangular elements, and the mesh is locally refined near the magnetic rod surface to ensure computing accuracy of the torque and force.

Multiple remeshing processes were performed to maintain the mesh quality. Mesh studies had been done to ensure that the results were independent of the mesh size.

5.2.3 Simulation Results and Analysis

Figure 5-5 shows the simulation results of cluster motion in one period of a nuAMF with $f_H = 20$ Hz and $I_0 = 2$ A. In one AC period τ (0.05 s), the MC rotates 360° in a clockwise direction to realign itself with \mathbf{H} . Figure 5-5b shows the orientation of the rod as a function of the rotation time (the orientation angle θ is defined in Fig. 5-5b). The rod shows two sharp angular changes in the clockwise direction near $t = 0.15\tau$ and 0.65τ , each corresponding to a rotation of the rod by 180° to realign with the magnetic field \mathbf{H} . Note the duration of these rotations of the rod is short compared to the period of nuAMF \mathbf{H} . Figure 5-5c shows the x -direction displacement S of the rod from its original position during one period of nuAMF. The increase/decrease of S means the rod moves away/toward the solenoid. It is interesting to note that S only changes when θ changes, i.e., the rod translates only when it rotates. During each clockwise rotation of the rod, the rod generally moves away from the solenoid (a sharp increase of S) due to the hydrodynamic interaction between the rod and the substrate. Such rotation-depended translation of the rod exhibits a fluctuation in S with a $2f_H$ frequency similar to the experimental observation.

It is interesting to note that the rod moves toward the solenoid with a small back step (see the decrease of S near $t = 0.15\tau$ and 0.65τ) at the beginning and end of each rotation process. Such a weak backward movement is caused by the imbalance of the pressure distribution on the rod's surface. This $2f_H$ translational movement of the rod also generates two spikes of translational velocity v in one period τ , as shown in Fig. 5-5d.

Figure 5-6 shows the width W of the rod projected on the horizontal plane as predicted by the

simulation and measured experimentally. Both results from simulation and experiment show two sharp downward spikes in one period of nuAMF, each corresponding to one 180° out-of-plane rotation of the rod. In contrast, when the rod is aligned with \mathbf{H} its projected width remains close to the major diameter of the rod, similar to the observation from experiments (see Fig. 5-6b).

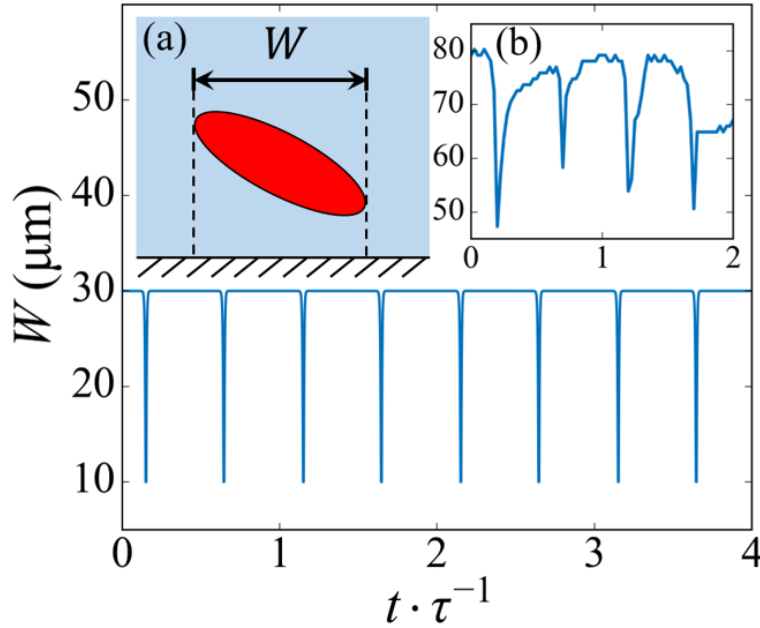


Figure 5-6. Evolution of the width of a magnetic cluster projected onto the horizontal plane over several periods of AC magnetic field ($f_H = 5$ Hz or $\tau = 0.2$ s). Inset (a) show the definition of the projected width of the cluster. Inset (b) is the representative experimental result compared with simulation data. The two downward spikes correspond to the rapid alignment of the cluster with the external magnetic field once it rotates away from the 0° or 180° orientation (see Fig. 5-5b). The projected width maintains its maximal value most of the time, indicating that the cluster is fully aligned with the low-frequency magnetic field studied here.

The effects of current amplitude I_0 and field frequency f_H on the average translational speed v of the magnetic rod have also been studied. The simulation results of the translational speed v for different I_0 show a similar trend as the experimental observation (see Fig. 5-2). Figure 5-7a shows that, when I_0 is small ($I_0 \leq 0.5$ A), the rod exhibits no translational motion. This is because \mathbf{H} ,

and hence \mathbf{F}_{mp} , generated by the current is too weak to ensure that the rod keeps rotating in the same direction when the direction of the magnetic field changes. Once I_0 is large enough ($I_0 >$

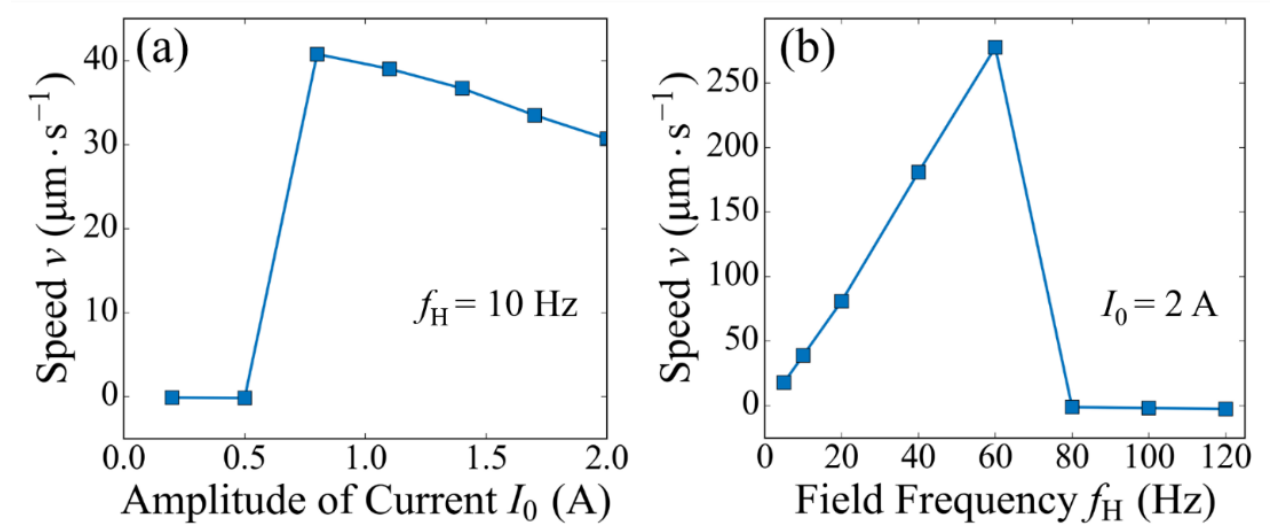


Figure 5-7. Effects of the amplitude of current I_0 (a) and field frequency f_H (b) of nuAMF on the translational velocity obtained from simulations.

0.5A), the rod starts to exhibit a persistent out-of-plane rotation and translates away from the solenoid. As the I_0 increases further, v decreases slightly due to the increase of \mathbf{F}_{mp} , which tends to drive the rod toward the solenoid. As shown in Fig. 5-7b, the translational speed v of the rod increases linearly in the low to intermediate frequency regime ($0 \text{ Hz} < f_H < 60 \text{ Hz}$). Such a rapid raise of v is expected as higher f_H means more out-of-plane rotations of a cluster in the same time period. When f_H is too high, the translational motion of the cluster becomes weak, similar to the experimental observation (see Fig. 5-3). This can be understood as follows. In a nuAMF \mathbf{H} with a sufficiently high frequency ($f_H \geq 80 \text{ Hz}$), the period of the nuAMF \mathbf{H} is too short for the cluster to realign itself with the H-field. Specifically, before the cluster rotates 180° in a clockwise direction, it is forced to rotate back (counter-clockwise) toward its original orientation by the changing direction of \mathbf{H} . Hence, the cluster can no longer persistently rotate in one direction and

its net translational motion is eliminated.

5.3 Conclusions

In summary, a novel method to manipulate magnetic clusters near a solid surface using a nuAMF is analyzed and the dynamics of magnetic clusters is studied. Experiments show that MCs will move away from the solenoid, which is different from the case of a magnetic particle pulling a permeant magnet. It is found that the MCs' time-dependent displacements show periodic behaviors and the frequency of the fluctuation of the particle displacement is twice the frequency of the driving field. The moving speed of the MCs also depends on the strength and gradient of the driving H-field, the frequency of the driving H-field, and the size of the MCs. A hydrodynamic model is developed to understand the underlying mechanisms of the MCs' behaviors and the theoretical predictions match the experimental results quite well. It is found that this nuAMF induced the persistent out-of-plate rotation of MCs by the effects of magnetophoresis and magnetic torque. This out-of-plate rotation of MCs causes the translational motion through the hydrodynamic interactions between MCs and a nearby solid boundary. This directional manipulation method has advantages when compared to other manipulation methods. For example, it is easy and cheap to implement and requires much weaker H-field strength than traditional magnetic field manipulation methods. Such a simple particle manipulation method has a great potential in applications such as cell biology and microfluidics.

Chapter 6. Summary

Micro-particles are ubiquitous in microsystems related to biology, medicine and microfluidics. The effective manipulation of micro-particles is crucial for achieving the desired functionality of microsystems and requires a fundamental understanding their dynamics in complex environment. In the past decades, many micro-particle manipulation methods have been developed basing on different particle dynamics induced by electric and magnetic fields, acoustic waves, and optical forces, *etc.* Nonetheless, few manipulation methods are suitable for *in vivo* applications. Hence, new methods are still being explored and developed at present. Among them, the active particles and magnetically steered surface walkers show great potentials in the practical manipulation of micro-particles. However, the underlying mechanisms of these new methods are still not well understood, and questions remain on the dynamics of the micro-particles in complex environment. To significantly improve the performance of these new technologies, these questions must be addressed. The overall objective of this dissertation is to advance the fundamental understanding of the dynamics of two types of micro-particles (specifically active particles and magnetically steered surface walkers) to facilitate their further development. For active particles, the self-diffusiophoresis of Janus catalytic micromotors in confined geometries and the bubble behavior in active particle system are investigated. For magnetically steered surface walkers, a novel manipulation method is presented and the dynamics of magnetic particles during manipulation process is analyzed.

In Chapter 2, the translational and rotational dynamics of JCMs in confined geometries driven by self-diffusiophoresis are studied using direct numerical simulations. The simulations reveal that JCMs can exhibit rich dynamic behavior under confined conditions. For the translocation of a single spherical JCM through a short cylindrical pore, while the JCM is slowed down by the pore

on average, the speed of the JCM can exceed that in free solutions when the JCM approaches the pore exit. The overall slowdown of self-diffusiophoresis becomes more obvious when the pore size reduces, but its dependence on the pore size is much weaker than the transport of particles driven by external force or externally imposed concentration gradients. For the translocation of a pair of JCMs through a pore, when both of their catalytic surfaces are facing the bottom reservoir direction, the front JCM speedups but the back JCM slows down. For a circular JCM near a pore entrance and with its phoretic axis not aligned with the pore axis, the JCM can enter the pore and its phoretic axis becomes fully aligned with the pore axis if its initial inclination angle is small. Otherwise, the JCM either collides with the pore entrance or moves away into the reservoir. For a JCM already inside a pore, self-diffusiophoresis can align the JCM's phoretic axis with the pore axis and drive it toward the pore center for the parameters considered here. These rich behaviors have both hydrodynamic and chemical origins. In particular, the modification of the chemical species concentrations surrounding a JCM by wall confinement and its neighboring JCMs, which is called a "chemical effect" (diffusion of the products), plays a key role in determining the translation and rotation of the JCMs. These effects are especially significant when the confinement is severe or when JCMs approach each other and should be taken into account in the design and operation of JCMs in these applications.

In Chapter 3, a new collective motion behavior of JCMs accompanied by periodic bubbling is analyzed. While an individual 5- μm diameter JCM submerged in solution cannot nucleate a bubble independently, it is found that at high JCM density, JCMs aggregate locally and collectively enable the nucleation and growth of bubbles. As the bubble grows, the JCMs exhibit a collective, synchronized motion. This motion is fast and its direction is towards the center of the bubble, regardless of the orientation of the catalytic surface on the JCMs. With the help of scale analysis,

it is proposed that the motion of JCMs towards the bubble center is caused by the evaporation-induced Marangoni flow effects. The numerical simulations show that the Marangoni effect can produce similar speeds of JCMs as observed in the experiments. Such an evaporation-induced Marangoni effect is further supported by experiments in which environmental humidity is tuned to quench the collective motion of JCMs. This result could be expected to garner interest for collective task management with fewer size restrictions as far as bubble nucleation is concerned.

In Chapter 4, some of the peculiar behaviors related to the formation, growth, and collapse of bubbles in JCM systems reported in recent experiments are investigated. A criterion is derived for the formation of bubbles on a JCM's surface based on consideration of the mass transfer near the JCM and the thermodynamics of bubble nucleation. Using this criterion, it is shown that bubble formation is controlled by both JCM size and the catalytic activity of the JCM's surface. According to the simulation, a high concentration profile generated by a cluster of JCMs facilitates the formation of bubbles, even near small JCMs. The numerical simulation on the growth of a bubble fed by a ring of JCMs produces an anomalous growth law of $R_b \sim t^\eta$ where η is larger than 0.5 and depends on the number of JCMs in the ring and the inward velocity of the JCM toward the bubble. This unusual bubble growth behavior is caused by a combination of a supersaturation environment and the relative movement between the growing bubble and the JCM. It is suggested that the rapid bubble collapse observed in recent experiments is due to the coalescence of the bubble with the air-liquid interface. The hypothesis is supported by agreement between the short time scale of such coalescence observed in experiments and in the simulations.

In Chapter 5, a novel method to manipulate magnetic clusters (MCs) near a solid surface using a nuAMF is analyzed and the dynamics of the magnetic clusters is studied. Experiments show that MCs move away from the solenoid, which is different from the case of a magnetic particle being

pulled by a permanent magnet. The speed of motion of the MCs also depends on the strength and gradient of the driving H-field, the frequency of the driving H-field, and the size of the MCs. A hydrodynamic model is developed to understand the mechanisms of the MCs' behaviors and the theoretical predictions match the experimental results quite well. It is found that the combination of magnetophoresis force and the magnetic torque cause the persistent rotation of the MCs. This rotational motion leads to translational motion due to the hydrodynamic interaction between the rotating MCs and a nearby substrate. Such a simple particle manipulation method has great potential for applications such as those in cell biology and microfluidics.

Reference

1. Feynman, R. P. There's plenty of room at the bottom. *Engineering and science* **1960**, *23*, 22-36.
2. Iamsaard, S., et al. Conversion of light into macroscopic helical motion. *Nat Chem* **2014**, *6*, 229-235.
3. Kuo, J. *Electron microscopy : methods and protocols*; Third edition. ed.; Humana Press: New York, 2014. p 799.
4. Bhushan, B., et al. *Handbook of Nanomaterials Properties*; Springer Verlag: Heidelberg, 2014. p 1463.
5. Bruce, D. W., et al. *Multi length-scale characterisation*; Wiley: Chichester, West Sussex, 2014. p 294.
6. Gerrard, J. A. *Protein nanotechnology : protocols, instrumentation, and applications*; 2nd edition. ed.; Humana Press : Springer: New York, 2013. p 371.
7. Castillo-León, J., et al. *Micro and nano techniques for the handling of biological samples*; CRC Press: Boca Raton, FL, 2012. p 231.
8. Huang, Q. *Nanotechnology in the food, beverage and nutraceutical industries*; Woodhead Publishing Ltd: Cambridge ; Philadelphia, 2012. p 452.
9. Totten, G. E.; Liang, H. *Mechanical tribology : materials, characterization, and applications*; Marcel Dekker: New York, 2004. p 496.
10. Hochella, M. F. There's plenty of room at the bottom: Nanoscience in geochemistry. *Geochim Cosmochim Ac* **2002**, *66*, 735-743.
11. Schaller, R. R. Moore's Law: Past, present, and future. *Ieee Spectrum* **1997**, *34*, 52-59.
12. Trimmer, W. S. N. Microrobots and Micromechanical Systems. *Sensor Actuator* **1989**, *19*, 267-287.
13. Dong, L. X.; Nelson, B. J. Robotics in the small - Part II: Nanorobotics. *Ieee Robot Autom Mag* **2007**, *14*, 111-121.
14. Abbott, J. J., et al. Robotics in the small - Part I: microrobotics. *Ieee Robot Autom Mag* **2007**, *14*, 92-103.
15. Yokel, R. A.; Macphail, R. C. Engineered nanomaterials: exposures, hazards, and risk prevention. *J Occup Med Toxicol* **2011**, *6*, 7.

16. Sader, J. E., et al. General scaling law for stiffness measurement of small bodies with applications to the atomic force microscope. *J Appl Phys* **2005**, *97*, 124903.
17. Wautelet, M. Scaling laws in the macro-, micro- and nanoworlds. *Eur J Phys* **2001**, *22*, 601-611.
18. Reifenberger, R. G. *Fundamentals of atomic force microscopy*; World Scientific: Hackensack New Jersey, 2016. p 323.
19. Eaton, P. J.; West, P. *Atomic force microscopy*; Oxford University Press: Oxford ; New York, 2010. p 248.
20. Binnig, G., et al. Atomic Force Microscope. *Phys Rev Lett* **1986**, *56*, 930-933.
21. Seruca, R., et al. *Fluorescence imaging and biological quantification*; Taylor & Francis: Boca Raton, 2017. p 360.
22. Serdyuk, I. N., et al. *Methods in molecular biophysics : structure, dynamics, function*; Second edition. ed.; Cambridge University Press: Cambridge, United Kingdom ; New York, NY, USA, 2017. p 1136.
23. Yablon, D. G. *Scanning probe microscopy for industrial applications : nanomechanical characterization*; Wileys: Hoboken, New Jersey, 2014. p 347.
24. Taatjes, D. J.; Roth, J. *Cell imaging techniques : methods and protocols*; 2nd ed.; Humana Press: New York, 2013. p 550.
25. Goldman, R. D., et al. *Live cell imaging : a laboratory manual*; 2nd ed.; Cold Spring Harbor Laboratory Press: Cold Spring Harbor, N.Y., 2010. p 736.
26. Borisenko, V. E.; Ossicini, S. *What is what in the nanoworld : a handbook on nanoscience and nanotechnology*; 3rd, revised and enlarged edition. ed.; Wiley-VCH: Weinheim, Germany, 2012. p 601.
27. Junno, T., et al. Controlled Manipulation of Nanoparticles with an Atomic-Force Microscope. *Appl Phys Lett* **1995**, *66*, 3627-3629.
28. Martinez, R. V., et al. Silicon nanowire circuits fabricated by AFM oxidation nanolithography. *Nanotechnology* **2010**, *21*, 245301.
29. Pedrak, R., et al. Micromachined atomic force microscopy sensor with integrated piezoresistive, sensor and thermal bimorph actuator for high-speed tapping-mode atomic force microscopy phase-imaging in higher eigenmodes. *J Vac Sci Technol B* **2003**, *21*, 3102-3107.
30. Kinbara, K.; Aida, T. Toward intelligent molecular machines: Directed motions of biological and artificial molecules and assemblies. *Chem Rev* **2005**, *105*, 1377-1400.

31. Browne, W. R.; Feringa, B. L. Making molecular machines work. *Nat Nanotechnol* **2006**, *1*, 25-35.
32. Balzani, V., et al. Artificial molecular machines. *Angew Chem, Int Ed* **2000**, *39*, 3349-3391.
33. Miller, J. Chemistry Nobel honors mechanical bonds, molecular machines. *Phys Today* **2016**, *69*, 18-21.
34. Ballardini, R., et al. Artificial molecular-level machines: Which energy to make them work? *Accounts Chem Res* **2001**, *34*, 445-455.
35. Berna, J., et al. Macroscopic transport by synthetic molecular machines. *Nat Mater* **2005**, *4*, 704-710.
36. Badilescu, S.; Packirisamy, M. *BioMEMS : science and engineering perspectives*; CRC Press: Boca Raton, 2011. p 329.
37. Whitesides, G. M. The origins and the future of microfluidics. *Nature* **2006**, *442*, 368-373.
38. Karimi, A., et al. Hydrodynamic mechanisms of cell and particle trapping in microfluidics. *Biomicrofluidics* **2013**, *7*, 21501.
39. Li, M., et al. A review of microfabrication techniques and dielectrophoretic microdevices for particle manipulation and separation. *J Phys D Appl Phys* **2014**, *47*, 063001.
40. Li, Y. H., et al. Manipulations of vibrating micro magnetic particle chains. *J Appl Phys* **2012**, *111*, 07A924.
41. Vavassori, P., et al. Magnetic nanostructures for the manipulation of individual nanoscale particles in liquid environments. *J Appl Phys* **2010**, *107*, 09B301.
42. Floyd, S., et al. Microparticle Manipulation using Multiple Untethered Magnetic Micro-Robots on an Electrostatic Surface. *2009 Ieee-Rsj International Conference on Intelligent Robots and Systems* **2009**, 528-533.
43. Kirby, B. J. *Micro- and nanoscale fluid mechanics : transport in microfluidic devices*; Cambridge University Press: New York, 2010. p 512.
44. Keh, H. J.; Chiou, J. Y. Electrophoresis of a Colloidal Sphere in a Circular Cylindrical Pore. *AIChE J* **1996**, *42*, 1397-1406.
45. Keh, H. J.; Chen, S. B. Electrophoresis of a Colloidal Sphere Parallel to a Dielectric Plane. *J Fluid Mech* **1988**, *194*, 377-390.
46. Bousse, L., et al. Electrokinetically controlled microfluidic analysis systems. *Annu Rev Bioph Biom* **2000**, *29*, 155-181.

47. Pohl, H. A. The Motion and Precipitation of Suspensoids in Divergent Electric Fields. *J Appl Phys* **1951**, *22*, 869-871.
48. Jones, T. B. Electrostatics and the lab on a chip. *Inst Phys Conf Ser* **2004**, 1-10.
49. Fiedler, S., et al. Dielectrophoretic sorting of particles and cells in a microsystem. *Anal Chem* **1998**, *70*, 1909-1915.
50. Cui, H. H., et al. Separation of particles by pulsed dielectrophoresis. *Lab Chip* **2009**, *9*, 2306-2312.
51. Gascoyne, P. R. C.; Vykoukal, J. Particle separation by dielectrophoresis. *Electrophoresis* **2002**, *23*, 1973-1983.
52. Zhang, C., et al. Dielectrophoresis for manipulation of micro/nano particles in microfluidic systems. *Anal Bioanal Chem* **2010**, *396*, 401-420.
53. Voldman, J., et al. Holding forces of single-particle dielectrophoretic traps. *Biophys J* **2001**, *80*, 531-541.
54. Archer, S., et al. Cell reactions to dielectrophoretic manipulation. *Biochem Biophys Res Commun* **1999**, *257*, 687-698.
55. Gonzalez, A., et al. Fluid flow induced by nonuniform ac electric fields in electrolytes on microelectrodes. II. A linear double-layer analysis. *Phys Rev E* **2000**, *61*, 4019-4028.
56. Erb, R. M., et al. Actuating Soft Matter with Magnetic Torque. *Adv Funct Mater* **2016**, *26*, 3859-3880.
57. Khashan, S. A.; Furlani, E. P. Effects of particle-fluid coupling on particle transport and capture in a magnetophoretic microsystem. *Microfluid Nanofluid* **2012**, *12*, 565-580.
58. Pamme, N.; Manz, A. On-chip free-flow magnetophoresis: Continuous flow separation of magnetic particles and agglomerates. *Anal Chem* **2004**, *76*, 7250-7256.
59. Scherer, F., et al. Magnetofection: enhancing and targeting gene delivery by magnetic force in vitro and in vivo. *Gene Ther* **2002**, *9*, 102-109.
60. Lubbe, A. S., et al. Clinical applications of magnetic drug targeting. *J Surg Res* **2001**, *95*, 200-206.
61. Zhu, X. B.; Grutter, P. Imaging, manipulation, and spectroscopic measurements of nanomagnets by magnetic force microscopy. *Mrs Bull* **2004**, *29*, 457-462.
62. Vieira, G., et al. Transport of magnetic microparticles via tunable stationary magnetic traps in patterned wires. *Physical Review B* **2012**, *85*, 174440.

63. Sarella, A., et al. Two-Dimensional Programmable Manipulation of Magnetic Nanoparticles on-Chip. *Advanced Materials* **2014**, *26*, 2384-2390.
64. Laurell, T., et al. Chip integrated strategies for acoustic separation and manipulation of cells and particles. *Chem Soc Rev* **2007**, *36*, 492-506.
65. Doinikov, A. A. Acoustic Radiation Pressure on a Compressible Sphere in a Viscous-Fluid. *J Fluid Mech* **1994**, *267*, 1-21.
66. Alekseev, V. N. Force Produced by the Acoustic Radiation Pressure on a Sphere. *Sov Phys Acoust+* **1983**, *29*, 77-81.
67. Nyborg, W. L. Radiation Pressure on a Small Rigid Sphere. *J Acoust Soc Am* **1967**, *42*, 947.
68. Wang, Z. C.; Zhe, J. A. Recent advances in particle and droplet manipulation for lab-on-a-chip devices based on surface acoustic waves. *Lab Chip* **2011**, *11*, 1280-1285.
69. Shi, J. J., et al. Focusing microparticles in a microfluidic channel with standing surface acoustic waves (SSAW). *Lab Chip* **2008**, *8*, 221-223.
70. Wood, C. D., et al. Alignment of particles in microfluidic systems using standing surface acoustic waves. *Appl Phys Lett* **2008**, *92*, 044104.
71. Franke, T., et al. Surface acoustic wave (SAW) directed droplet flow in microfluidics for PDMS devices. *Lab Chip* **2009**, *9*, 2625-2627.
72. Yasuda, K., et al. Using acoustic radiation force as a concentration method for erythrocytes. *J Acoust Soc Am* **1997**, *102*, 642-645.
73. Shi, J. J., et al. Acoustic tweezers: patterning cells and microparticles using standing surface acoustic waves (SSAW). *Lab Chip* **2009**, *9*, 2890-2895.
74. Lenshof, A., et al. Acoustofluidics 8: Applications of acoustophoresis in continuous flow microsystems. *Lab Chip* **2012**, *12*, 1210-1223.
75. Jonas, A.; Zemanek, P. Light at work: The use of optical forces for particle manipulation, sorting, and analysis. *Electrophoresis* **2008**, *29*, 4813-4851.
76. Ashkin, A. Acceleration and Trapping of Particles by Radiation Pressure. *Phys Rev Lett* **1970**, *24*, 156.
77. Ashkin, A.; Dziedzic, J. M. Optical Levitation by Radiation Pressure. *Appl Phys Lett* **1971**, *19*, 283.

78. Ashkin, A. Optical trapping and manipulation of neutral particles using lasers. *P Natl Acad Sci USA* **1997**, *94*, 4853-4860.
79. Gaugiran, S., et al. Polarization and particle size dependence of radiative forces on small metallic particles in evanescent optical fields. Evidences for either repulsive or attractive gradient forces. *Opt Express* **2007**, *15*, 8146-8156.
80. Ng, L. N., et al. Manipulation of colloidal gold nanoparticles in the evanescent field of a channel waveguide. *Appl Phys Lett* **2000**, *76*, 1993-1995.
81. Schmidt, H.; Hawkins, A. R. Optofluidic waveguides: I. Concepts and implementations. *Microfluid Nanofluid* **2008**, *4*, 3-16.
82. Ashkin, A.; Dziedzic, J. M. Observation of Light-Scattering from Nonspherical Particles Using Optical Levitation. *Appl Optics* **1980**, *19*, 660-668.
83. Roosen, G. Optical Levitation of Spheres. *Can J Phys* **1979**, *57*, 1260-1279.
84. Dreyfus, R., et al. Microscopic artificial swimmers. *Nature* **2005**, *437*, 862-865.
85. Zhang, L., et al. Artificial bacterial flagella for micromanipulation. *Lab Chip* **2010**, *10*, 2203-2215.
86. Manjare, M., et al. Bubble Driven Quasioscillatory Translational Motion of Catalytic Micromotors. *Phys Rev Lett* **2012**, *109*, 128305.
87. Ismagilov, R. F., et al. Autonomous Movement and Self-Assembly. *Angew. Chem., Int. Ed.* **2002**, *41*, 652-654.
88. Paxton, W. F., et al. Catalytic Nanomotors: Autonomous Movement of Striped Nanorods. *J. Am. Chem. Soc.* **2004**, *126*, 13424-13431.
89. Kapral, R. Perspective: Nanomotors without Moving Parts That Propel Phemselves in Solution. *J. Chem. Phys.* **2013**, *138*, 020901.
90. Ebbens, S. J.; Howse, J. R. In Pursuit of Propulsion at the Nanoscale. *Soft Matter* **2010**, *6*, 726-738.
91. Kolmakov, G. V., et al. Designing Self-Propelled Microcapsules for Pick-up and Delivery of Microscopic Cargo. *Soft Matter* **2011**, *7*, 3168-3176.
92. Baraban, L., et al. Transport of Cargo by Catalytic Janus Micro-Motors. *Soft Matter* **2012**, *8*, 48-52.
93. Fukuyama, T., et al. Directing and Boosting of Cell Migration by the Entropic Force Gradient in Polymer Solution. *Langmuir* **2015**, *31*, 12567-12572.

94. Zhang, Z., et al. Design a Plasmonic Micromotor for Enhanced Photo-Remediation of Polluted Anaerobic Stagnant Waters. *Chem Commun* **2016**, 52, 5550-5553.
95. Mou, F., et al. Autonomous Motion and Temperature-Controlled Drug Delivery of Mg/Pt-Poly (N-Isopropylacrylamide) Janus Micromotors Driven by Simulated Body Fluid and Blood Plasma. *ACS Appl Mater Interfaces* **2014**, 6, 9897-9903.
96. Howse, J. R., et al. Self-Motile Colloidal Particles: From Directed Propulsion to Random Walk. *Phys Rev Lett* **2007**, 99, 048102.
97. Anderson, J. L. Colloid Transport by Interfacial Forces. *Annu Rev Fluid Mech* **1989**, 21, 61-99.
98. Moran, J. L.; Posner, J. D. Locomotion of Electrocatalytic Nanomotors Due to Reaction Induced Charge Autoelectrophoresis. *Phys Rev E* **2010**, 81, 065302.
99. Solovey, A. A., et al. Catalytic Microtubular Jet Engines Self-Propelled by Accumulated Gas Bubbles. *Small* **2009**, 5, 1688-1692.
100. Gao, W., et al. Hydrogen-Bubble-Propelled Zinc-Based Microrockets in Strongly Acidic Media. *J Am Chem Soc* **2012**, 134, 897-900.
101. Manjare, M. T., et al. Marangoni Flow Induced Collective Motion of Catalytic Micromotors. *J. Phys. Chem. C* **2015**, 119, 28361-28367.
102. Reigh, S. Y.; Kapral, R. Catalytic Dimer Nanomotors: Continuum Theory and Microscopic Dynamics. *Soft Matter* **2015**, 11, 3149-3158.
103. Gao, Y.; Yu, Y. Macrophage Uptake of Janus Particles Depends upon Janus Balance. *Langmuir* **2015**, 31, 2833-2838.
104. Brown, A.; Poon, W. Ionic Effects in Self-Propelled Pt-Coated Janus Swimmers. *Soft Matter* **2014**, 10, 4016-4027.
105. Moran, J. L.; Posner, J. D. Role of Solution Conductivity in Reaction Induced Charge Auto-Electrophoresis. *Phys Fluids* **2014**, 26, 42001.
106. Popescu, M. N., et al. Confinement Effects on Diffusiophoretic Self-Propellers. *J Chem Phys* **2009**, 130, 194702.
107. Tao, Y. G.; Kapral, R. Swimming Upstream: Self-Propelled Nanodimer Motors in a Flow. *Soft Matter* **2010**, 6, 756-761.
108. Yang, M. C., et al. Hydrodynamic Simulations of Self-Phoretic Microswimmers. *Soft Matter* **2014**, 10, 6208-6218.

109. Uspal, W., et al. Self-Propulsion of a Catalytically Active Particle near a Planar Wall: From Reflection to Sliding and Hovering. *Soft Matter* **2015**, *11*, 434-438.
110. Ibrahim, Y.; Liverpool, T. B. The Dynamics of a Self-Phoretic Janus Swimmer Near a Wall. *Europhys Lett* **2015**, *111*, 48008.
111. Kreuter, C., et al. Transport Phenomena and Dynamics of Externally and Self-Propelled Colloids in Confined Geometry. *Eur. Phys. J.: Spec. Top.* **2013**, *222*, 2923-2939.
112. Mozaffari, A., et al. Self-Diffusiophoretic Colloidal Propulsion Near a Solid Boundary. *arXiv preprint arXiv:1505.07172* **2015**.
113. Das, S., et al. Boundaries Can Steer Active Janus Spheres. *Nat Commun* **2015**, *6*, 8999.
114. Michelin, S.; Lauga, E. Phoretic Self-Propulsion at Finite Péclet Numbers. *J Fluid Mech* **2014**, *747*, 572-604.
115. Golestanian, R., et al. Designing Phoretic Micro- and Nano-Swimmers. *New J Phys* **2007**, *9*, 126.
116. Wang, S.; Wu, N. Selecting the swimming mechanisms of colloidal particles: bubble propulsion versus self-diffusiophoresis. *Langmuir* **2014**, *30*, 3477-3486.
117. Huang, W. J., et al. Catalytic Nanoshell Micromotors. *J Phys Chem C* **2013**, *117*, 21590-21596.
118. Gibbs, J. G.; Zhao, Y.-P. Autonomously Motile Catalytic Nanomotors by Bubble Propulsion. *Appl Phys Lett* **2009**, *94*, 163104.
119. Mou, F., et al. Single-Component TiO₂ Tubular Microengines with Motion Controlled by Light-Induced Bubbles. *Small* **2015**, *11*, 2564-70.
120. Soler, L., et al. Self-propelled micromotors for cleaning polluted water. *ACS nano* **2013**, *7*, 9611-9620.
121. Brandon, N. P.; Kelsall, G. H. Growth-Kinetics of Bubbles Electrogenerated at Microelectrodes. *J Appl Electrochem* **1985**, *15*, 475-484.
122. Plesset, M. S.; Prosperetti, A. Bubble dynamics and cavitation. *Annu Rev Fluid Mech* **1977**, *9*, 145-185.
123. Enriquez, O. R., et al. The quasi-static growth of CO₂ bubbles. *J Fluid Mech* **2014**, *741*, R1.
124. Buehl, W. M.; Westwater, J. W. Bubble Growth by Dissolution - Influence of Contact Angle. *AIChE J* **1966**, *12*, 571-576.

125. Jones, S., et al. Bubble nucleation from gas cavities—a review. *Adv Colloid Interface Sci* **1999**, *80*, 27-50.
126. Epstein, P. S.; Plesset, M. S. On the Stability of Gas Bubbles in Liquid-Gas Solutions. *J Chem Phys* **1950**, *18*, 1505-1509.
127. Abbott, J. J., et al. Modeling magnetic torque and force for controlled manipulation of soft-magnetic bodies. *Ieee T Robot* **2007**, *23*, 1247-1252.
128. Sing, C. E., et al. Controlled surface-induced flows from the motion of self-assembled colloidal walkers. *P Natl Acad Sci USA* **2010**, *107*, 535-540.
129. Franceschini, A., et al. Dynamics of non-Brownian fiber suspensions under periodic shear. *Soft Matter* **2014**, *10*, 6722-6731.
130. Franceschini, A., et al. Transverse Alignment of Fibers in a Periodically Sheared Suspension: An Absorbing Phase Transition with a Slowly Varying Control Parameter. *Phys Rev Lett* **2011**, *107*, 250603.
131. Jenness, N. J., et al. Magnetic and optical manipulation of spherical metal-coated Janus particles. *SPIE Proceedings* **2010**, *7762*, 27
132. Zhang, L., et al. Controlled Propulsion and Cargo Transport of Rotating Nickel Nanowires near a Patterned Solid Surface. *Acs Nano* **2010**, *4*, 6228-6234.
133. Cheang, U. K., et al. Fabrication and magnetic control of bacteria-inspired robotic microswimmers. *Appl Phys Lett* **2010**, *97*, 213704.
134. Martinez-Pedrero, F.; Tierno, P. Magnetic Propulsion of Self-Assembled Colloidal Carpets: Efficient Cargo Transport via a Conveyor-Belt Effect. *Phys Rev Appl* **2015**, *3*, 051003.
135. Peyer, K. E., et al. Bio-inspired magnetic swimming microrobots for biomedical applications. *Nanoscale* **2013**, *5*, 1259-1272.
136. Erb, R. M., et al. Non-linear alignment dynamics in suspensions of platelets under rotating magnetic fields. *Soft Matter* **2012**, *8*, 7604-7609.
137. Kang, T. G., et al. Chaotic mixing induced by a magnetic chain in a rotating magnetic field. *Phys Rev E* **2007**, *76*, 066303.
138. Yang, F. C., et al. Self-Diffusiophoresis of Janus Catalytic Micromotors in Confined Geometries. *Langmuir* **2016**, *32*, 5580-5592.
139. Gao, W., et al. Catalytic Iridium-Based Janus Micromotors Powered by Ultralow Levels of Chemical Fuels. *J Am Chem Soc* **2014**, *136*, 2276-2279.

140. Ibele, M., et al. Schooling Behavior of Light - Powered Autonomous Micromotors in Water. *Angew Chem, Int Ed* **2009**, *48*, 3308-3312.
141. Ai, Y., et al. Transient Electrophoretic Motion of a Charged Particle Through a Converging - Diverging Microchannel: Effect of Direct Current - Dielectrophoretic Force. *Electrophoresis* **2009**, *30*, 2499-2506.
142. Ai, Y., et al. DC Electrokinetic Particle Transport in an L-Shaped Microchannel. *Langmuir* **2009**, *26*, 2937-2944.
143. Ai, Y., et al. Direct Numerical Simulation of AC Dielectrophoretic Particle-Particle Interactive Motions. *J Colloid Interface Sci* **2014**, *417*, 72-79.
144. COMSOL. COMSOL Multiphysics User's Guide. *Version: 5.1* **2015**.
145. Hu, H. H., et al. Direct Numerical Simulations of Fluid-Solid Systems Using the Arbitrary Lagrangian-Eulerian Technique. *J Comput Phys* **2001**, *169*, 427-462.
146. Qian, S.; Ai, Y. *Electrokinetic Particle Transport in Micro-/Nanofluidics: Direct Numerical Simulation Analysis*; CRC Press 2012; Vol. 153. p 382.
147. Keh, H.; Anderson, J. Boundary Effects on Electrophoretic Motion of Colloidal Spheres. *J Fluid Mech* **1985**, *153*, 417-439.
148. Li, D. *Encyclopedia of Microfluidics and Nanofluidics*; Springer Science & Business Media 2008; Vol. 1. p 2226.
149. Qiao, R. Effects of Molecular Level Surface Roughness on Electroosmotic Flow. *Microfluid Nanofluid* **2007**, *3*, 33-38.
150. Qiao, R.; He, P. Modulation of Electroosmotic Flow by Neutral Polymers. *Langmuir* **2007**, *23*, 5810-5816.
151. Happel, J.; Brenner, H. *Low Reynolds Number Hydrodynamics: With Special Applications to Particulate Media*; Springer Science & Business Media 2012; Vol. 1.
152. Buttinoni, I., et al. Dynamical Clustering and Phase Separation in Suspensions of Self-Propelled Colloidal Particles. *Phys Rev Lett* **2013**, *110*, 238301.
153. Theurkauff, I., et al. Dynamic Clustering in Active Colloidal Suspensions with Chemical Signaling. *Phys Rev Lett* **2012**, *108*, 268303.
154. Kline, T. R., et al. Catalytic Nanomotors: Remote - Controlled Autonomous Movement of Striped Metallic Nanorods. *Angew Chem* **2005**, *117*, 754-756.

155. Manjare, M., et al. Bubble Driven Quasioscillatory Translational Motion of Catalytic Micromotors. *Phys Rev Lett* **2012**, *109*, 128305-5.
156. Thorncroft, G. E., et al. An experimental investigation of bubble growth and detachment in vertical upflow and downflow boiling. *Int J Heat Mass Transfer* **1998**, *41*, 3857-3871.
157. Mehes, E.; Vicsek, T. Collective motion of cells: from experiments to models. *Integr Biol-Uk* **2014**, *6*, 831-854.
158. Gibbs, J. G.; Zhao, Y. P. Autonomously motile catalytic nanomotors by bubble propulsion. *Appl Phys Lett* **2009**, *94*.
159. Howse, J. R., et al. Self-motile colloidal particles: From directed propulsion to random walk. *Phys Rev Lett* **2007**, *99*.
160. Young, N., et al. The motion of bubbles in a vertical temperature gradient. *J Fluid Mech* **1959**, *6*, 350-356.
161. Hu, H.; Larson, R. G. Evaporation of a sessile droplet on a substrate. *The Journal of Physical Chemistry B* **2002**, *106*, 1334-1344.
162. Bergman, T. L.; Incropera, F. P. *Fundamentals of heat and mass transfer*; 7th ed.; John Wiley & Sons 2011. p 1048.
163. O'Shaughnessy, S. M.; Robinson, A. J. Numerical investigation of bubble induced Marangoni convection: some aspects of bubble geometry. *Microgravity Sci Tec* **2008**, *20*, 319-325.
164. Anderson, J. L. Droplet interactions in thermocapillary motion. *International journal of multiphase flow* **1985**, *11*, 813-824.
165. Hu, H.; Larson, R. G. Analysis of the effects of Marangoni stresses on the microflow in an evaporating sessile droplet. *Langmuir* **2005**, *21*, 3972-3980.
166. Bhardwaj, R., et al. Pattern formation during the evaporation of a colloidal nanoliter drop: a numerical and experimental study. *New J Phys* **2009**, *11*, 075020.
167. Yunker, P. J., et al. Suppression of the coffee-ring effect by shape-dependent capillary interactions. *Nature* **2011**, *476*, 308-311.
168. Solovev, A. a., et al. Collective behaviour of self-propelled catalytic micromotors. *Nanoscale* **2013**, *5*, 1284--93.
169. Velev, O. D., et al. Direct Measurement of Lateral Capillary Forces. *Langmuir* **1993**, *9*, 3702-3709.

170. Yang, F. C., et al. On the peculiar bubble formation, growth, and collapse behaviors in catalytic micro-motor systems. *Microfluid Nanofluid* **2017**, *21*.
171. Blander, M.; Katz, J. L. Bubble nucleation in liquids. *AIChE J* **1975**, *21*, 833-848.
172. Bankoff, S. Entrapment of gas in the spreading of a liquid over a rough surface. *AIChE J* **1958**, *4*, 24-26.
173. Matsumoto, M.; Tanaka, K. Nano bubble - Size dependence of surface tension and inside pressure. *Fluid Dyn Res* **2008**, *40*, 546-553.
174. Debenedetti, P. G. *Metastable liquids: concepts and principles*; Princeton University Press 1996.
175. Liu, X. Y. Heterogeneous nucleation or homogeneous nucleation? *J Chem Phys* **2000**, *112*, 9949-9955.
176. Fletcher, N. H. Size Effect in Heterogeneous Nucleation. *J Chem Phys* **1958**, *29*, 572-576.
177. Liu, D., et al. Prediction of the onset of nucleate boiling in microchannel flow. *Int J Heat Mass Transfer* **2005**, *48*, 5134-5149.
178. Hsu, Y. On the size range of active nucleation cavities on a heating surface. *J Heat Transfer* **1962**, *84*, 207-213.
179. Watanabe, H., et al. Ostwald ripening in multiple-bubble nuclei. *J. Chem. Phys.* **2014**, *141*, 234703.
180. Lee, H. S.; Merte, H. Spherical vapor bubble growth in uniformly superheated liquids. *Int J Heat Mass Transfer* **1996**, *39*, 2427-2447.
181. Robinson, A. J.; Judd, R. L. Bubble growth in a uniform and spatially distributed temperature field. *Int J Heat Mass Transfer* **2001**, *44*, 2699-2710.
182. Wu, M., et al. Scaling law in liquid drop coalescence driven by surface tension. *Phys Fluids* **2004**, *16*, L51-L54.
183. Rein, M. Phenomena of liquid drop impact on solid and liquid surfaces. *Fluid Dyn Res* **1993**, *12*, 61.
184. Blanchette, F.; Bigioni, T. P. Partial coalescence of drops at liquid interfaces. *Nat Phys* **2006**, *2*, 254-257.
185. He, P., et al. Fluid dynamics of the droplet impact processes in cell printing. *Microfluid Nanofluid* **2014**, 1-17.

186. Sussman, M.; Puckett, E. G. A coupled level set and volume-of-fluid method for computing 3D and axisymmetric incompressible two-phase flows. *J Comput Phys* **2000**, *162*, 301-337.
187. Fluent, A. 12.0 Theory Guide. *Ansys Inc* **2009**, 5.
188. Huang, W. J., et al. Manipulation of magnetic nanorod clusters in liquid by non-uniform alternating magnetic fields. *Soft Matter* **2017**, *13*, 3750-3759.
189. Shine, A. D.; Armstrong, R. C. The Rotation of a Suspended Axisymmetrical Ellipsoid in a Magnetic-Field. *Rheol Acta* **1987**, *26*, 152-161.
190. Liao, S. B., et al. *Visualizing Electromagnetism*: <http://web.mit.edu/viz/EM>, 2004.
191. Hirt, C. W., et al. An arbitrary Lagrangian-Eulerian computing method for all flow speeds. *J Comput Phys* **1974**, *14*, 227-253.